SURFACE FINISH MODELING IN MICROMILLING OF BIOCOMPATIBLE MATERIALS

A Thesis

by

DMYTRO VOLODYMYROVY BERESTOVSKYI

Submitted to the Office of Graduate Studies of
Texas A&M University
in partial fulfillment of the requirements for the degree of

MASTER OF SCIENCE

Chair of Committee,	Wayne Nguyen Hung
Committee Members,	Chii-Der Suh
	Jyhwen Wang
Head of Department,	Andreas Polycarpou

August 2013

Major Subject: Mechanical Engineering

ABSTRACT

Over the last few decades, miniaturization of the product became a necessity for many industries to achieve successful technological development, satisfy customer needs, and stay economically competitive in the market. Thus, many medical, aerospace, and electronic devices tend to decrease in size. Along with the strong demand for miniaturization, new cutting-edge micromanufacturing techniques are developing in order to produce microcomponents with a smooth surface finish and high dimensional accuracy. In the medical industry, some devices require manufacturing of fluidic microchannels on biocompatible materials for transportation of exact amount of medicine to a defined location. Often such microchannels must be manufactured to achieve a high aspect ratio, a submicron surface finish, and an anisotropic controlled profile. The fabrication of such channels on biocompatible materials still poses a challenge.

This study developed micromanufacturing technique to produce the microchannels and satisfy all the requirements listed above. Computer controlled micromilling on a high speed machine system in minimum quantity lubrication was used to remove most materials and define a channel pattern. Microchannels were machined with ball end mills of diameters from Ø152μm to Ø198μm on NiTi alloy, 304 and 316L stainless steels. Assessment of microchannel was performed with optical microscopy, scanning electron microscopy, and white light interferometry.

The theoretical surface roughness in ball end milling was derived using geometrical approach. The theoretical surface finish model was compared and validated with the experimental surface finish data. Meso- and macro-scale milling confirmed the validity of the model, but surface finish in micro-scale milling was measured to be a few orders of magnitude higher due to size effect and build-up edge. The build-up-edge was reduced when using AlTiN coated tools and milling in minimum quantity lubrication. The empirical surface roughness model obtained in this study shows the dependence of surface finish on chip load in micromilling. In order to further enhance the surface finish of milled microchannels additional finishing technique was identified. A separate study developed an effective electrochemical polishing technique to remove burrs and enhance surface finish of milled microchannels. When applying to 304, 316L stainless steel alloys and NiTi alloy, this hybrid technique can repeatedly produce microchannels with an average surface finish less than 100nm.

DEDICATION

I would like to dedicate this work to my wife Natalie Berestovsky, who encouraged, inspired and helped me during my years at Texas A&M, my sister Maryna Berestovska, and my parents Lyudmila Berestovska and Vlodimir Berestovskiy who provided their support even though they were far away during my years at graduate school.

ACKNOWLEDGEMENTS

I would like to thank my committee chair and graduated research advisor Dr. Hung, who provided outstanding environment for conducting a research in micromanufacturing and unforgettable experience in presenting our study at the ICOMM 2013 conference in Canada. I would like to thank my committee members, Dr. Suh and Dr. Wang, for their guidance and support throughout the course of this research.

I would like to thank Mr. Adam Farmer, Mr. Stephen Wells at Texas A&M University for they valuable guidance and help in conducting machining experiments.

I would like to thank Dr. Angie Price for allowing us to use equipment and machines in her laboratory to perform grinding and polishing experiments.

I would like to thank Professor Manny Soriaga, Mr. Dakota Brock, Mr. Xiao Han, and Mr. Brennon Sessions of Chemistry Department at Texas A&M University for their kind assistance in this research. Generous support from Agilent, Haas Automation, Unist, Performance Micro Tools, and Swiss-Tek Coatings is much appreciated.

Also, I would like to thank my parents and sister for their support during my years at graduate school. Finally, thanks to my wife for her encouragement, patience and love.

NOMENCLATURE

A_d	Axial Depth of Cut (mm)
D	Diameter of the Tool (mm)
D_e	Effective Diameter of the Tool (mm)
f_r	Feed Rate (mm/min)
f_{sp}	Spindle Speed Frequency (Hz)
f_t	Chip Load (mm/tooth)
f_{tooth}	Tooth Passing Frequency (Hz)
h	Height of Pick in Radial Direction (mm)
h_1	Height of Pick in Axial Direction (mm)
H_c	Height of Cusp (mm)
h_m	Critical Chip Thickness (mm)
h_{max}	Maximum Height of the Feed Mark (mm)
N	Spindle Speed (rpm)
n_t	Number of Teeth
R	Radius of the Ball End Mill (mm)
R_0	Tool Radius (mm)
R_1	Radius of the Radial Section of the Tool at Particular Depth (mm)
R_a	Average Surface Roughness (µm)
R_t	Maximum Peak-to-valley Surface Roughness (µm)
V	Cutting Speed (m/min)

V_e	Effective Cutting Speed (m/min)
x_G	Coordinate Of Center of Gravity (mm)
y_G	Coordinate Of Center of Gravity (mm)

TABLE OF CONTENTS

Page

LIST OF FIGURES

Page

Page

Page

Page

LIST OF TABLES

Page

1. INTRODUCTION

Product miniaturization is an essential driving factor for many industries due to customer demands and high and efficient technological development. Smaller sizes of the components lead to many advantages such as smaller occupied space, lower energy consumption, lower material consumption, and better heat transfer due to the lower surface to volume ratio [1]. Therefore, many medical, aerospace, optical, communicative, automotive, and information devices tend to decrease in size. Along with the strong demand for miniaturization, the high dimensional accuracy and high surface quality of the miniature components is very often required. The production of such components requires cutting-edge micro-manufacturing technologies and techniques [2], [3].

The manufacturing of many medical devices requires utmost precision and state-of-the-art quality control. In the medical industry fluidic microdevices require manufacturing of small channels to transport precise doses of medicine or an exact amount of biofluid to prescribed locations. Fabrication of such microchannels on biocompatible materials is still a challenge when high aspect ratio, anisotropic profile, submicron surface finish, and controlled contour of the channel surface are required. Currently, manufacturing techniques such as laser machining and chemical etching are used to produce similar types of microchannels. However, a laser cannot produce microchannels with controlled anisotropic profile and an isotropic chemical etching process cannot produce high aspect ratio channels. In addition, chemical etching requires intricate expensive mask and utilization of unique chemical solution for each material. This makes the etching process complex and time consuming.

Conventional micromilling has the potential to be the most cost effective and efficient material removal processes. The micromilling with ball end mills in combination with electrochemical polishing can be used to economically manufacture fluidic microchannels with minimum surface damage. Depending on a system, micromilling could provide reasonable surface roughness, dimensional and geometric accuracy, and higher productivity compared to other micromachining techniques. Also, different engineering materials such as metal alloys, polymers, ceramics, and composites can be machined using similar tooling and procedure [4].

Although micromilling has been investigated, there is limited research work using microsize ball end mills. This research is part of a larger project to manufacture complex, deep, and smooth microchannels for medical applications.

The main objectives of this research are:

i. Develop and optimize micromilling techniques to produce complex, deep, and smooth microchannels on biocompatible materials.
ii. Analyze and study surface finish after ball end milling on biocompatible materials.
iii. Identify technique to enhance surface finish of milled microchannels.
iv. Develop a model to predict surface roughness after ball end milling, validate it with experimental data, compare with other models from literature.

The scope of this research includes:

i. Ball end milling with tools of diameters from Ø152µm to Ø9.525mm

ii. Micromilling of channels on biocompatible materials such as NiTi alloy, CP titanium, 304 and 316L stainless steels.

iii. Modeling of the surface roughness of micromilled surfaces.

2. LITERATURE REVIEW

Various nontraditional fabricating processes and techniques have been and are still researched to manufacture micro-components, such as LIGA (a photo-lithography technique with utilizing of a synchrotron), laser, ultrasonic, ion beam, electron beam, and micro-electro discharge machining (EDM) [1], [5]. Laser micro machining is very complex and costly process. The disadvantage of the utilization of the laser is that the mechanical properties of the machined material can be changed near the heat affected zone. Electro discharge machining is another method that can be used for micro machining operations. The main drawback of this method is that it causes subsurface damage and results in rough surface finish, due to formation of recast layers [6]. Lithography-based micro electro mechanical systems (MEMS) process can be utilized to produce lower than micrometer size components. The drawback of this technique is that it is very slow and expensive, has low productivity, incapable to create complex geometries, and can be applied only to a few silicon based materials [3].

Other traditional manufacturing processes that can be applied to produce miniature features are micromilling and microdrilling. The micro components with sizes 10-10,000 µm can be created using this method. The micromilling provides lower surface roughness and higher dimensional and geometric accuracy comparing to other micromachining techniques [7], [8]. Micromilling does not cause surface damage, as oppose to EDM and lithographic methods [9]. Also, manufacturing of the 3-dimensional complex components can be done using micro mechanical cutting process such micro ball end milling, which is significant for the manufacturing of the microinjection molds and dies. Currently, limited research work has been done in the field of mechanical machining of micro- and meso-scale components; therefore, this field is of current interest for many researchers [1].

The trends to manufacture smaller and more accurate components has been the same, since the early days of manufacturing [10]. In particular, the machining capability and accuracy improvement over time for last six decades can be observed in the Figure 1 [11]. It can be seen from this figure that the accuracy of the different machining techniques has been enhancing significantly with time.

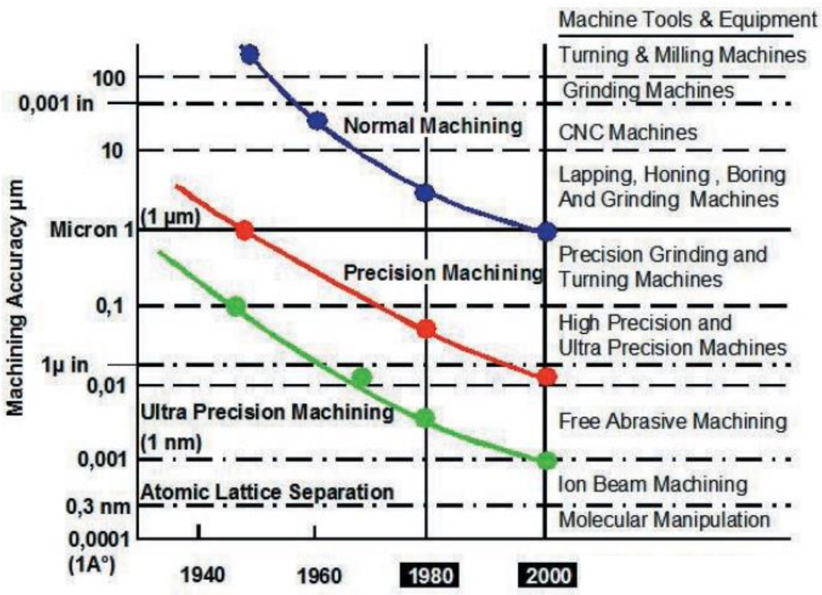

Figure 1. Machining Capability over Time [11].

2.1 Microfluidic Channels

Recently, traditional drug delivery systems (DDS) have been intensively studied. Drug delivery systems are used to provide more efficient treatment for the patients by delivering precise doses of drug to the human body. Traditional drug delivery methods such as oral medication and liquid injection do not provide long drug duration in the human body and require repeated drug delivery. In addition, it is still a challenge to control precisely drug release rate while delivering drug with traditional methods.

Recent development in micromanufacturing led to the investigation of new nontraditional drug delivery systems with microreservoirs and microchannels (Figure 2). In these microdevises, drug is placed in the microreservoirs until it is delivered to the body. The size of the microreservoirs can vary from 100μm to 1mm. The microchannels are used to release precise doses of drug dissolved in water in prescribed locations when the microdevice is engaged in aqueous environment. In this nontraditional drug delivery systems drug release rate can be accurately controlled by selecting number, proper geometry, and dimensions (length, width, and depth) of the fluidic microchannels [12]. In order to provide uniform fluidic flow of the biofluid, the channels should have high geometric accuracy and smooth surface finish. In addition, for implantable medical devices microchannels should be manufactured on biocompatible materials such 316L stainless steel, CP titanium, Nitinol, or PEEK polymers.

Manufacturing of fluidic microchannels can be done using different manufacturing techniques such laser machining, lithography, chemical etching, and micromilling. Laser machining cannot be used when controlled anisotropic profile of the channel is required.

In addition, channels machined with laser usually have rough surface finish (Figure 3) [13].

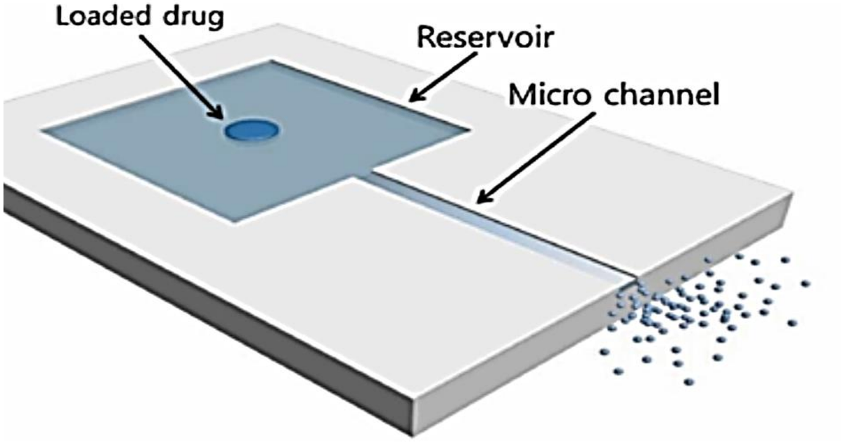

Figure 2. Microfluidic Drug Delivery Device [12].

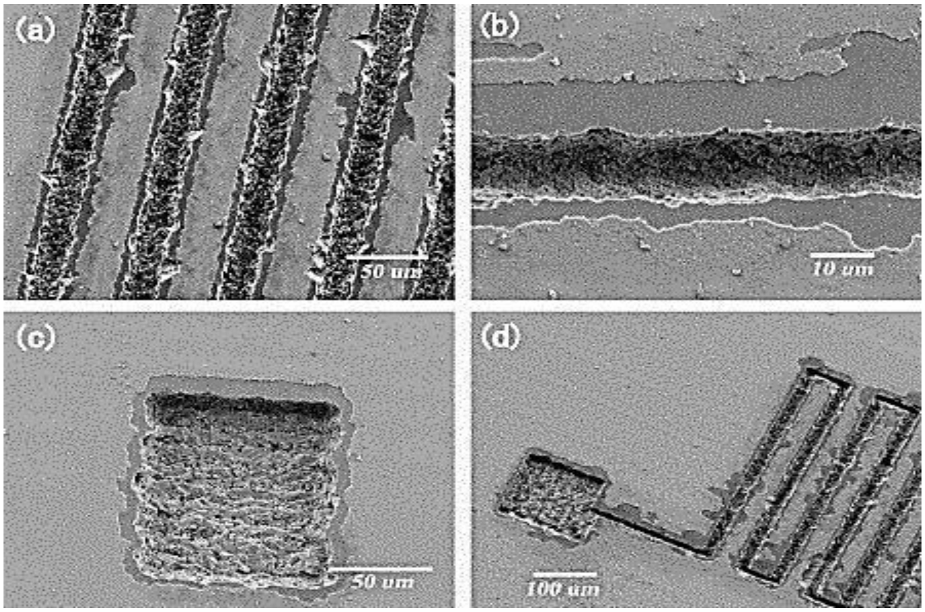

Figure 3. SEM Images of Microchannel Patterns Machined on Anodic Alumina Film (Al_2O_3) with pulsed Nd:YAG Laser. Channel Depth 12µm –15µm, Power Density 125 mW/cm^2, Scan Depth 30 µm/s: (a) Microchannels at Regular Intervals; (b) Magnified View of a Microchannel; (c) Microchamber; (d) Microchamber with a Microchannel [13].

Chemical etching process cannot produce high aspect ratio channels and requires intricate expensive mask and utilization of unique chemical solution for each material. The conventional micromilling in combination with electrochemical polishing can be used to economically manufacture fluidic microchannels with minimum surface damage. Depending on a system, micromilling could provide reasonable surface roughness, dimensional and geometric accuracy, and higher productivity comparing to other micromachining techniques.

2.2 Micro vs Macro Machining

The basic concepts, characteristics, and knowledge about micro mechanical machining were adopted and transformed from the macro machining domain. However, micro machining has much more challenges and constrains comparing to conventional macro machining for which many studies have been done, documented, and standardized [1]. For micromachining a lot of research is still to be done, focusing on the machining of the dimensions in the range 1 µm – 999 µm [14].

The challenges associated with micromachining rise from size effect of miniaturized cutting tools, work pieces, and overall process. When dimensions of a microtool and depth of cut are on the same order of magnitude as the grain size of the machined material, anisotropy of grain’s mechanical properties and its crystallographic orientation influence the micro cutting process, which is not the case for the conventional macro cutting [10]. For conventional macro machining the cutting mechanism takes place when material of the workpiece is sheared at the tool tip and removed as a chip. For micromachining the shear process at the tool tip is more complicated and depends on the degree of size effect, which is the effect observed when the depth of cut is on the same order as cutting edge radius.

For micro cutting process chip-shear mechanism occurs at the tool edge, as opposed to the conventional macro cutting where chip-shear mechanism takes place at the rake surface of the tool [15]. In this case of micromachining the rake angle has a high negative value, which leads to the serious increase in the shear force on the tool, high surface roughness, elastic recovery of the machined surface, and the plowing during micromachining [1]. The difference in the macro and micro cutting mechanisms with respect to the rake angle can be seen in the Figure 4.

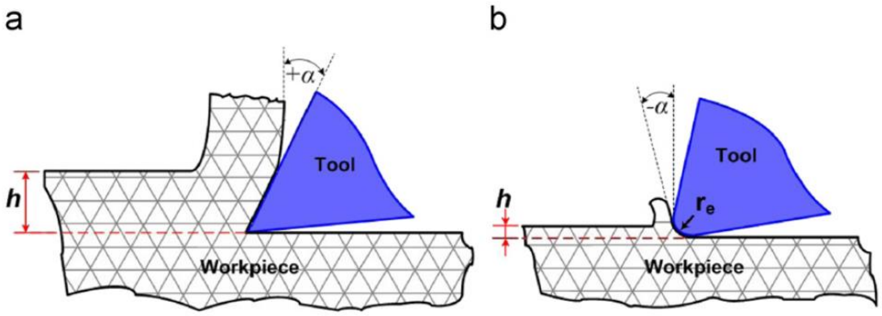

Figure 4. Difference in the Geometry for Macro (a) and Micro Machining (b) [14].

According to Liu *et al* [7], [8] and Kim *et al* [16] the larger amount of elastic-plastic deformation occurs on the work material during micromachining due to the large rake angle, than during macro mechanical machining. The plastic deformation results in more difficult separation of the material because material is work-hardened by increased dislocation density. Due to the large rake angle, the rise in the force results in a faster wear, an increase in the deflection and vibrations, and a build-up edge formation on the micro tools [1].

Very often, the failure of the micro tools occurs when chip thickness is smaller than cutting edge radius, which is about 1-3μm for micro tools [17]. In some sources the critical chip thickness was studied and its critical values were suggested. When chip thickness is lower than critical chip thickness during micro machining, the cutting process does not occur, since material is not removed and is only deformed elastically. In other words, depth of cut and chip load during micro machining should be larger than the critical chip thickness to provide cutting. The dependence of the chip formation on the critical chip thickness is shown in the Figure 5. It is seen from the Figure 5 (a) that when uncut chip thickness (*h*) is lower than critical chip thickness (*hm*), material of the workpiece is not removed and is only deformed elastically [1]. Thus, plowing of the cutting edge on the surface of the workpiece occurs, which leads to bad surface roughness, faster wear of the tool, and can cause surface defects [18].

In the case where critical chip thickness (*hm*) is slightly lower than uncut chip thickness (*h*) cutting occurs by shear process with a little portion of the elastic deformation (Figure 5(b)). This cutting mechanism results in real depth of cut being lower than required depth of cut, since some portion of the material recovers elastically during micro machining. Finally, if critical chip thickness (*hm*) is smaller than uncut chip thickness (*h*), cutting process occurs with minimum and insignificant elastic deformation (Figure 5(c)) [7], [8], [16].

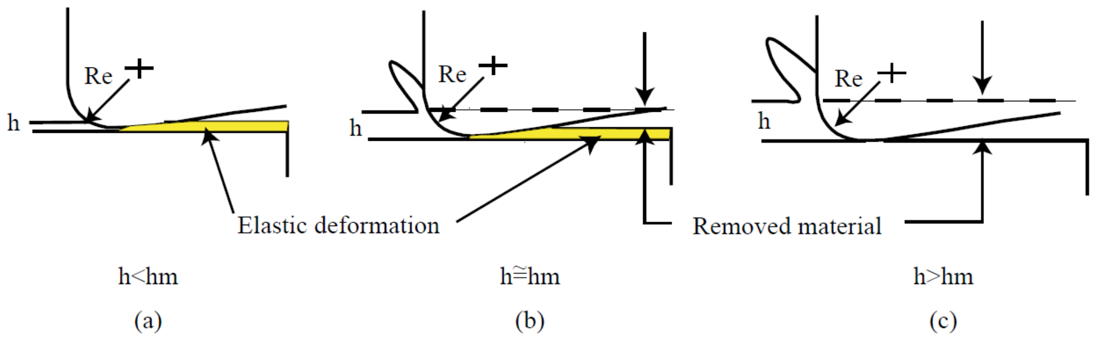

Figure 5. Dependence of the Cutting Process on the Critical Chip Thickness (R_e – radius of tool edge, h – uncut chip thickness, hm - critical or minimum chip thickness) [1].

Several researchers have studied the critical chip thickness. The critical chip thickness can be determined using either finite element analysis or experimental results [19]. Vogler *et al* [19] utilized finite element analysis to find critical chip thickness for micromachining of steel. According to their study, the critical chip thickness can be estimated as 20-30% of the cutting edge radius during micromechanical machining of the pearlite and ferrite steel. However, Shimada *et al* [20] determined that critical chip thickness is about 5 % of the tool edge radius during micro machining of the aluminum and cooper. It is clear that there is no standard definition for minimum or critical chip thickness and a lot of research is still to be conducted in this area. Liu *et al* [21] used experimental approach in their study to estimate the critical chip thickness for micromachining. They concluded that when thrust force increases abruptly, it indicates the crossing of the critical value of the chip thickness and shifting form plowing predominant forces to shearing predominant forces, which is shown in the Figure 6.

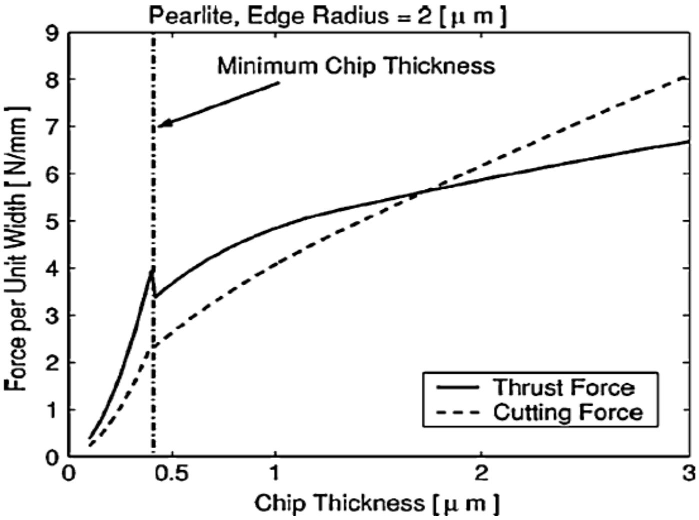

Figure 6. Chip Thickness and Force Correlation in Micromachining of Perlite [1].

One more important difference between macro and micromachining is that microstructure of the work piece plays more significant role during microcutting process than it does during macrocutting. Very often during micromachining, the work piece can’t be considered as isotropic material [10], [22]. The microstructure of the work piece has a noticeable influence on the formation of the surface, surface finish, and cutting forces during micromilling of the multi-phase materials [19], [23]. The cutting mechanism of the polycrystalline, single crystal, and amorphous materials is very distinctive. During microcutting of the polycrystalline materials the cutting force changes significantly when tool cutting edge goes through grain boundary (Figure 7). On the other hand, while micromachining the single crystal or amorphous material the cutting forces do not change significantly. The influence of the microstructure and anisotropy of the grains in the polycrystalline materials can be neglected when the grain size is ten times lower than depth of cut, which is always the case for macro mechanical machining [10], [24].

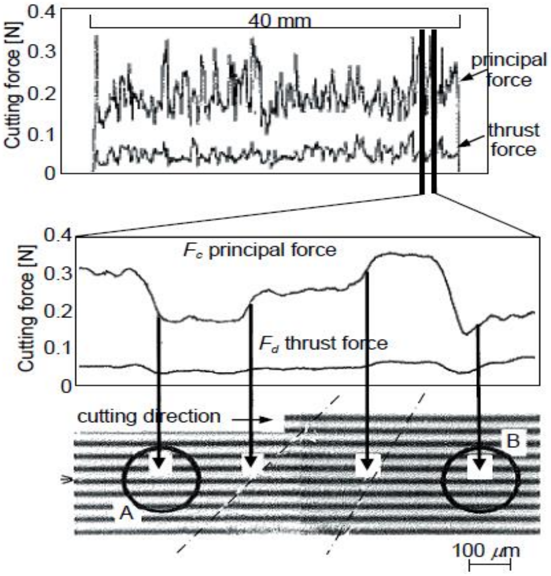

Figure 7. Fluctuation of the Principal Cutting Force Depending on the Grain Boundary. Material of the work piece - Al alloy [10].

Another significant difference between micromachining and macromachining is a tool runout. One of the main reasons for the tool runout lies in the misalignment between axis of the tool and the axis of the spindle of the milling machine. For the conventional macromachining tool runout is minor issue, since its value is much smaller comparing to the tool size and is very often neglected. On the other hand, for the micromachining where size of the tool is lower than 1 mm and spindle speed can reach 100,000 rpm the tool runout can be a significant problem. Even small deflection of the tool can cause the significant increase in the vibrations, accelerated wear, higher surface roughness, and even sudden failure of the microtool during cutting. Therefore, additional attention should be given to the control of the tool runout prior to the beginning of the micromachining. One of the sources for the runout is tool holder. The utilization of the collet-type holders to secure micro tools provides lower value of the runout. The collet is a recommended type of tool holder comparing to the set-screw type holder during micromilling [1].

Other common challenges that can be encountered during micromachining are difficulties with securing, handling, and setting up microtools and the work pieces on the milling machine, difficulties in monitoring and controlling of the process in real time, and the lack of the metrology standards [3]. Conventional methods for holding micro parts during micro machining operations often can’t be utilized. The forces needed to secure the work piece are also very low, since the cutting forces during micromachining operations are much lower than during conventional macro machining. Thus, the micro parts can be secured using the glue, double-sticky tape or heat activated wax glue [25].

2.3 Micromilling

Micro end milling is one the most productive and cost efficient micromachining processes, that can be used to produce 3-dimensional features with high accuracy and precision, smooth surface finish, and high material removal rate. The sizes of the tungsten-carbide micro end mills that are currently commercially available are as small as 25 µm. The micro end mills are currently used in the industry to produce micro parts for micro molds and dies made of tool steel. Also they are utilized to machine micro parts for the medical implants [4].

The schematic representation of the milling process is shown in the Figure 8. The cutting conditions that are controlled during milling operations are depth of cut, chip load (feed per flute), and cutting speed. As opposed to macromilling where the optimal cutting conditions have long been determined, documented, and can be selected from the reference books depending on different factors such as the material of the work piece, material of the cutting tool, desired surface finish, or tool life, there are no a standards for cutting conditions for micromilling operations.

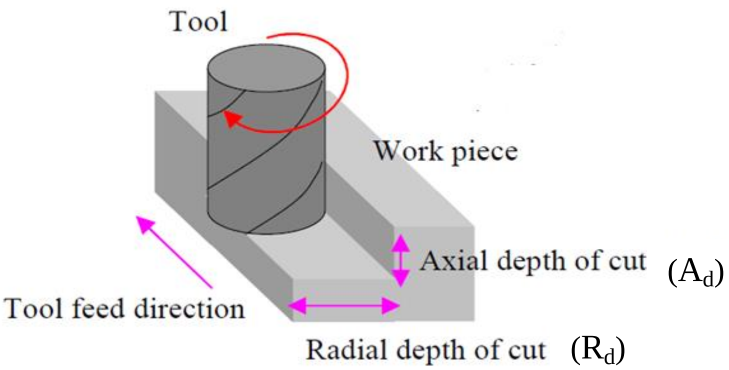

Figure 8. Schematic Representation of the Milling Process [26].

There are two different kinds of depth of cut for micro end milling operations: radial depth of cut (R_d) and axial depth of cut (A_d), which are shown in the Figure 8. The depth of cut that is used during micromilling varies from a few microns to hundreds micrometers depending on the diameter of the tool and material of the work piece. For example, Schueler *et al* [18] performed micro end milling of titanium alloy Ti6A4V with tungsten carbide tool Ø48µm using axial depth of cut of 40µm and radial depth of cut 2µm. Ozel *et al* [27] used axial depths of cut 40µm, 70µm, and 100µm for slot micromilling of the same titanium alloy Ti6A4V with tungsten carbide micro end mill Ø381µm.

The feed in milling operations is usually defined as a feed per tooth or flute, and it is called chip load (f_t). The units for the chip load are µm/flute or mm/tooth. Chip load is a parameter that shows the thickness of the chip removed by one tooth of the tool per one revolution. The feed rate is another cutting parameter that can be calculated for end milling using following equation [28]:

$$f_r = N n_t f_t \tag{2.1}$$

where

f_r : feed rate (mm/min)

N : spindle speed (rpm)

n_t : number of teeth

f_t : chip load (mm/flute)

Cutting speed (V) is a linear speed at which the cutting edge is moving while spinning on the outside diameter of the mill. The units of the cutting speed are m/min. The relationship between cutting speed, diameter of the milling cutter and spindle speed is represented by following equation [28]:

$$N = V/\pi D \tag{2.2}$$

where

N : spindle speed (rpm)

V : cutting speed (mm/min)

D : diameter of milling cutter (mm)

The tool is exposed to two cutting forces during slot end milling that are shown in the Figure 9. The force F_x is directed in the opposite direction to the feed. The second force F_y is directed in the normal direction to the cutting edge. Both forces increase when the feed rate increases during end milling. The cutting forces can be determined by the direct measurements using different types of dynamometers or can be predicted using finite element models [4].

Finite element models (FEM) are often utilized to predict cutting forces, chip formation, stress state and the temperature at the cutting zone. The prediction of the cutting forces for micro milling is an important, since it provides ability to estimate the deflection of the microtool. The tool deflection is one of the main reasons for low accuracy of the machined part, faster tool wear, and sudden failure of the tools [29].

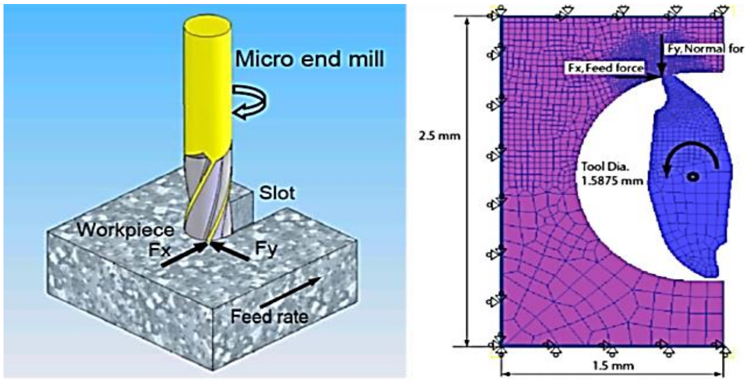

Figure 9. Schematic Representation of the Direction of the Cutting Forces during End Milling of the Slot [29].

Ball end mills, or ball nose milling cutters, are outstanding cutting tools for machining of the complex 3-dimensional surfaces using the machine tools with computer numerical control (CNC). The ball end milling is frequently utilized to produce parts with complex configurations and shapes such as medical implants, molds and dies [30]. The configuration and shape of the of the ball nose end mill results in effective cutting process and provides ability to cut material from any angle and direction. The cutting edge of the tool starts at its tip and evolve into the helical [31]. Figure 10 shows a complex 3D statue that was machined on the 5 axis CNC machine tool with micro ball end mill [10].

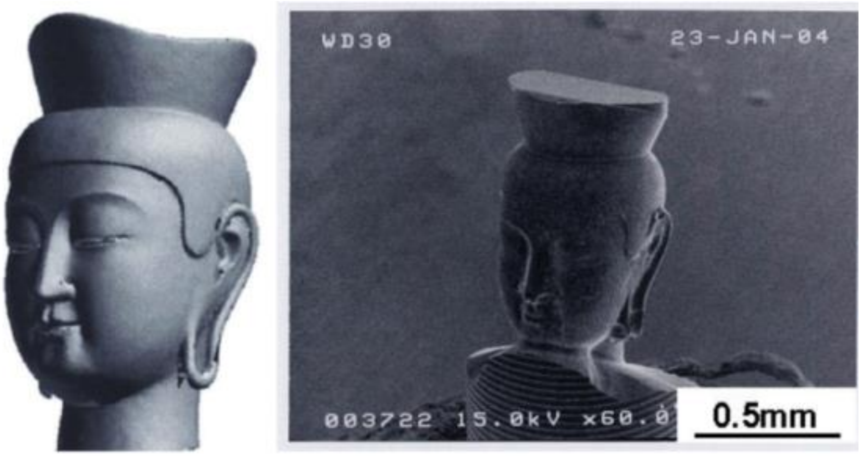

Figure 10. Micro Statue Machined with Ball End Micro Mill on 5 Axis CNC Machine Tool [10].

Cutting speed is not constant along the cutting edge of the tool during ball end milling process. The magnitude of the cutting speed is close to zero at the tool tip, and it rises in the direction towards the maximum diameter of the tool. When axial depth of cut is lower than radius of the ball end mill, the effective diameter (D_e) of the tool must be considered to estimate spindle speed. The effective diameter in ball end milling is shown in the Figure 11. The effective diameter of the tool depends on two parameters – tool radius and axial depth of cut, and can be determined using following equation [31]:

$$D_e = 2\sqrt{R^2 - (R - A_d)^2} \tag{2.3}$$

where

D_e : effective diameter of the tool (mm)

R : radius of the ball nose end mill (mm)

A_d : axial depth of cut (mm)

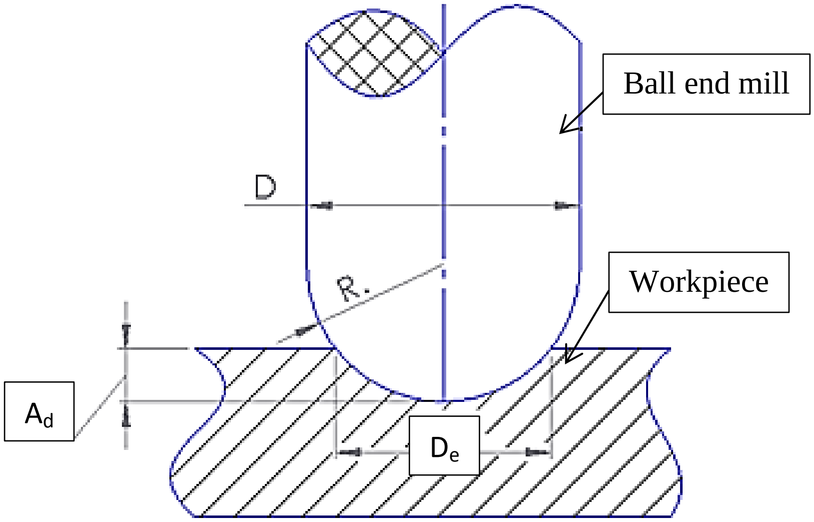

Figure 11. Effective Diameter D_e for Ball End Milling.

When axial depth of cut is smaller than the radius of the ball end mill, the effective cutting speed (maximum cutting speed) should be calculated taking into account effective diameter of the tool [31]:

$$V_e = \pi D_e N \tag{2.4}$$

where

V_e : effective cutting speed (mm/min)

D_e : effective diameter of the tool (mm)

N : spindle speed (rpm)

When ball nose end mill is used to machine flat surface with tool trajectory in zigzag pattern, unmachined stripes will be produced on the flat machined surface. These strips or cusps are created between each two neighboring passes of the tool and result in the high surface roughness in the direction perpendicular to the feed (Figure 12). The height of the cusp (H_c) can be estimated according to the equation [31]:

$$H_c = R - \sqrt{R^2 - (R_d/2)^2} \tag{2.5}$$

where

H_c : height of cusp (mm)

R : radius of the ball nose end mill (mm)

R_d : radial depth of cut (mm)

In contrast to the ball end milling, when flat surface is machined with flat end mill the cusps are not created on the machined surface. Therefore, the ball end milling is not recommended for zigzag machining of the flat surfaces when the final product requires smooth surface finish.

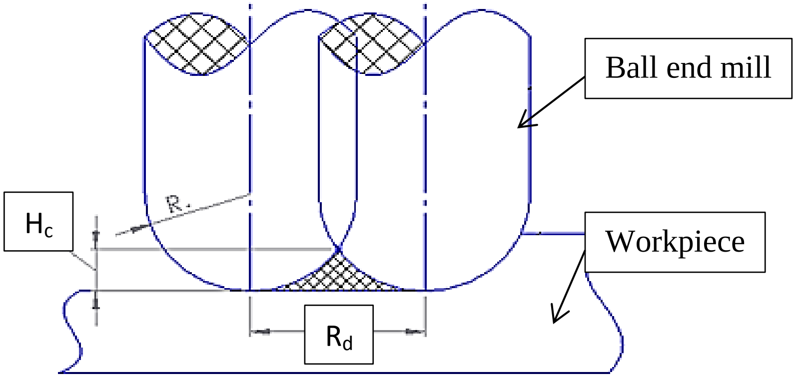

Figure 12. Cusp Height H_c for Zigzag Ball End Milling of the Flat Surface.

2.4 Surface Roughness after Micromilling

Smooth surface is often required on components for many medical and aerospace applications. Surface roughness for macromilling operations was understood and could be predicted using recommended cutting conditions from many reference books. On the other hand, very limited work has been done to understand controlling factors of surface roughness in micromilling. Usually conventional macro milling processes do not provide smooth surface finish, thus, finishing processes such as grinding and polishing are used afterwards. The components that are produced by micromilling processes are very tiny in size, therefore, finishing processes are difficult to apply. Rough and finishing milling passes and electrochemical polishing can be utilized to provide a smooth surface finish. In conventional end milling, surface roughness usually depends on geometry of the tool, condition of the tool, and cutting conditions. Some cutting conditions, such as feed or chip load, have the most significant effect on the surface finish, others, such as depth of cut and cutting speed, have less impact. However, the dependence of surface finish on cutting conditions in micro milling has not yet been clarified and a lot of research is currently conducted in this area [26].

Shizuka *et al* [26] conducted a study to determine the effect of feed and depth of cut on surface roughness during down-cut micro end milling. In their experiment they performed wet micro milling on cold worked mold steel (SLD11) with TiAlN coated tungsten carbide end mill with diameter Ø900μm. Different chip loads, axial and radial depths of cut were used in their experiment. The results of the experiments are shown in the Figure 13. It is seen from the Figure 13(a) that the surface roughness in micro milling does not depend significantly on feed as it does in conventional macro milling. Also, the axial depth of cut does not have an influence on the surface finish (Figure 13(b)). In contrast to feed and axial depth of cut, radial depth of cut has the most significant impact on the surface roughness, and it increases with radial depth of cut (Figure 13(c)). It can be seen from the Figure 13(c) that surface roughness stars to deteriorate when value of radial depth of cut rises above the value of tool radius (450 μm). It happens because cutting forces increase considerably, which leads to the tool deflection and chatter vibrations. Therefore, according to this study, the radial depth of cut should be considered as criterion which causes deterioration of the surface roughness during down micro end milling of flat surfaces [26].

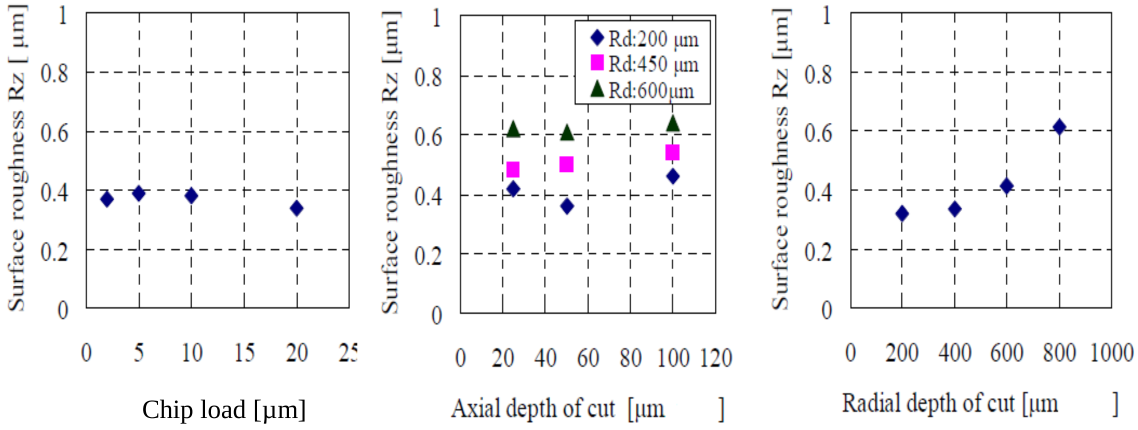

(a) (b) (c)

Figure 13. Relationship between Chip Load, Axial Depth of Cut, Radial Depth of Cut, and Surface Roughness [26].

Tsuda *et al* [2] investigated the influence of the flood cooling fluid and cutting speed on the surface finish during micro milling of Ti6Al4V titanium alloy with tungsten carbide flat end mill. During their experiments the surface of the workpiece was covered in water-insoluble cutting fluid. The results that they obtained are shown in Figure 14. R_z type of surface roughness rises when machined distance increases during dry cutting. In contrast, when coolant is applied, the surface finish does not vary significantly with machined distance. Also, the surface finish of the workpiece machined with higher cutting speed (198 m/min) is better R_z=0.37µm than for surface machined with lower cutting speed (51 m/min) R_z= 0.6µm. It can be concluded from the results shown in the Figure 14 that the utilization of the higher cutting speed while micromilling of Ti6Al4V alloy results in the effective machining process and better surface finish. Also, cooling fluid should be always applied when smooth surface roughness is needed, since it reduces the tool wear and results in better surface finish of machined component [2].

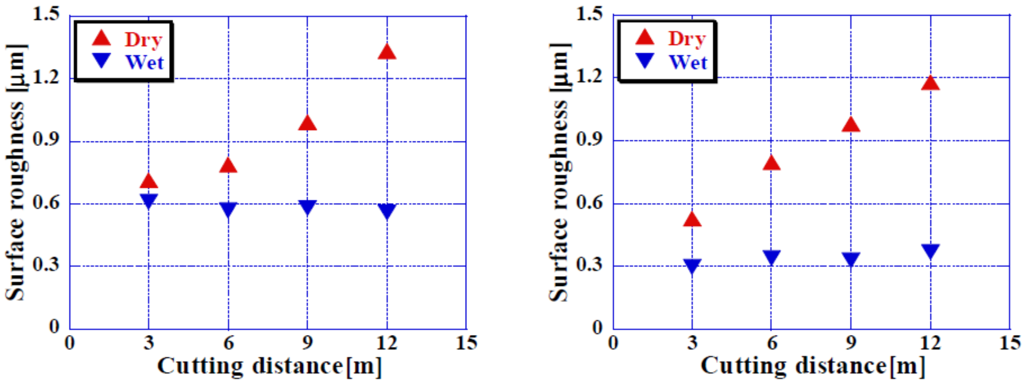

(a) Cutting speed of 51 m/min

(b) Cutting speed of 198 m/min

Figure 14. Effect of Cutting Distance on R_z Surface Roughness for Dry and Wet Micromilling of Ti6Al4V alloy [2].

Ozel *et al* [27] studied the effect of the cutting speed, feed and depth of cut on the surface finish during dry slot micromilling of Ti6Al4V titanium alloy with uncoated tungsten carbide and CBN coated flat end micro mills (Ø381µm, Ø508µm, and Ø635µm). The results of their study are shown in the Figure 15 [27]. It is seen form the Figure 15 (a) that when the cutting speed increases the surface roughness decreases for the microtools with diameter Ø508µm and Ø635µm. However, for the tool with diameter Ø381µm the correlation between cutting speed and surface roughness is reversed. Figure 15 (b) shows that the effect of the feed on surface finish is less significant than effect of the cutting speed. Finally, the minimum depth of cut results in the best surface finish, as shown in Figure 15(c).

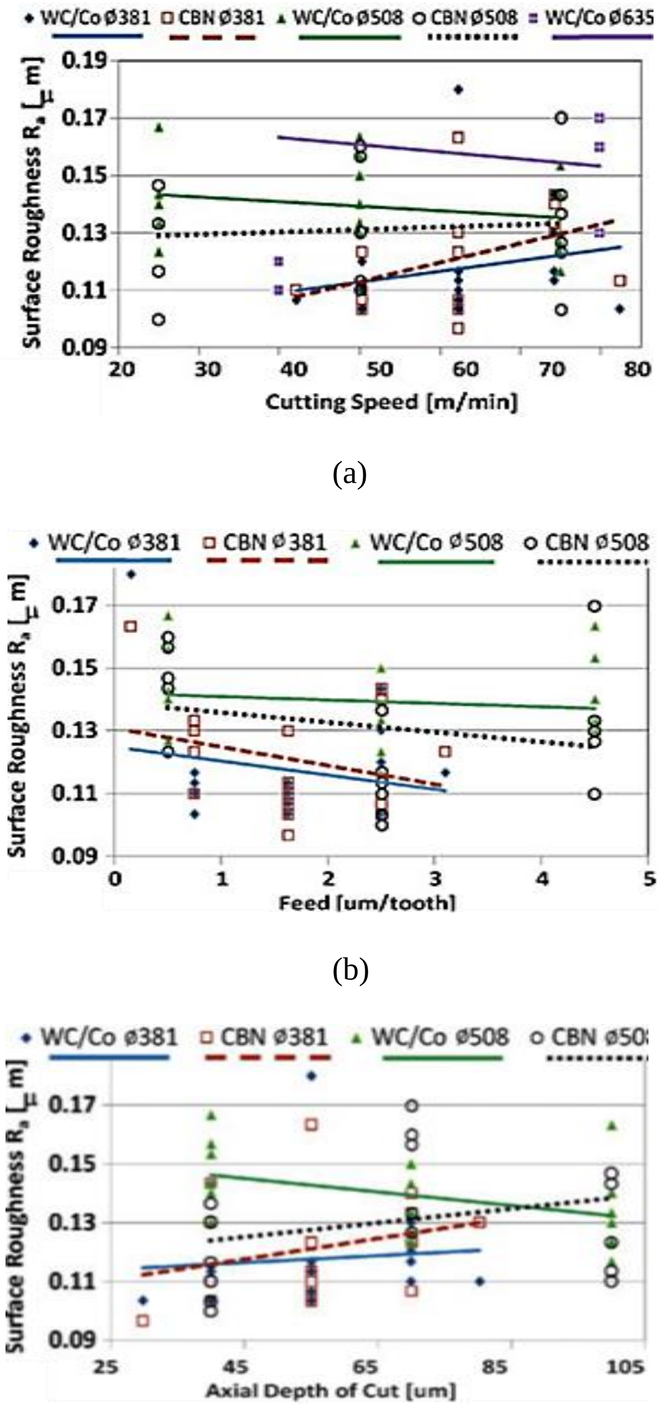

(a)

(b)

(c)

Figure 15. Effect of Cutting Speed, Feed, and Axial Depth Cut on the Surface Roughness for Dry Micromilling of Ti6Al4V Titanium Alloy [27].

Li *et al* [32] studied the influence of the tool wear on the surface finish during micromilling. In their experiment they used Ø100µm micro end mill for dry machining of the slots in the copper. The tool wear usually depends on the cutting speed and material removal volume. Consequently, the surface roughness is affected by these parameters as well. According to their study, surface roughness measured at the bottom of the machined slots was significantly affected by the tool wear. The increase of surface roughness with increase of machining length is shown in the Figure 16. According to the Figure 16 the surface roughness rises from R_a=144nm after machining of 3 slots (Figure 16 (a)) to R_a=535nm after machining of 90 slots (Figure 16 (c)) as tool wear progresses.

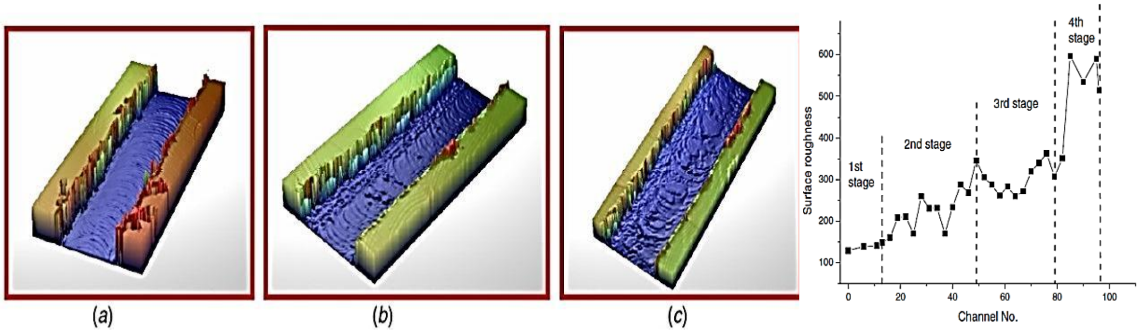

Figure 16. Surface Topography of the Machined Slots: (a) after 3rd Slot R_a=144nm; (b) after 45th Slot, R_a=196nm; (c) after 90th Slot, R_a=535nm [32].

According to the plot in the Figure 16 the change of surface roughness with material removal volume can be observed in four stages. At the first stage there is no significant tool wear, thus, surface roughness does not vary a lot. At the second stage surface roughness increases promptly from R_a=148.5nm to R_a=345.84nm, which corresponds to the fast wear of the microtool. There is no apparent increase in surface roughness at third stage, which means that the wear of the tool does not change significantly – stable stage. Finally, at the fourth stage surface roughness raises greatly from R_a=345nm to R_a=597.3nm, which conforms to the significant increase in the tool wear and approach of the breakage [32].

Also, it is worth mentioning, that surface roughness measured along the center line of the channel bottom is maximum when tool is new or in a good condition, since there is a largest value of the feed rate along the center line (Figure 17(a)). However, as the wear of the microtool progresses, it is not the case anymore, and maximum surface finish can be observed in any location of the bottom surface, since it starts being affected by the wear geometry of the micromill (Figure 17(b) and (c)) [32].

Figure 18 shows the effect of the cutting speed, material removal volume, and depth of cut on the surface roughness in dry micromilling of OFHC copper with 0.1mm diameter tungsten carbide microtool. It is clear from the Figure 18 that cutting speed and material removal volume have the greatest effect on the surface roughness. The surface roughness does not vary significantly with increase of depth of cut from 6 µm to 20 µm. The work of Li *et al* [32] concludes that tool wear during micromilling has more significant effect on the surface finish compared to the macromilling. Thus, cutting parameters such as cutting speed and material removal volume should be considered for evaluation of the final surface finish, because they are the main parameters that determine the progress of the tool wear [32].

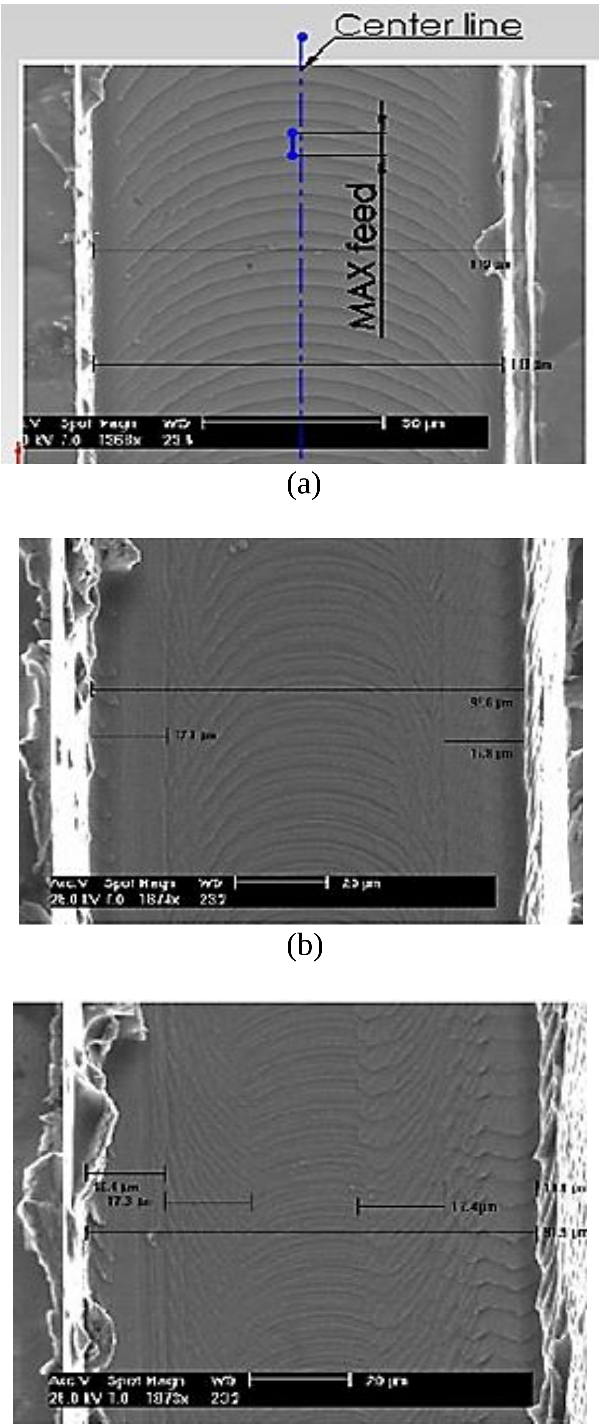

(a)

(b)

(c)

Figure 17. SEM Pictures of the Bottom Surface of the Slots: (a) after 3rd slot; (b) after 45th slot; (c) after 90th slot [32].

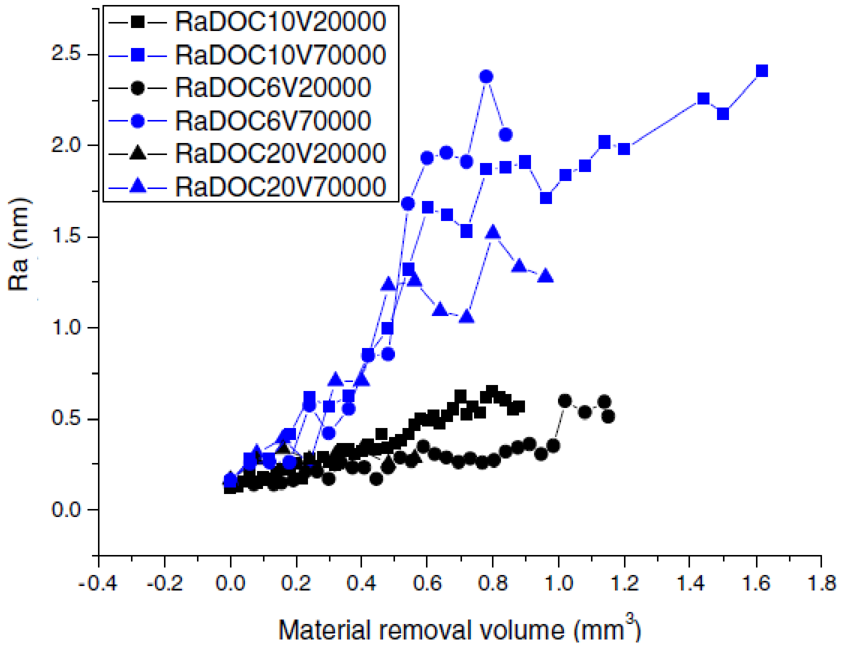

Figure 18. Dependence of R_a Surface Roughness on the Spindle Speed (V, rpm), Depth of Cut (DOC, µm), and Material Removal Volume (MR, mm^3) [32].

Schueler *et al* [18] also investigated the surface characteristics during dry slot micro end milling of Ti6Al4V and Ti6Al4Nb titanium alloys with tungsten carbide micro end mills Ø48µm. They conducted micromachining experiments with three different chip loads 0.84µm/tooth, 0.168µm/tooth, and 0.252µm/tooth, and concluded that feed rate does not have a significant effect on the surface finish. For these three different cutting conditions the average value of the surface roughness of the bottom of the slot was approximately R_a=100nm. They also concluded that the surface finish of the side walls in the machined slots obtained during down milling is much better than surface finish generated during up milling process. Therefore, when low surface roughness of the side walls of the slot is desired, finishing down milling passes should be applied.

Hamaguchi *et al* [33] investigated the effect of tool tilting angle on the surface roughness in dry micro ball end milling. Four experiments were conducted with four different tilting angles of spindle 0°, 15°, 30°, and 45°. Tungsten carbide micro ball end mill of diameter Ø200µm was used to machine hardened stainless steel with constant spindle speed and chip load, 120,000rpm and 10µm/tooth respectively. The dependence of surface roughness on the cutting distance and tilting angle of the spindle is shown in the Figure 19.

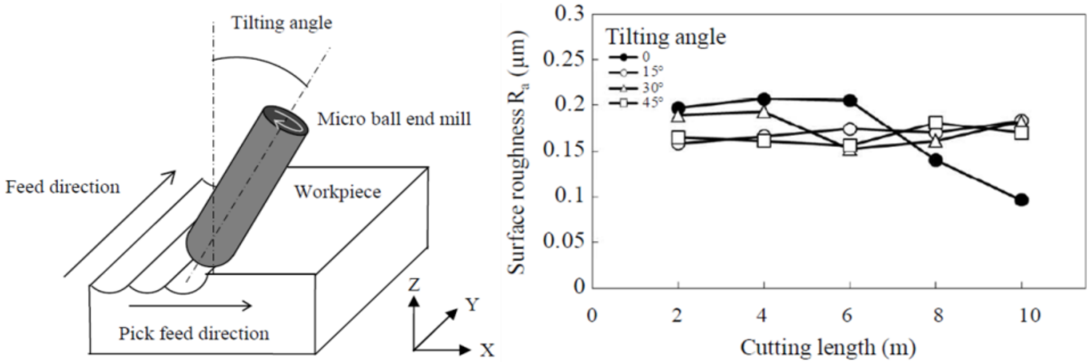

Figure 19. Dependence of Surface Roughness on Tool Tilting Angle and Cutting Length [33].

According to the Figure 19 the values of surface roughness are very similar for machining with tilting angles 15°, 30°, and 45° and they do not change significantly after milling of 10m distance. However, the surface roughness with angle 0° decreases after 6m of machining. They concluded, that the decrease in the surface roughness occurs because the center wear progresses at the tip of the ball end mill where the cutting speed is close to zero. When center wear appears, the new flat cutting edges are created in the tool geometry. Thus, micro ball end mill starts behave similarly to the flat end mill, which results in better surface finish. In general, it can be seen that tilting angle of spindle does not significantly affect surface roughness during micro ball end milling [33].

As we can see from discussion above, surface roughness generation depends on many factors, such as cutting parameters, utilization of the finishing and rough passes, presence of coolant and its type, presence of coating on the tool, geometrical characteristics of the tool, presence of wear and build-up edge (BUE), and other parameters. A lot of studies have been done in modeling and predicting of the surface roughness during macro ball end milling operations. In most of those studies geometrical approach has been used to describe surface characteristics. According to the geometrical approach the main parameters that affect surface roughness are chip load and tool radius.

Quintana *et al* [34] considered geometrical characteristics of the cut for mathematical modeling of the surface roughness in ball end milling process. According to their work, the maximum height of the mark (h_{max}) in the feed direction on the machined surface, which is shown in the Figure 20, can be estimated using following equation:

$$h_{max} = \frac{f_t^2}{8[R \pm f_t \times n_t/\pi]} \tag{2.6}$$

where

h_{max} : maximum height of the mark (mm)

f_t : chip load (mm/tooth)

R : radius of the ball end mill (mm)

n_t : number of flutes

The plus sign in the denominator of equation (2.6) is used for up milling, and the minus sign is used for down milling. According to equation (2.6) when larger chip load and smaller tool radius are used, then rougher surface is resulted.

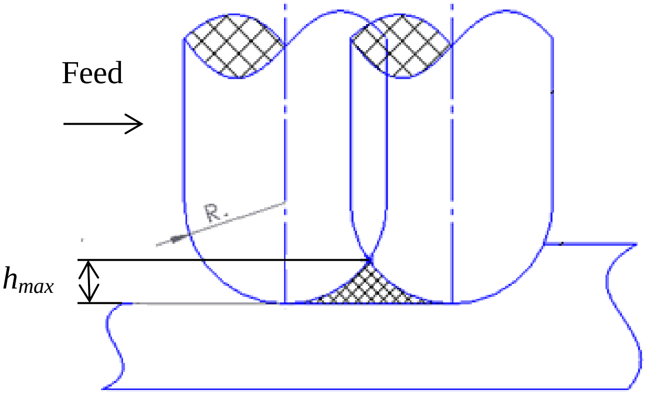

Figure 20. Maximum Height of the Mark (h_{max}) in the Feed Direction in Ball End Milling.

Other researchers in their work used new ridge method to derive mathematical model for predicting the surface roughness after ball end milling. They confirmed validity of their model with experimental results. According to their model the maximum height of the mark in the feed direction can be estimated as [35]:

$$h_{max} = R - \sqrt{R^2 - f_t^2} \tag{2.7}$$

where

h_{max} : maximum height of the mark (mm)

f_t : chip load (mm/tooth)

R : radius of the ball end mill (mm)

According to the work of Jung *et al* [35] the maximum surface roughness (h_{max}) after ball end milling of the flat surface can be calculated as a sum of heights of scallops ($H_{max,scallop}$) and cutters ($H_{max,\ cutter}$) (Figure 21):

$$h_{max} = H_{\mathrm{max},scallop} + H_{max,cutter} = \frac{f_p^2}{8R} + \frac{f_t^2}{8R} \tag{2.8}$$

where

h_{max} : maximum height of the mark (mm)

R : radius of the ball end mill (mm)

f_p : radial depth of one path (mm)

f_t : chip load (mm/tooth)

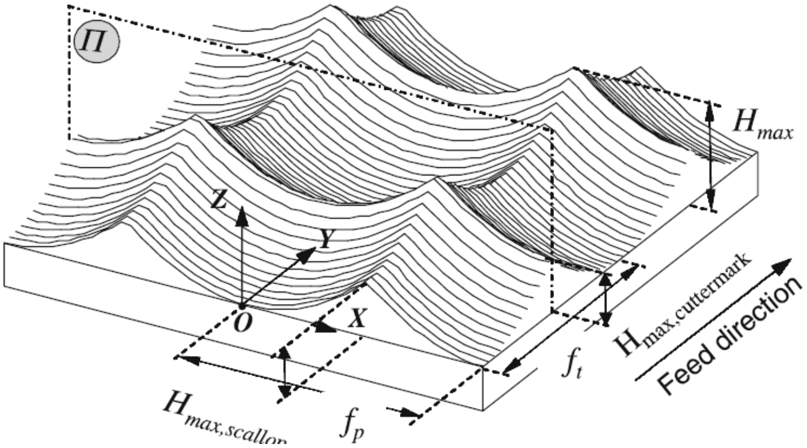

Figure 21. Surface Roughness Generation Prediction by Conventional Geometrical Model [35].

For slot milling, when only one path is applied, scallops do not form, therefore, equation (2.8) can be modified as to obtain following equation [35], [36]:

$$h_{max} = \frac{f_t^2}{8R} \tag{2.9}$$

Another geometrical model that can be used for estimation of surface roughness R_a during ball end milling is given bellow [37]:

$$R_a = \frac{0.0321(2f_t)^2}{R} \tag{2.10}$$

where

R_a : surface roughness (mm)

f_t : chip load (mm/tooth)

R : radius of the ball end mill (mm)

All the mathematical models listed above consider only geometrical characteristics of the cut to predict surface roughness. Also, it was assumed that the tool is in a good or nearly new condition. However, as the tool wear occurs and build-up edge forms during machining, it leads to the change of the tool geometry. Thus, the surface roughness starts being affected by these changes in tool geometry, and the machined surface becomes rougher. Li *et al* [32] created a model for surface roughness prediction during micro flat end milling that includes effect of tool wear. The toolwear progresses with increasing of cutting speed and material removal volume, which leads to the deteriorating effect on the surface finish. The surface roughness model with effect of wear is given below [32]:

$$R_a = K_{Ra} \times Ra_0 \tag{2.11}$$

$$Ra_0 = function(f_t, R) \tag{2.12}$$

$$K_{Ra} = C_{Ra} \times V^m \times MR^n \tag{2.13}$$

where

K_{Ra} : coefficient that takes into account effect of the wear on surface roughness

Ra_0 : theoretical surface roughness predicted by geometrical model (mm)

V : cutting speed (mm/min)

MR : material removal volume (mm^3)

C_{Ra}, m, n : coefficients from Taylor's model, that are obtained empirically for a particular cutting conditions

Li *et al* [32] validated their model shown in equations (2.11) - (2.13) and experimentally determined coefficients C_{Ra}, m, n for micro slot milling of OFHC Copper with Ø100µm tungsten carbide flat end mill. The equation (2.13) was modified to the following equation:

$$K_{Ra} = 0.1882 \times V^{0.67} \times MR^{0.59} \tag{2.14}$$

2.5 Burr Formation in Micromilling

The burrs formed during micromilling are very small in size and are much more difficult to be removed compared to the larger burrs that form after macromilling. Although, deburring techniques such as electrochemical polishing can be utilized to remove micro burrs, they require consumption of additional machining time and are costly [18]. It is very difficult to prevent burr formation, but it can be reduced when applying proper cutting conditions such as machining in minimum quantity lubrication and utilization tools with hard coatings [27].

Hashimata *et al* [38] in their study suggested classification for different types of burrs that can form during slot milling. The types of burrs depend on their location and are shown in the Figure 22. The burrs that are formed at the edge of the slot floor when tool enters or exits the work piece are called entrance and exit burrs, respectively. Similarly, the burrs that are created on the side edges, in the beginning and the end of the slot, are called entrance and exit side burrs, respectively. Finally, the type of burr that is formed on the top edge of the channel during slot milling is called top burr.

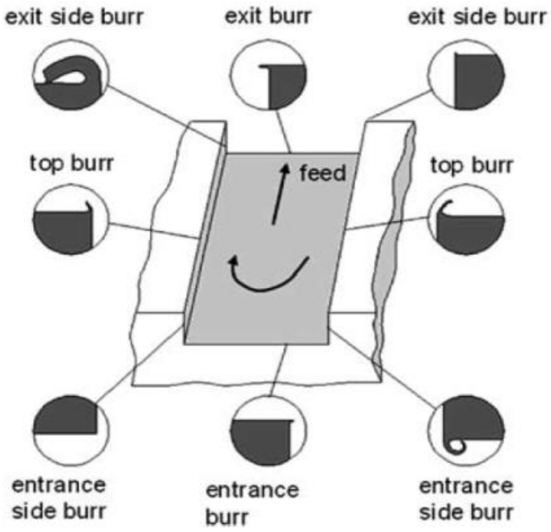

Figure 22. Types of Burrs Formed during Slot Milling [38].

According to Schueler *et al* [18], all listed above types of burrs form during slot micro end milling of Ti6Al7Nb titanium alloy. Figure 23 shows burrs that were formed during slot micro end milling of Ti6Al7Nb with tungsten carbide micro end mill of diameter Ø48µm. They observed that the size of the top burrs is much large in micromilling compared to macromilling due to the size effect. During slot micromilling material is moved towards the top surface of the workpiece by high compressive stress, which leads to the formation of the top burrs. The size of the exit and entrance burrs are very similar and are smaller than size of the top burrs. However, exit side burrs are larger than the entrance side burrs. According to their study, the burr formation and its size are not affected by the method of milling – down or up milling, which can be seen from Figure 24 [18].

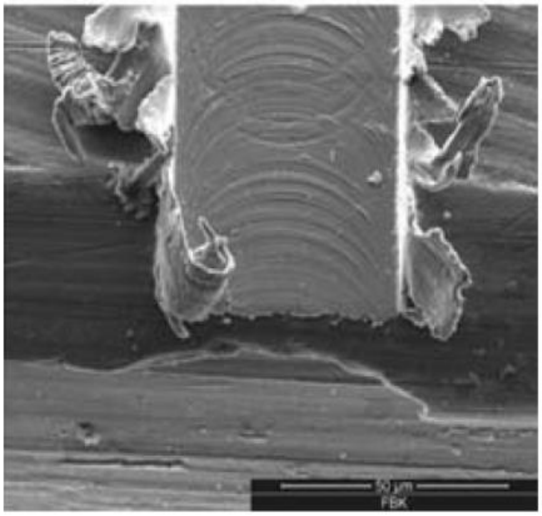

Figure 23. Types of Burrs Formed during Slot Micro End Milling of Ti6Al7Nb Titanium Alloy (Axial Depth 20µm; Cutting Speed 9.05 m/min, Chip load 0.084 µm/tooth) [18].

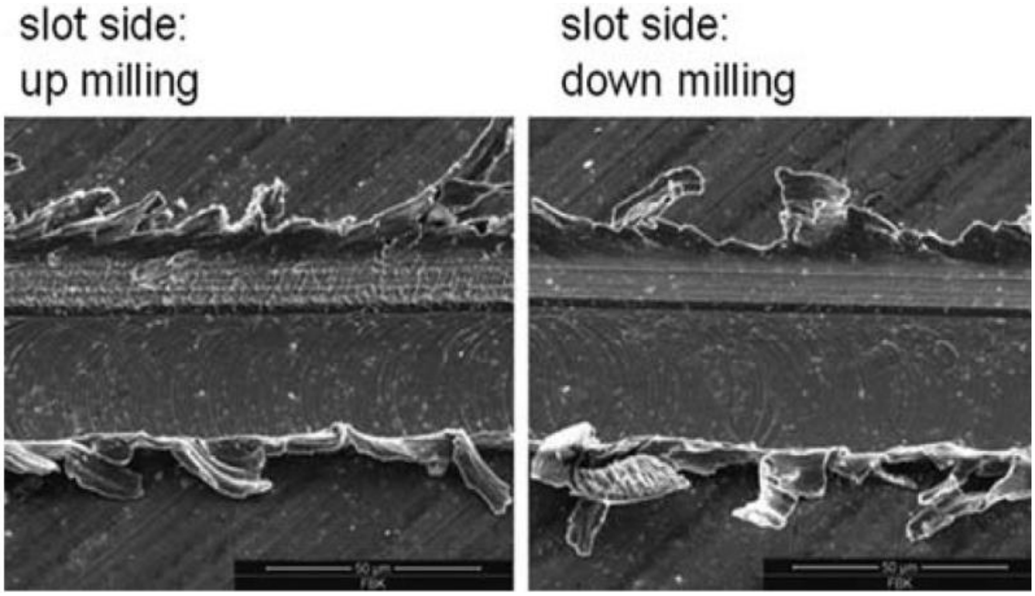
slot side: up milling

slot side: down milling

Figure 24. Effect of the Milling Method (Up and Down Milling) on the Burr Formation during Slot Micro Milling of Ti-6Al-7Nb (Axial Depth 20µm; Tool Diameter 48µm; Cutting Speed 9.05 m/min, Chip Load 0.084 µm/tooth) [18].

2.6 Cutting Fluid in Micro Machining

Cutting fluid is applied during machining to increase tool life, enhance surface finish, decrease burr, and build-up edge formation. When properly used, the coolant decreases temperature, decreases friction, and removes chips from the cutting zone. As opposed to the conventional macro machining, highly pressurized flood coolant cannot be used during micromachining, since high pressure of the cutting fluid can affect cutting process by deflecting the microtool. Therefore, new cooling technique such as minimum quantity lubrication (MQL) is used during micromachining [10].

MQL is a cooling method where mist is sprayed from the nozzle on the tip of the cutting tool. Utilization of the MQL instead of the flood cooling or dry cutting condition leads to advantages such as effective wetting, better machined surface quality, lower tool wear and build up edge formation, lower cost, lower environmental pollution, and lower health risk of the machinist [39]. Figure 25 shows slots machined on NiTi alloy and tool conditions after machining for two milling conditions: (a) cutting with MQL and (b) dry cutting. It can be seen form the figure that when MQL is used, the formation of burrs on the surface and the formation of the buildup edge on the tool decrease significantly [10]. Figure 26 shows how different cooling conditions affect the tool wear. It is obvious that the utilization of the MQL results in the lowest tool wear compared to the flood cooling and dry cutting conditions [40].

Other study shows that when minimum quantity lubrication is properly used in micromilling of 316L stainless steel, the formation of build-up edge can be decreased and tool life can be significantly increased (up to 100 times) compared to dry machining (Figure 27) [41].

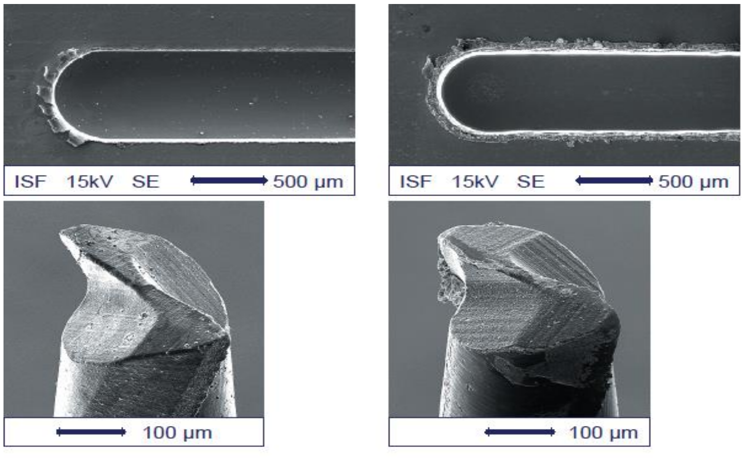

(a) MQL (b) Dry

Figure 25. Slot Micro Milling with MQL and without Coolant (Workpiece – NiTi, Axial Depth 10μm; Tool Diameter 400 μm; Cutting Speed 33 m/min, Chip Load 12 μm/tooth) [10].

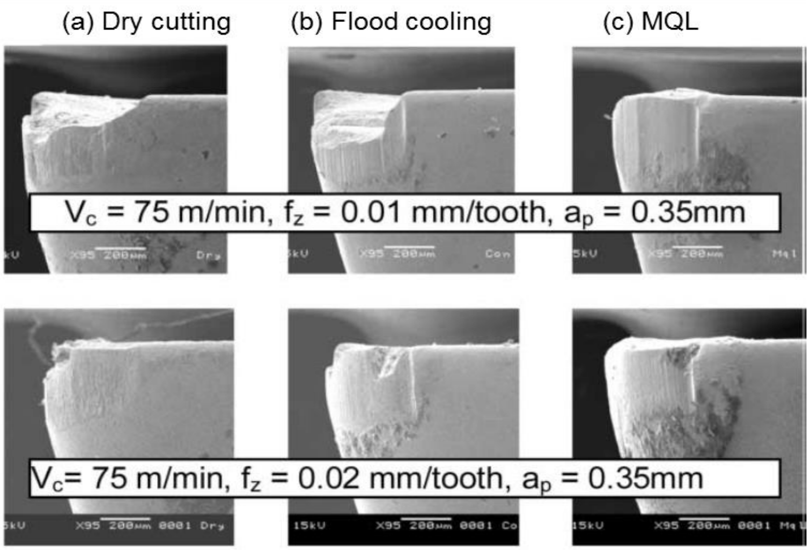

Figure 26. Tool Wear Dependence on the Different Cooling Conditions [40].

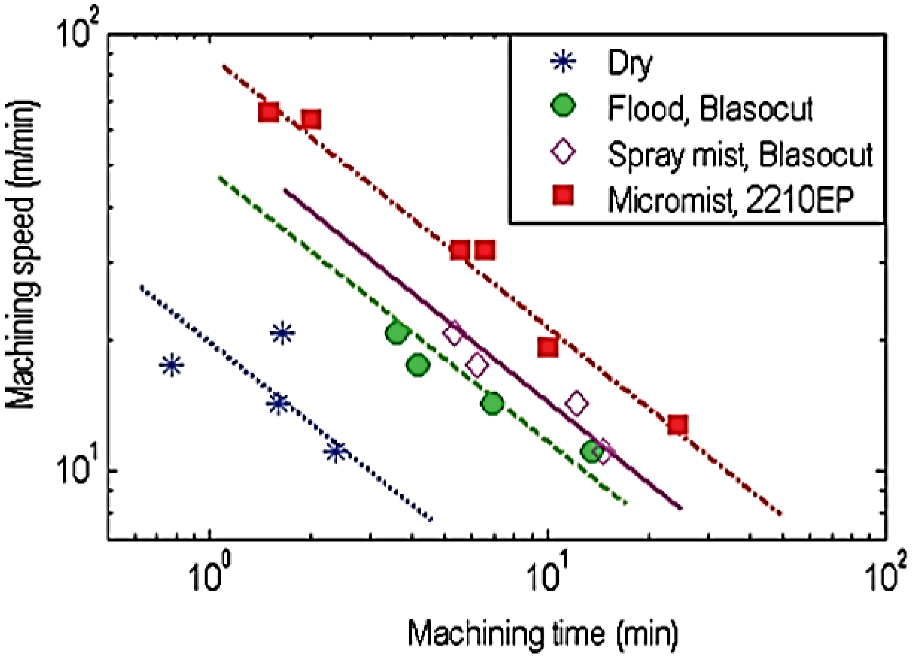

Figure 27. Effect of Cutting Fluid on Tool Life in Micromilling of 316L Stainless Steel. 10µm/tooth Chip Load, 0.348mm Axial Depth, 0.558mm Radial Depth, Ø1.016mm Tool **[**41**]**.

2.7 Tool Coatings

Hard coatings are used on the tools to provide higher hardness and wear resistance of the outer layer of the tools. In the most cases the utilization of the coatings leads to more efficient cutting process, lower wear, lower burr size, less build-up edge, and smoother surface finish. Many types of physical vapor deposition coatings are available for micro tools. However, limited studies have been done on their effectiveness during micro machining operations. The thickness of the coating layer for micro tools is smaller (1.5±0.15µm) than it is for macro tools (2-3µm). The characteristics of different coating types are show in the Table 1 [14].

Table 1. Coating Characteristics [14].

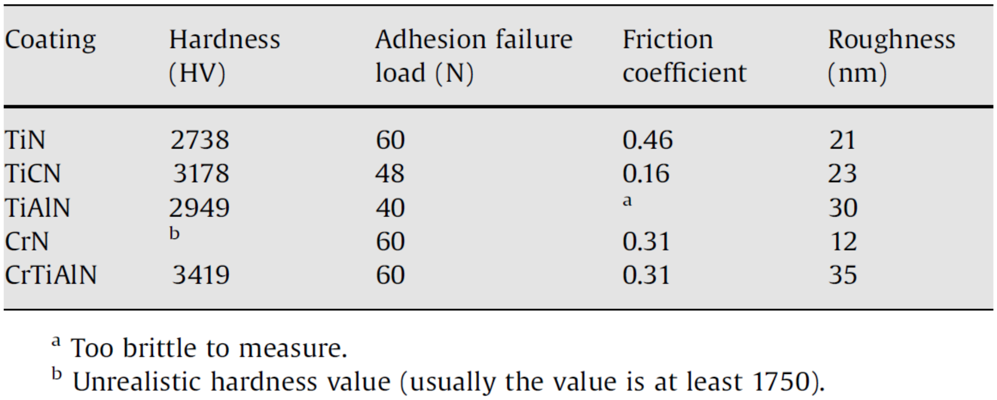

Coating	Hardness (HV)	Adhesion failure load (N)	Friction coefficient	Roughness (nm)
TiN	2738	60	0.46	21
TiCN	3178	48	0.16	23
TiAlN	2949	40	[a]	30
CrN	[b]	60	0.31	12
CrTiAlN	3419	60	0.31	35

[a] Too brittle to measure.
[b] Unrealistic hardness value (usually the value is at least 1750).

Aramcharoen *et al* [14] investigated the effect of different types of coating such as TiN, CrN, TiCN, TiAlN and CrTiAlN on the wear, burr formation, and surface roughness during micro end milling of the tool steel with 500µm micro tools. The effect of the coating on the chipping of the tool is shown in the Figure 28. According to their results, all types of coating decrease chipping of the tools, and coating TiAlN provides lowest chipping. Coating CrN shows low resistivity to chipping, since this kind of coating has higher chemical reactivity with tool steel – material of the workpiece.

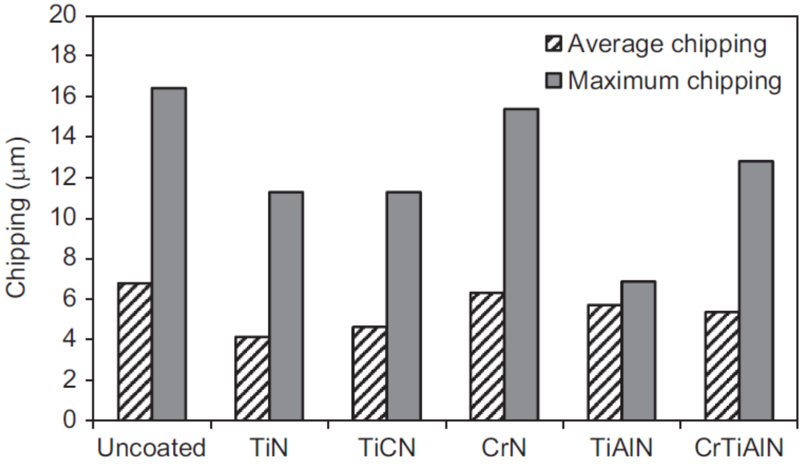

Figure 28. Effect of the Coating on the Chipping of the Micro Tools when Machining Tool Steel [14].

The effect of the different coating types on the surface roughness is shown in the Figure 29. There is no significant difference in the surface roughness between coated and uncoated tools at the beginning of the machining (0-5 mm machined length). However, at the end of the machining (after 20 mm machined length) the highest surface roughness is observed for the uncoated tools, and TiCN and CrN coated tools, because flank wear progresses on the uncoated tool, and the coating is removed from TiCN and CrN coated tools.

The average width of the burrs formed during micro milling with different coatings is shown in the Figure 30. In general utilization of the coating, except TiAlN coating, leads to the decrease of the of the burr size [14].

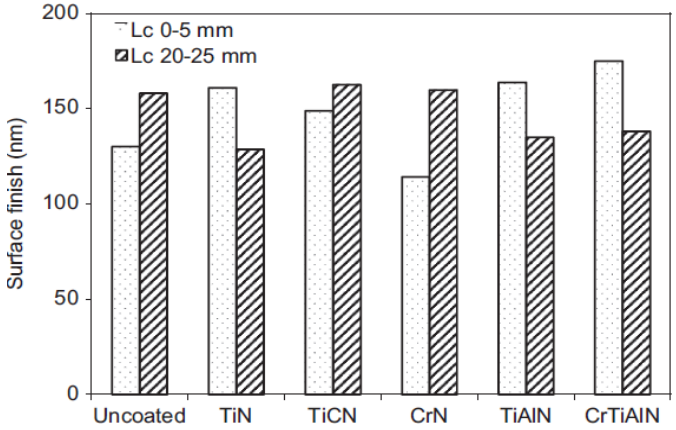

Figure 29. Effect of the Coating on the Surface Roughness when Machining Tool Steel [14].

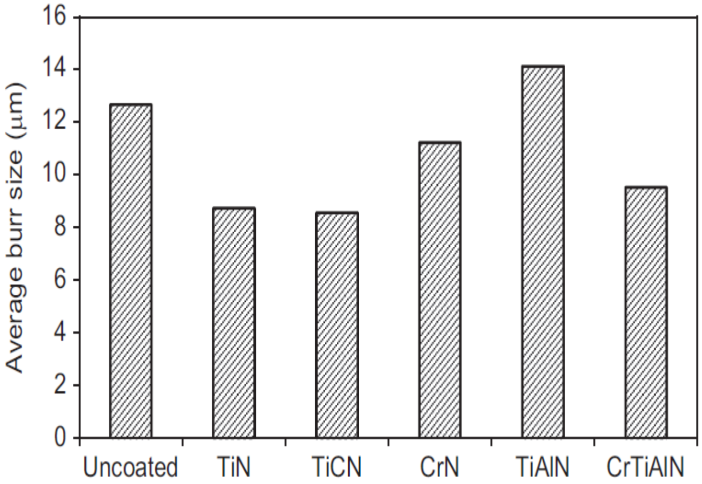

Figure 30. Effect of the Coating on the Average Burr Size when Machining Tool Steel [14].

3. EXPERIMENTS

The scope of the experiments included:

i. Developing and optimizing of milling process to fabricate smooth, deep, and complex microchannel patterns.
ii. Analyzing of surface quality of milled channels after ball end milling.
iii. Identifing technique to enhance surface finish of milled microchannels.
iv. Developing a model to predict surface roughness after ball end milling, validating it with experimental data, and comparing with other models from literature.

Ball end milling of the micro and meso channels were performed on different materials at different cutting parameters in minimum quantity lubrication. The experimental data was used to derive an empirical surface roughness model and compared against theoretical values.

3.1 Materials

Micromilling experiments were performed on NiTi alloy, 304 stainless steel, and 316L stainless steel. Mesomilling experiments were performed on 6061-T6 aluminum alloy and 36A low carbon steel to complement surface finish data. The properties of the materials used for the experiments are given in the Table 2. Chemical compositions of alloys are provided in the Table 3. NiTi alloy and 316L stainless steel were selected for micromilling experiments because they are biocompatible materials and are often used for medical applications. NiTi alloys are also very often used for medical implants and are of current interest for many researchers due to their shape memory effect caused by the martensitic phase transformations. Although biocompatible materials were the prime focus of the research other engineering materials such as 6061-T6 aluminum alloy and 36A low carbon steel were machined to complement surface finish data.

Table 2. Properties of the Materials of the Workpieces [6], [39], [42].

Material	Ultimate tensile strength, MPa	Yield strength, MPa	Modulus of elasticity, GPa	Elongation, %	Rockwell B Hardness	Density, g/cm^3	Melting point, °C
6061-T6	260-300	240-276	70-80	13	60 HRB	2.7	580
304 SS	520-720	210	193	31	92 HRB	8	1450
316L SS	485	170	193	40	95 HRB	8	1400
A36	400-550	250	200	20	85HRB	7.8	1400
NiTi (Martensitic)	103-1100	70-140	21-69	60	50-60 HRC	6.45	1310

Table 3. Chemical Composition of Materials [42].

Material	Chemical composition (weight %)
6061-T6	0.04-0.35 Cr, 0.15-0.40 Cu, <0.70 Fe, 0.8-1.2 Mg, 0.4-0.8 Si, <0.25 Zn, Remainder Al
304 SS	<0.08 C, 17.5-20.0 Cr, 8-11 Ni, <2 Mn, <1 Si, <0.045 P, <0.03 S, Remainder Fe
316L SS	<0.03 C, 16.0-18.5 Cr, 10-14 Ni, 2-3 Mo, <2 Mn, <1 Si, <0.045 P, <0.03 S, Remainder Fe
A36	0.25-0.29 C, <0.2 Cu, <1.03 Mn, <0.28 Si, <0.04 P, <0.05 S, Remainder Fe
NiTi	56.0 Ni, <2 Co, Remainder Ti

3.2 Tools

The experiments were conducted with micro ball end mills that were provided by Performance Micro Tool and Swiss-Tek coating. Some WC-Co mills were physical vapor deposited (PVD) with AlTiN by Swiss-Tek coating. The mill size varied from Ø152µm to Ø3.175mm. The characteristics of the micro tools are given in Figure 31 and Table 4. The mechanical properties of the fine grained tungsten carbide material are given in the Table 5.The characteristics of meso tools are provided in the Table 6.

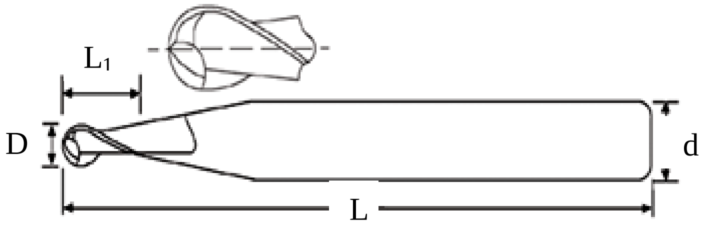

Figure 31. Two Flute Micro Ball End Mill [43].

Table 4. Characteristics of the Micro Ball End Mills [43].

Part number	*TR-2-0060-BN*	*SPS-2-0078-BN*
Material	Tungsten carbide	Tungsten carbide
Coating condition	Uncoated	AlTiN coated
Number of flutes	2	2
Cutter diameter (D), mm	$0.152^{+0}_{-0.127}$	$0.198^{+0}_{-0.012}$
Flute length (L_1), mm	$0.457^{+0.177}_{-0}$	$0.610^{+0.177}_{-0}$
Shank diameter (d), mm	$3.175^{+0}_{-0.0051}$	$3.175^{+0}_{-0.0051}$
Total length (L), mm	38.1 (±0.127)	38.1 (±0.127)
Cutting direction	Right Hand	Right Hand

Table 5. Properties of the Fine-Grained Microstructure Tungsten Carbide (WC) [44].

Grain size, µm	Cobalt content, mass %	Hardness		Fracture toughness (K_{IC}), MPam$^{1/2}$	Transverse rapture strength, GPa	Young's modulus, GPa
		HRA	HV			
<0.6	7	94	1930	5.8	4.0	590

Table 6. Characteristics of the Meso Ball End Mills [45].

Part number	*07761133*	*09137530*
Material	Tungsten carbide	Tungsten carbide
Coating condition	Uncoated	AlTiN coated
Number of flutes	4	4
Cutter diameter, mm	3.175	3.175
Flute length, mm	12.7	12.7
Shank diameter, mm	3.175	3.175
Total length, mm	38.1	38.1
Tool type	Right Hand	Right Hand

3.3 Equipment

3.3.1 Milling Machine

The HAAS OM2 milling machine was used to perform micro and meso milling experiments. The shank of the tools was mounted in the collet, which is recommended type of tool holder during micro milling, since it provides low value of tool runout. The HAAS milling machine had air bearing spindle and the three degrees of freedom (X, Y, and Z axes), which was sufficient to perform all experiments. The detailed specification is provided in APPENDIX A.1.

UNIST cool lubricator system was used on the HAAS OM2 milling machine to provide micro mist cooling and lubrication of the tool and workpiece during cutting process. The minimum quantity lubrication was used in order to increase tool life and provide lower surface roughness of machined components. The tool life is increased due to reduction of heat generated in the cutting zone, and due to reduction of the friction between the chip and the tool, as well as between the tool and the workpiece. UNIST micro mist Coolube 2210 was utilized for all machining experiments. The specification of the UNIST cool lubricator system is provided in APPENDIX A.2.

3.3.2 Metrology Equipment

- *Keyence CCD Laser Displacement Sensor LK-G Series*

The Keyence laser displacement sensor was used to measure the height of the washer with attached to it a single sided sticky aluminum foil, which was used to set z-offset of the micro tool prior to the machining. The laser was selected for the measurements since it provided high accuracy and repeatability, which was required for micromachining experiments. The resolution of the laser was 0.1 µm. The other reason for using Keyence laser is that it is a non-contact measuring tool, which was also required. It was important not to bend or not to make even micro dent on the foil attached to the washer while measuring its height, because the micro dent would affect the accuracy of setting of z-offset, and, consequently, the accuracy of the machined channel. While setting z-offset of the tool, the micro end mill was moved to make contact with the foil attached to the top surface of the washer. Hard piece could not be used instead of the washer with the foil, since it was possible to break a fragile microtool with even a slight contact to any hard components. Thus, it was required to measure the height of the washer with aluminum foil only at its middle, because only this location could prevent the breakage of the tool while setting z-offset. In addition, Keyence laser was used to measure runout and vibrations of the microtools. Detailed specification of Keyence CCD laser is provided in APPENDIX A.3.

- *Olympus STM 6 Optical Microscope*

Olympus STM 6 Optical Microscope was used for the tool wear measurements on micro and meso ball end mills, and for the observing the machined surfaces and their quality. DP 70 12.5 megapixel camera was installed on the optical microscope, which provided ability to take and save optical images. These images were transferred to SolidWorks software for further analysis. The resolution of the optical microscope was 0.1µm, which was a sufficient for all measurements. Depending on the desired magnification, different objective lenses in the range 1.25x - 50x were used for the measurements. The objective lens and the table of the optical microscope could move along three axes (X, Y, and Z). The motion along each axis could be done in coarse or fine modes.

- *JEOL6400 Scanning Electron Microscope*

Scanning Electron Microscope (SEM) was utilized to observe the surface topography of machined micro slots and conditions of micro tools. It provided ability to create images with higher magnification than of those with optical microscope. Prior to measuring with SEM, the samples were cleaned ultrasonically in alcohol and dried with pressurized air in order to remove microchips and residues of oil from the micro mist. During measurements the samples were placed in the chamber, in which vacuum was formed using a pump. The detection of emitted secondary electrons (SE) and backscattered electrons (BSE) was used to create SEM images.

- *Zygo NewView 100 Interferometer*

Zygo interferometer was used to measure surface finish of the machined micro and meso channels. It was selected for surface roughness measurements because of its high accuracy. The accuracy on the order of hundredth of micron was required for the measurements. The resolution of the interferometer was 0.1 nm. Also, the utilization of a non-contact technique for surface roughness measurements was mandatory for micro components. In order to provide accurate measurements the surface of the samples had to be reflective, which was not an issue, since all materials of the work pieces were metals with high reflectivity. Zygo interferometer completely met above mentioned requirements.

The computer with two monitors were installed and connected to the Zygo NewView 100 microscope. Zygo joystick box was utilized to control direction and motion speed along X, Y, and Z axes during measurements. Zygo MetroPro software was used to analyze the measured three dimensional surface profiles and provided ability to measure different types of surface roughness such as R_a, R_z, and R_t. Also, it provided the information about the distribution of the surface heights on three different plots such as filled plot, oblique plot, and profile plot. Depending on the necessary magnification three sizes of objective lens (2.5x, 5x, and 10x) could be used on the Zygo microscope. Bipolar scanning depth (length) could be adjusted in range 10µm -100µm depending on the measured profile. The detailed specification of Zygo NewView 100 interferometer is provided in APPENDIX A.4.

- *Raytec Rayngers ST Pyrometer*

Raytec Rangers ST pyrometer was used to measure temperature of the aluminum block when it was being heated up on the hot plate for gluing the samples to its surface with heat activated wax. The utilization of the infrared non-contact thermometer was required in order to provide safe measurements, since the temperature of the aluminum block was approximately 80°C and the temperature of the hot plate was about 400°C. The temperature of the hot surface was measured without touching it with pyrometer by detecting the amount of the emitted electromagnetic radiation. The detailed specification of the Raytec Rangers ST pyrometer is provided in APPENDIX A.5.

3.4 Procedure

3.4.1 Tools

Prior to the machining the conditions of the new micro and meso tools were checked using optical microscope in order to detect any manufacturing defects and eliminate their effect on the experimental results. The images of each tool were taken using optical microscope before and after the experiments in order to keep records of tool conditions. Before making any observations using optical microscope, the tools were cleaned ultrasonically with isopropyl alcohol for 3-5 minutes and dried with pressurized air. Ultrasonic Cleaner Metason 200 was used to remove residues of oil, small pieces of dirt, and small metal particles from the tools. The ultrasonic cleaner generated a high-frequency voltage that produced ultrasonic waves in the alcohol, and led to the formation of the vacuum micro bubbles. When bubbles hit the surface of the tools, they broke and released a burst of energy. Due to the high release of energy, the dirt was removed from the tools. The specification of Ultrasonic Cleaner Metason 200 is provided in APPENDIX A.6.

After cleaning and observation with the microscope, the tool was mounted in the collet of the HAAS OM2 CNC Milling Machine. This had to be done carefully to avoid any contact with the tool tip, since any contact could result in its damage or breakage. Then, the tool positioning was performed in order to set X, Y, and Z offsets. The coordinate system and the positive directions of each axis used for programming on the HAAS OM2 CNC milling machine is given in the Figure 32. The positioning of the tool along Z axis was critical for micro milling experiments. Z offset had to be set accurately and precisely, since it had a direct effect on the consistency of the axial depth of cut. Thus, the precise technique was developed and used to set Z-offset of the tool. The procedure to set Z offset of the tool was performed as follows:

1. Flat surfaces of the washer with diameter 15 mm was ground using sandpaper in order to remove all burrs and provide flatness.
2. Single sided sticky aluminum foil was attached to one flat side of the washer. Aluminum foil was used because it is electrically conductive, which was required.

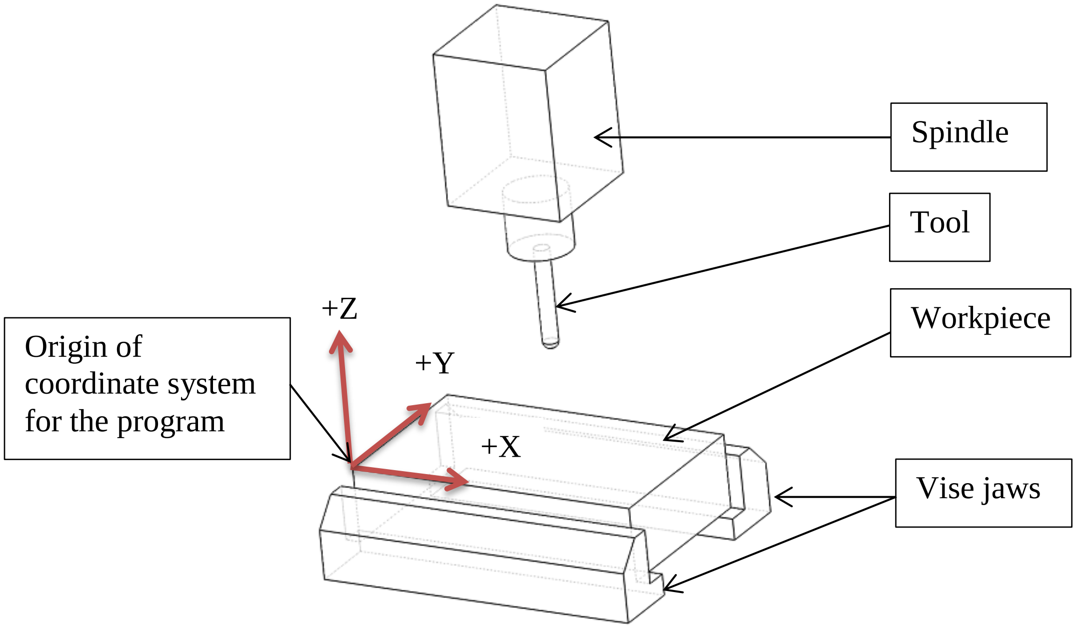

Figure 32. Coordinate System of the Workpiece on the HAAS OM2 CNC Milling Machine.

3. The point that corresponded to the middle of the washer was marked on the foil with a marker.
4. Keyence Laser Displacement Sensor was used to measure the height of the washer at the marked location, as it is shown in the Figure 33. Prior to measuring, tuning of the Keyence laser was performed to set the reflectivity of the aluminum foil. The height of the washer was measured repeatedly 20 times at the same location and the average value was calculated.
5. The workpiece was mounted in the vise and its top surface was cleaned with compressed air.
6. The metal washer was placed on the top surface of the workpiece.

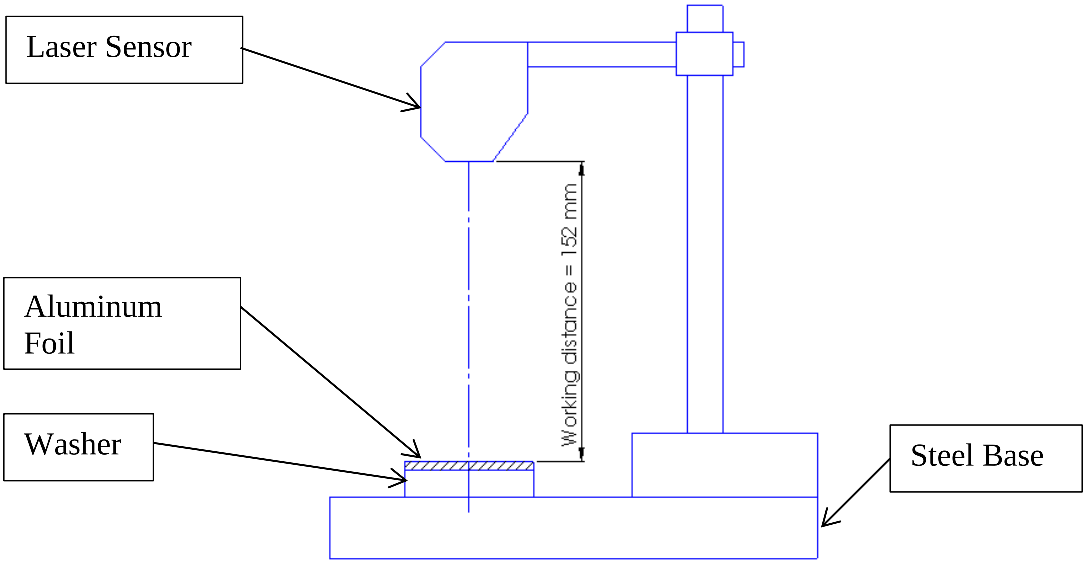

Figure 33. Schema of Height Measurements with Keyence Laser Displacement Sensor.

7. Microtool was mounted in the collet of the milling machine.
8. The tool was moved in X and Y directions using hand jog on the milling machine in order to place its tip directly above the marked point at the center of the washer.
9. The digital multimeter was connected with a wire connector to the aluminum foil on the washer and with another wire connector to the shank of the microtool. The multimeter was used to measure the resistivity change once the tool touched the foil on the washer and closed the circuit. The connection of the multimeter to the tool and aluminum foil for Z offset setup is shown in the Figure 34.
10. Tool was moved downwards slowly, and was rotated manually until it made

contact with the aluminum foil at the marked pint. The manual rotation of the tool was necessary to provide better contact between the tool tip and the foil and in order to prevent bending of the foil. It was not possible to observe this contact with the naked eye, but the contact was indicated on the multimeter since the resistivity suddenly changed and the multimeter produced the beeping noise.

11. Z value was highlighted in the “Work Zero Offset” menu in G54 line on the display of the HAAS OM2 CNC milling machine, and “Part zero set” button was pressed to record current position as a coordinate origin in Z direction.
12. The value of Z coordinate was read form the coordinate display. The height of the washer with aluminum foil was subtracted form that value using numerical keypad of the milling machine, since tool was located above the workpiece.

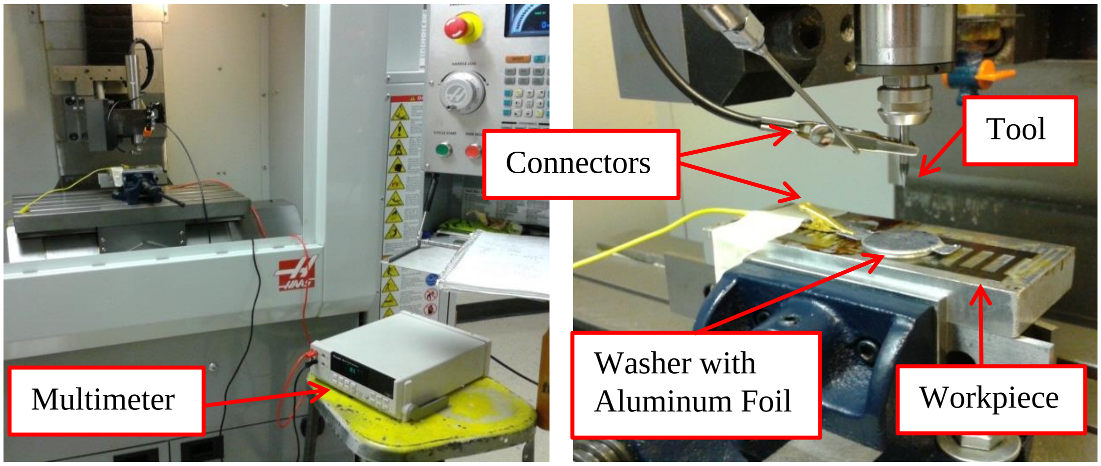

Figure 34. Setup for the Setting Z Offset of Microtool using Multimeter.

High accuracy and precision was not required for setting X and Y offsets, since the distance between each new machined channel was 1-2 mm, which was about 10 times larger than the diameter of the microtools. Also, the depth of cut was not affected by the accuracy in setting X and Y offsets. The procedure to set up X and Y offsets of the tool was performed as follows:

a. The plug gage with diameter 3.175 mm was secured in the collet of the milling machine. The plug gage was used instead of the micro tool in order to prevent its damage or breakage while setting an offset.

b. The table of the milling machine was moved to sandwich the rubber washer of thickness 2.667mm without deforming it between the workpiece surface and the plug gage as it is shown in the Figure 35.

c. X (or Y) value was highlighted in the “Work Zero Offset” menu in G54 line on the display of the HAAS OM2 CNC milling machine, and “Part zero set” button was pressed to record current position as a coordinate origin in X (or Y) direction.

d. The value of X (or Y) coordinate was read form the coordinate display. The thickness of the rubber washer was added to that value using numerical keypad of the milling machine, since the spindle was located on the left side of the workpiece for X axis (or in front of the workpiece for Y axis).

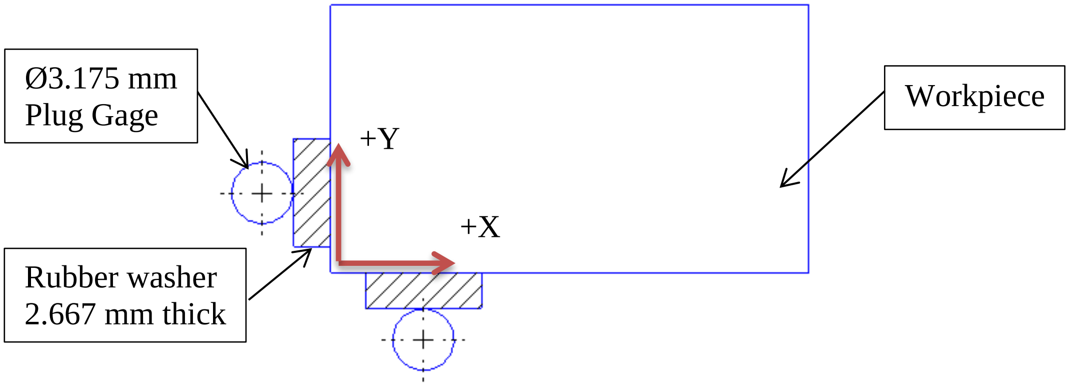

Figure 35. Setting X and Y Offsets Using the Plug Gage.

3.4.2 Workpieces

The samples for micromilling experiments were cut from 0.5-1.0 mm sheets of CP titanium, NiTi alloy, 304 and 316L stainless steels using AgieCharmilles wire-type electrical discharge machining. Detailed specification of AgieCharmilles wire-type electrical discharge machine is provided in the APPENDIX A.7. A simpler shearing process was not used to cut samples in order to avoid bending them. Since the tolerance of parallelism was extremely critical for micro machining, even small bending of the samples could result in large deviation in the depth of cut within the same sample. The configuration and dimensions of the stainless steel sample are given in the Figure 36. This shape of the sample was selected to provide the ability to mount them while the electrochemical polishing operations that followed the micromilling of the channels.

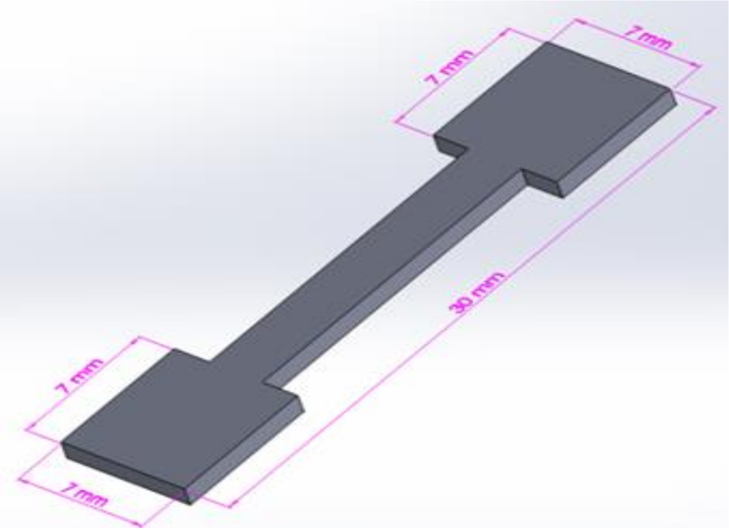

Figure 36. Configurations and Dimensions of the Samples from 304 and 316L Stainless Steels used for Micro Milling.

Since the thickness of the samples was too low to mount them in the vice, first they were glued to the larger aluminum block that was preliminary machined using larger HAAS VF1 CNC milling machine. The detailed drawing of the aluminum block is provided in the APPENDIX B.1. The top surfaces of the block, that the samples were glued to, were machined on the HAAS OM2 CNC milling machine, the same machine used to perform the micromilling experiments for accuracy and parallelism.

The samples were glued to the top surface of the aluminum block using heat activated wax. The procedure of gluing was performed as follows:

1. 70% isopropyl alcohol and cotton swabs was utilized to clean the surfaces of the block and samples in order to remove oil and create high quality glued joint.
2. Aluminum block was placed on the top surface of the Waage Electric Stove hot

plate with the side prepared for gluing facing up. The aluminum block was heated up to the temperature 60-80°C. The Raytec Rayngers ST pyrometer was used to measure temperature of the top surface of the block as it is shown in the Figure 37.

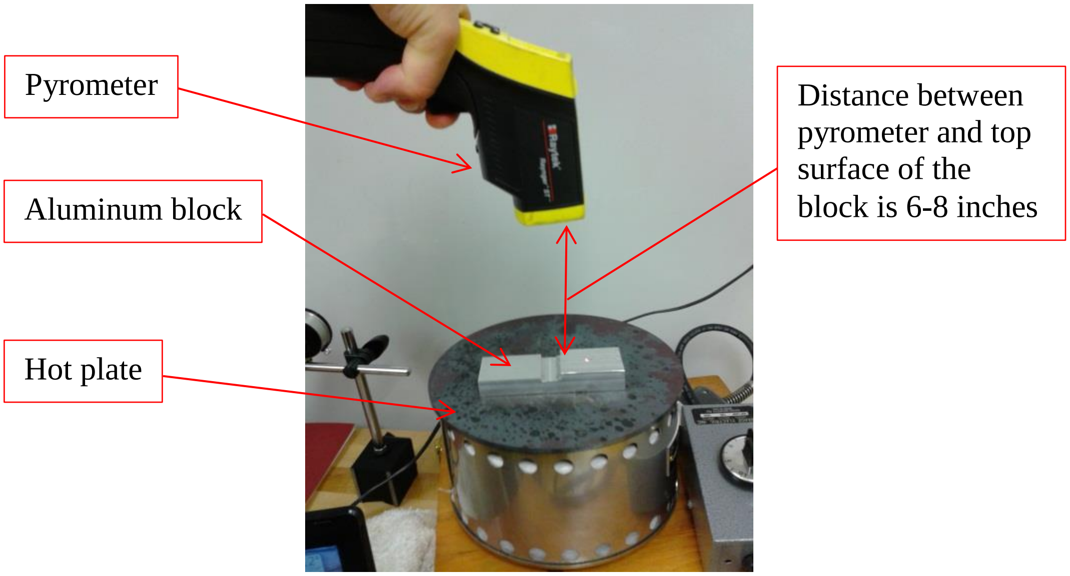

Figure 37. Temperature Measurements with Pyrometer while Gluing with Heat Activated Wax.

3. Uniform layer of mounting quartz type sticky wax P/NMWM070 was applied on the hot top surface of the block by touching it with hard wax. The wax was melting and transforming from the solid state to the viscous liquid state at temperature 60-80°C. The final uniform thickness of the wax on the top surface of the block was approximately 0.5 mm.

4. The samples were placed in desired location on the top of the block using the tweezers.
5. After all of the samples were aligned, the block was removed from the hot plate.
6. The weight was applied on the top surfaces of the samples in order to squeeze them together.
7. The block with samples was left for 2 hours at room temperature to let wax solidify.
8. Residue of the wax was removed from the top surfaces of the samples using acetone and cotton swabs.

The parallelism of the top surface of the workpiece was measured with dial indicator when it was place on the parallel bars and secured in the vise on the HAAS OM2 CNC milling machine. The schematic representation of the parallelism measurements is shown in the Figure 38. The measured value of the parallelism was lower than 0.020 mm, which was sufficient to guarantee the necessary accuracy for both micro and mesomilling experiments.

Larger aluminum and low carbon steel samples for meso milling experiments were preliminarily machined on the lager HAAS VF1 CNC milling machine to the dimensions 75mm x 40mm x 18mm and 75mm x 50mm x 13mm respectively. Sharp edges on the samples were deburred using the file. Preliminarily machining was performed to guarantee low tolerance of parallelism of the samples.

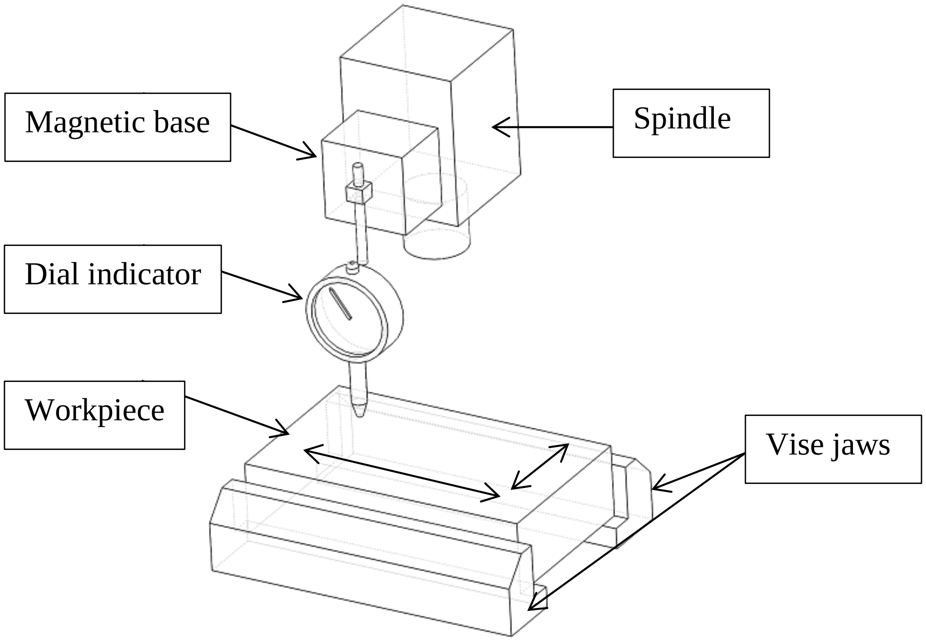

Figure 38. Schematic Representation of Parallelisms Measurements.

3.4.3 Micromist

It was important to set the micro mist direction properly to provide effective micro machining and generate high quality surface. Thus, before the beginning of each machining experiment, the coolant nozzle was set according to the angles that are shown in the Figure 39 and Figure 40. This set-up provided maximum contact surface between the coolant spray and the cutting tool. The coolant nozzle was directed at the tip of the tool, and located 30 mm away from it. The angle θ, which was between Z axis of the milling machine and nozzle, was set to 60°. The angle ϕ, which was between X axis of the milling machine and the nozzle, was set to 55° [6].

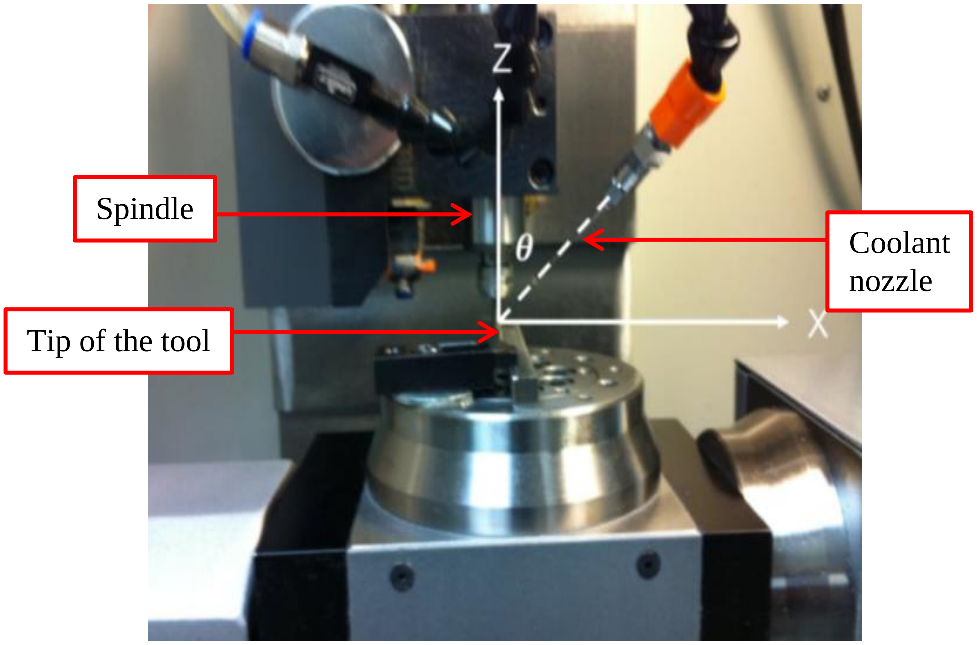

Figure 39. Coolant Nozzle Positioning (Front View) [6].

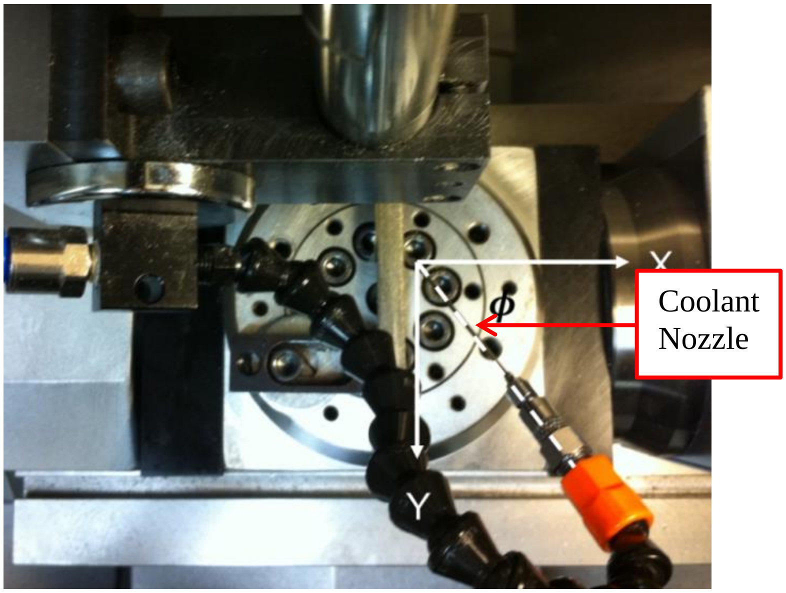

Figure 40. Coolant Nozzle Positioning (Top View) [6].

3.4.4 Tool Vibration and Runout Measurements

Tool runout measurements were performed in order to check spindle and tool runout and feasibility of the milling machine for the experiments. The Keyence displacement laser was used to measure deflection of the microtool. The laser was connected to the data acquisition card DAC National Instruments NI USB-6008, which provided sampling rate 10kHz. Set-up of the tool runout measurements is shown in the Figure 41. Data was collected using LabVIEW software for three different conditions: (1) rotating spindle without machining, (2) machining with depth of cut 0.038mm, and (3) machining with depth of cut 0.076mm. Tungsten carbide micro ball end mill Ø 152µm with two flutes and CP titanium workpiece were used for machining. The cutting conditions for the experiments are given in the Table 7. The CNC code that was utilized for the experiment is provided in the APPENDIX C.4. After raw data was collected, fast Fourier transform (FFT) plots were built to provide better visualization of the frequency spectrum.

Table 7. Cutting Conditions for Runout Measurements.

Depth of cut, µm	Cutting speed, m/min	Chip load, µm	Spindle speed, rpm	Feed rate, mm/min
38	13	0.05	27500	2.7
76				
38	13	0.1	27500	5.5
76				
38	20	0.05	41904	4.2
76				
38	20	0.1	41904	8.4
76				

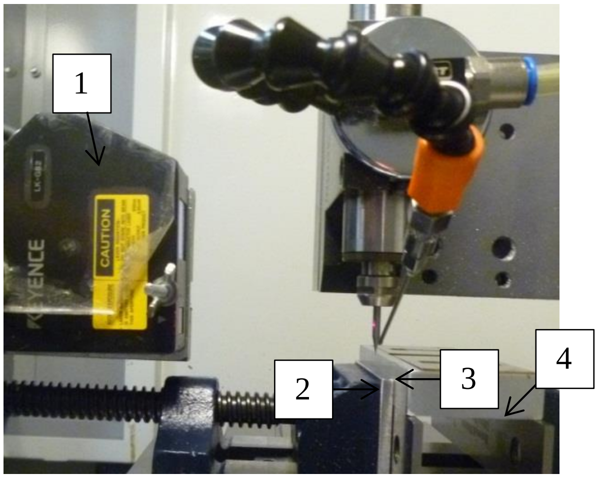

Figure 41. Set-up of the Tool Runout Measurements on HAAS OM2 Micromilling Machine with Keyence Displacement Laser: (1) Keyence Laser; (2) Micro Ball End Mill Ø0.152mm; (3) Coolant Nozzle; (4) Workpiece.

3.4.5 Micromilling

Prior to the milling experiments, every micro and meso tool was examined using optical microscope according to the procedure described in the section 3.4.1. The examinations of the tools were done to detect any manufacturing defects and prevent their effect on the experimental results. The number was assign to each tool to keep tracking of the tools. The collet of the milling machine was cleaned with pressurized air. Tool was mounted in the collet avoiding of any contacts with the fragile tip of the tool. The workpiece was placed on the parallel bars and tightened in the wise. The tool-workpiece positioning was performed according to the procedure described in the section 3.4.1. The coolant nozzle orientation was set as it was described in the section 3.4.3. UNIST cool lubricator system was turned on before start of the milling. The paper was placed in front of the coolant nozzle in order to check the presence of the micromist.

Prior to each machining experiment, milling machine was warmed up using warm up program which is provided in the APPENDIX C.1. The warming up was performed in order to decrease wear of the spinning parts of the spindle.

The schematic representation of micro milling experiments is shown in the Figure 42. Two perpendicular slots were milled on a specimen at particular cutting conditions. The slot length was set at 12 mm for 304 stainless steel and 316L stainless steel, and 8 mm for NiTi alloy. Each pair of cross slots was machined with a new tool. The tool trajectories were drawn using SolidWorks software. CNC programs were written for each experiment according to the tool trajectories. The CNC programs for all experiments are provided in the APPENDIX C. The correctness of each program was validated by plotting a trajectory graph on the coordinate display screen of the CNC milling machine.

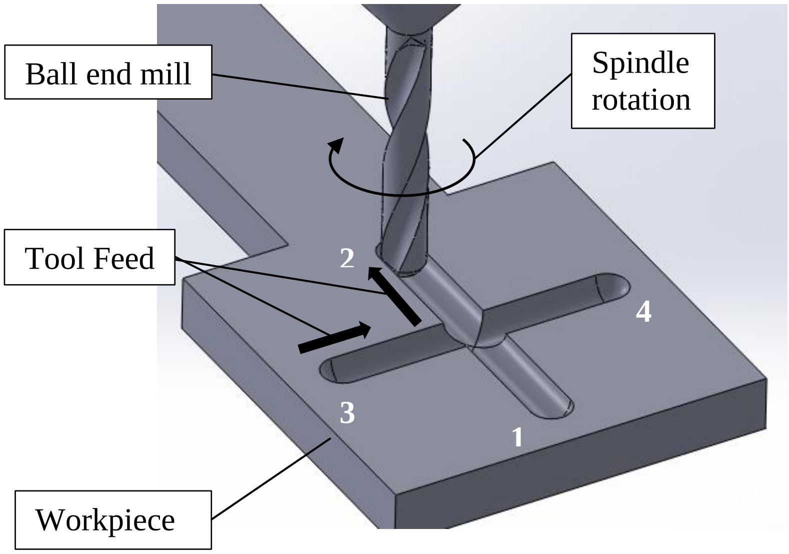

Figure 42. Schematic Representation of Micromilling Experiments. A Tool Starts at Position #1 and Moves to #2, Lifts up and Restarts at #3 and #4.

The various cutting conditions used in the micromilling experiments are shown in the Table 8. Cutting conditions used for mesomilling of 6061-T6 aluminum alloy and 36A low carbon steel are given in the Table 9. The recommended cutting speed and chip loads for mesomilling were selected from the machinery's book depending on the material of the workpiece and the cutting tool [46]. All milling experiments were performed with micromist coolant to provide better surface quality and longer tool life. The same cutting speed and various different chip loads were used for the same work piece material. The experiments with same cutting conditions were repeated for the uncoated and AlTiN coated tools.

Table 8. Cutting Conditions for Micromilling of NiTi Alloy, 316L and 304 Stainless Steels.

Workpiece material	Tool diameter, mm	Tool Coating	Depth of cut, µm	Spindle speed, rpm	Cutting speed, m/min	Chip load, µm/tooth	Machined length, mm
316L and 304 stainless steels	0.152	Uncoated	30	50000	24	0.05	12
	0.152	Uncoated	30	50000	24	0.1	12
	0.152	Uncoated	30	50000	24	0.2	12
	0.152	Uncoated	30	50000	24	0.3	12
	0.198	AlTiN	30	38377	24	0.05	12
	0.198	AlTiN	30	38377	24	0.1	12
	0.198	AlTiN	30	38377	24	0.2	12
	0.198	AlTiN	30	38377	24	0.3	12
NiTi alloy	0.198	AlTiN	30	38377	24	0.05	8
	0.198	AlTiN	30	38377	24	0.1	8
	0.198	AlTiN	30	38377	24	0.2	8
	0.198	AlTiN	30	38377	24	0.3	8

Table 9. Cutting Conditions for Mesomilling of 6061-T6 Aluminum Alloy and A36 Low Carbon Steel.

Material of the workpiece	Tool diameter, mm	Tool Coating	Depth of cut, µm	Spindle speed, rpm	Cutting speed, m/min	Chip load, µm/tooth	Machined length, mm
6061-T6 aluminum alloy	3.175	Uncoated/AlTiN	100	6020	60	5	10
	3.175	Uncoated/AlTiN	100	6020	60	10	10
	3.175	Uncoated/AlTiN	100	6020	60	20	10
	3.175	Uncoated/AlTiN	100	6020	60	30	10
	3.175	Uncoated/AlTiN	100	6020	60	50	10
	3.175	Uncoated/AlTiN	100	6020	60	80	10
	3.175	Uncoated/AlTiN	100	6020	60	100	10
A36 low carbon steel	3.175	Uncoated/AlTiN	50	3009	30	5	20
	3.175	Uncoated/AlTiN	50	3009	30	15	20
	3.175	Uncoated/AlTiN	50	3009	30	40	20
	3.175	Uncoated/AlTiN	50	3009	30	70	20

3.4.6 Surface Roughness Measurements

The optical microscope and scanning electron microscope (SEM) were utilized to observe the surface topography of the machined microchannels. In order to obtain the complete image with the full depth of field from the optical microscope, the digital image stitching was utilized. Prior to the observation with the microscope, machined channels were cleaned ultrasonically with Isopropyl alcohol for 3-5 minutes and dried with pressurized air in order to remove residue of oil and chips. The optical microscope images were imported into SolidWorks software and scaled for further dimensional analysis of the surface.

The surface finish along machined channels was measured with a Zygo white light interferometer, which provided three dimensional surface profiles. Before the start of the measurements, bipolar scanning depth (length) was set to 100 µm. The objective lens was moved up or down in order to focus the channel surface and find fringes on the bottom surface of the channel. The tilting knobs were used to align the channel bottom surface horizontally, since even small deviation from horizontal line would lead to the incorrect measurements. The light intensity was adjusted in order to obtain complete scanning image without black spots.

Two different types of measurements were performed: (1) along the center line of the channel; and (2) at the side wall of the channel, 60-70 µm away from the center line. R_a type of surface roughness was measured along the line 0.9 mm (Figure 43 (a)). The measurements were repeated in the different locations of the same channel 10 times and the average value of surface roughness was calculated. In order to determine effects of tool wear and build-up edge on surface finish, it was measured at the beginning of the first channel and at the end of the last channel, machined with the same cutting tool and cutting conditions. The distribution of surface height was provided on three different plots – filled plot (Figure 43 (a)), oblique plot (Figure 43 (b)), and profile plot (Figure 43 (c)).

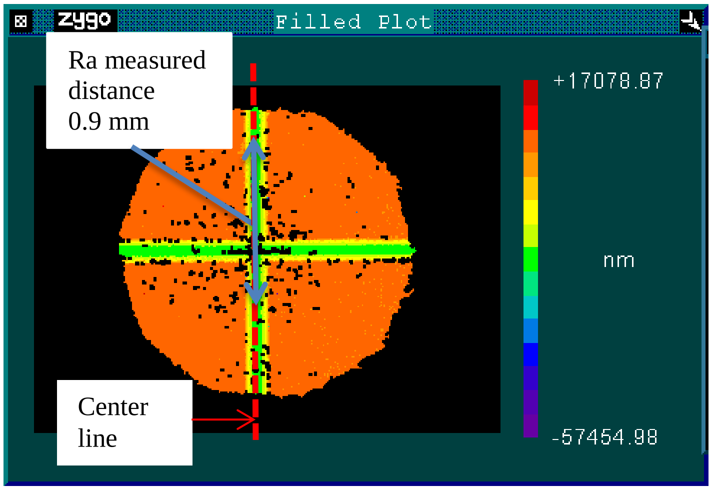

(a)

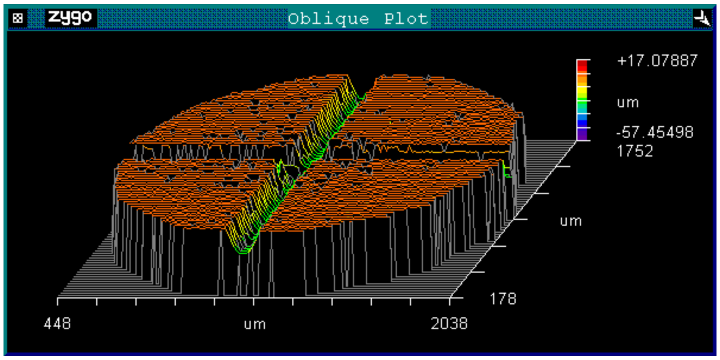

(b)

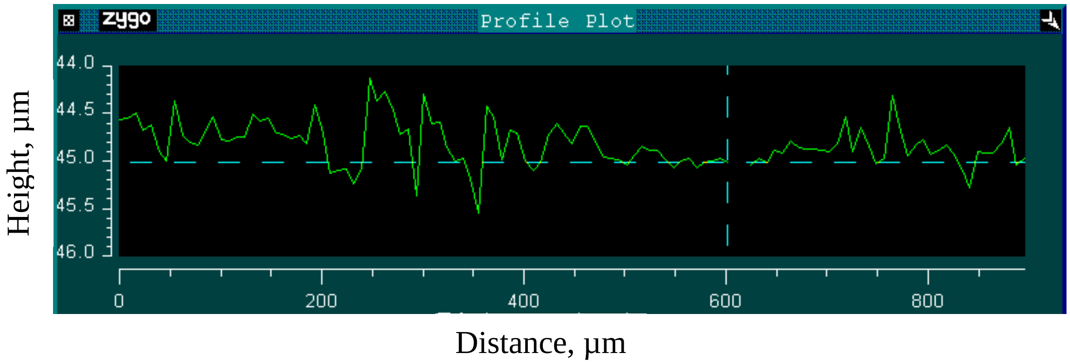

(c)

Figure 43. Surface Roughness (R$_a$) Measurements using Zygo White Light Interferometer: (a) Filled Plot; (b) Oblique Plot; (c) Profile Plot. 304 Stainless Steel, Coated ϕ0.198 mm Ball End Mill, 24m/min, 0.05 μm/tooth, Average R$_a$=0.18μm.

3.4.7 Tool Wear and Build-Up Edge

The tool wear and build-up edge (BUE) on the tools were observed using optical and scanning electron (SEM) microscopes. For better observation of the tool wear with SEM microscope the build-up edge was removed by chemical etching of the tools. The Figure 44 (a) shows SEM picture of the tool that was etched for 9 minutes and Figure 44 (b) shows the tool with BUE that was not etched. Specific chemical solutions were utilized for chemical etching of the tools after machining of different materials. The compositions of chemical solutions used for chemical etching of the tools after machining of 304 stainless steel and CP titanium are shown in the Table 10 [6]. The tools were etched by swabbing them with cotton swabs saturated in chemical solutions for 9 minutes.

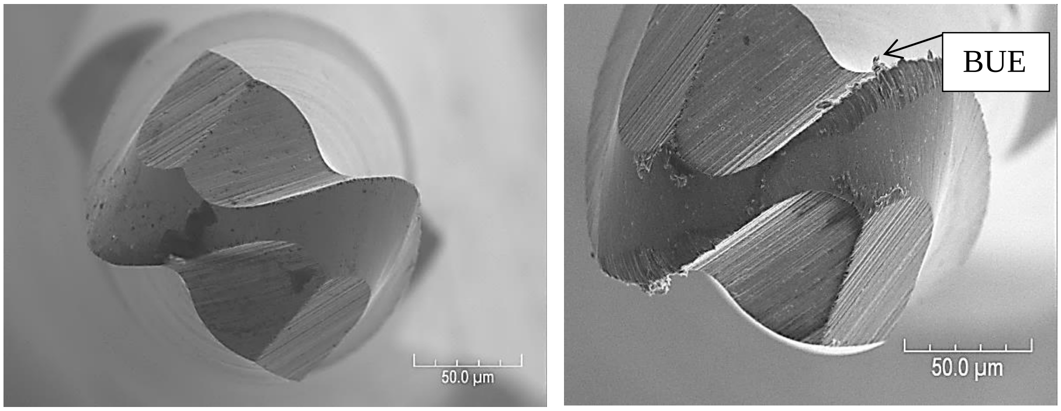

Figure 44. SEM Images of the Micro Ball End Mills Ø152µm: (a) after Etching for 9 min. 24 m/min, 0.1µm/tooth, MQL, after 966 mm of CP Titanium; (b) without Etching. 24m/min, 0.2µm/tooth, MQL, after 12 mm of 304 Stainless Steel and 12 mm of 316L Stainless Steel.

Table 10. Solutions for Chemical Etching of 304 Stainless Steel and CP Titanium.

Material	Chemical	Fraction [%]	Etching time [min]
CP titanium	Hydrofluoric acid	4	9
	Nitric acid	20	
	Distilled water	76	
304 stainless steel	Hydrochloric acid	50	9
	Glycerol	33	
	Nitric acid	17	

3.4.8 Micromilling of High Aspect Ratio Channels

Four channels with different aspect ratios were machined on 304 stainless steel and 316L stainless, and six channels with different aspect ratios were machined on NiTi alloy (Table 11). The length of all channels was set to 3.5mm. New AlTiN coated tool of diameter Ø198μm was used to machine each material. The same cutting conditions were used to machine all channels. The cutting conditions are provided in the Table 11. CNC programs for all experiments are provided in APPENDIX C.

In order to examine the profiles and the quality of milled microchannels, the samples were sectioned in the direction perpendicular to the channels using wire type EDM. Prior to the observation and measurements with optical microscope, the cut surface was ground and polished in order to enhance the surface quality and remove burrs left after electrical discharge machining.

Table 11. Cutting Conditions for Micromilling of High Aspect Ratio Channels.

Channel #	Workpiece material	Depth of cut, µm	Cutting Speed, m/min	Chip load, µm/flute	Total channel depth, µm	Aspect ratio
1	304 SS 316L SS NiTi	30	24	0.1	60	0.3:1
2					120	0.6:1
3					180	0.9:1
4					210	1.1:1
5	NiTi				300	1.5:1
6					420	2.1:1

Prior to the grinding, the metal samples were placed in the rubber mold facing down with the surface where it was sectioned, and epoxy mixture was poured into the mold and left to solidify for 24 hours. Then, the bottom and top surfaces of the solidified epoxy were ground on the Handiment grinding machine to make them parallel to each other. Parallelism of the surfaces was required to provide accurate measurements with optical microscope. The abrasive papers with 320, 400, and 600 grits were used consecutively to grind the sample. Before starting the grinding with the new abrasive paper, the sample was thoroughly washed with water in order to flush away any particles that might have remained on the ground surface from the previously used abrasive paper. Buehler polishing machine was used to polish the microscrateches left after the grinding. First the sample was polished with the polishing solution with particle size of 1µm, and then with polishing solution with particle size of 0.3µm. The polishing solutions were made by mixing deagglomerated alumina with distilled water. After the polishing the sample was cleaned ultrasonically with isopropyl alcohol for 3-5 minutes and dried with pressurized air.

4. RESULTS AND DISCUSSIONS

4.1 Tool Vibration and Runout Analysis

Fast Fourier transform (FFT) data was generated from measured laser displacement data. It provided detailed frequency spectra and showed the dynamics of a milling system (Figures 45-47). Two primary peaks on each FFT plot corresponded to the spindle speed frequency (f_{sp}) of 466.3 Hz and the tooth passing frequency (f_{tooth}) of 932.6 Hz. Spindle speed frequency was calculated as following:

$$f_{sp} = \frac{N}{60} = \frac{27500\, rev/min}{60\, sec/min} = 458.3\, Hz \cong 466.3\, Hz \tag{4.1}$$

Tooth passing frequency was calculated as following:

$$f_{tooth} = n_t\, f_{sp} = 2 \times 458.3\, Hz = 916.6\, Hz \ \cong 932.6\, Hz \tag{4.2}$$

where

f_{sp} : spindle speed frequency (Hz)

f_{tooth} : tooth passing frequency (Hz)

N : spindle speed (rev/min)

n_t : number of teeth

Other peaks that appear on the plots could be due to harmonic vibration, or laser and MQL system noises, or result of the utilization of the data acquisition card at low sampling rate. In the Figure 45 the spindle speed peak for the rotating spindle without machining corresponded to the runout of the spindle and tool combination. The amplitude of the spindle speed peak increased by 90% while milling at 0.038 mm depth of cut (half of tool radius) compared to its amplitude for rotating of the spindle without machining (Figures 45 and 46). The amplitude of the spindle speed peak increased more significantly by 240%, when depth of cut was equal to the tool radius of 0.076 mm (Figure 47). The tooth passing peak amplitude dominated others in free rotation without milling, but reduced when a tool was engaged during machining. Tool deflection, due to cyclic milling, and forces in an interrupted milling operation, therefore, are the primary concerns for this machining system. Depths of cut lower than half of the tool radii were subsequently utilized for all machining experiments.

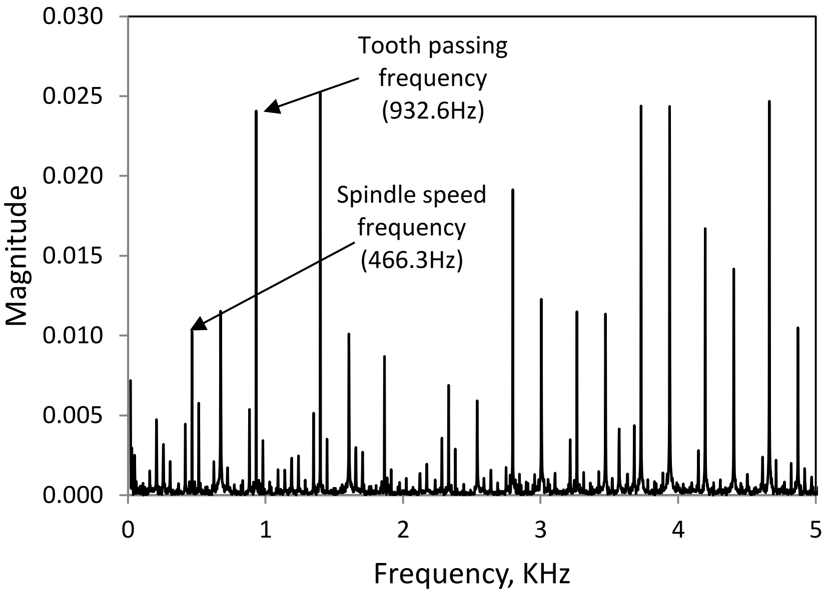

Figure 45. Frequency Spectrum of Tool and Spindle Runout. Rotating Spindle without Machining, Ball End Mill ϕ0.152 mm, Spindle Speed 27238 rpm.

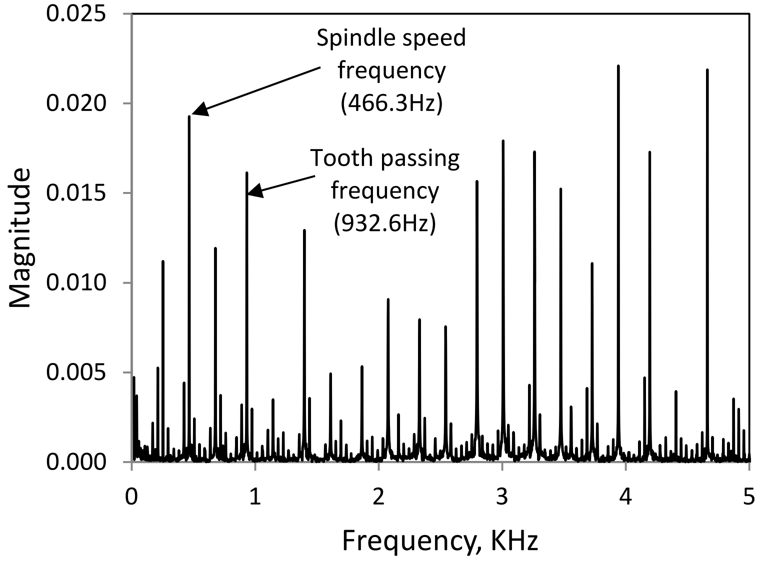

Figure 46. Frequency Spectrum of Tool and Spindle Runout. Milling CP Titanium, Ball End Mill ϕ0.152 mm, Spindle Speed 27238 rpm, Feed Rate 2.7 mm/min, Depth of Cut 38 µm, MQL.

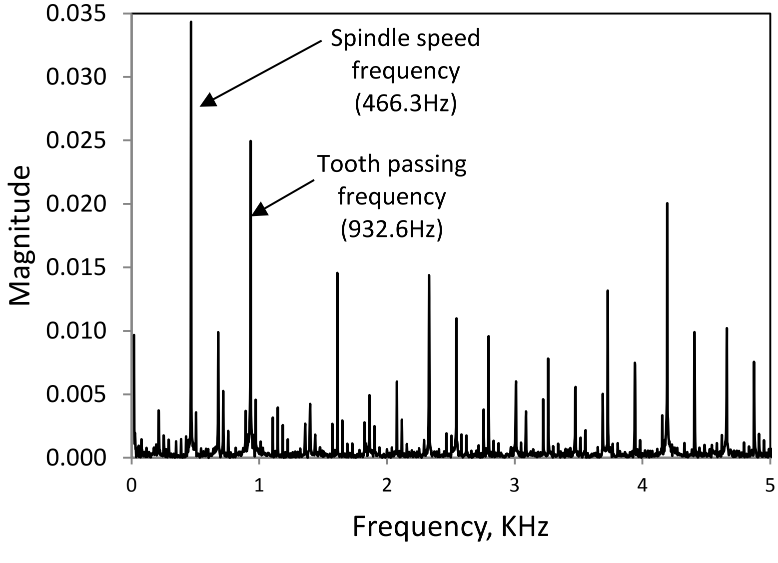

Figure 47. Frequency Spectrum of Tool and Spindle Runout. Milling CP Titanium, Ball End Mill ϕ0.152 mm, Spindle Speed 27238 rpm, Feed Rate 2.7 mm/min, Depth of Cut 76 µm, MQL.

4.2 Theoretical Surface Roughness Modeling

In this section theoretical surface roughness in ball end milling was derived using geometrical approach. The theoretical surface finish model was compared and validated with the experimental surface finish data. While deriving this model the following assumptions were made:

I. The depth of cut and chip load are larger than the cutting edge radius of the tool, therefore, plowing of the tool cutting edges on the machined surface does not occur and does not affect surface roughness.

II. The cutting edge of the tool is sharp.

III. The build-up-edge is not present on the tool, thus, surface roughness is not affected by cutting speed.

Figure 48 shows surface profile of the channel bottom formed after ball end milling at extremely low depth (OB_1), which corresponds to the particular perpendicular tool section of radius R_1. Tool makes contact with the workpiece and starts cutting at point 1, then it moves the distance of 6 chip load distances to point 2. The distance between two peaks formed on the machined surface *(CB)* is equal to two chip loads ($2f_t$), as it was determined with simulation of surface formation in ball end milling in SolidWorks and confirmed experimentally (APPENDIX F and G). The circular segment *CAB* of radius *R* describes surface profile of the channel bottom and is a base contour for surface roughness calculation (Figure 48 (b)).

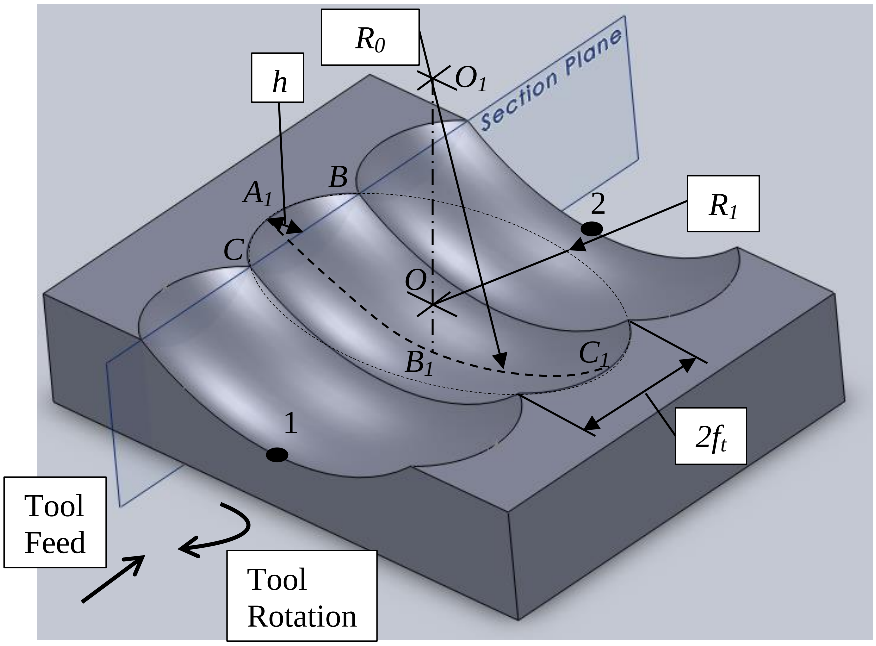

(a)

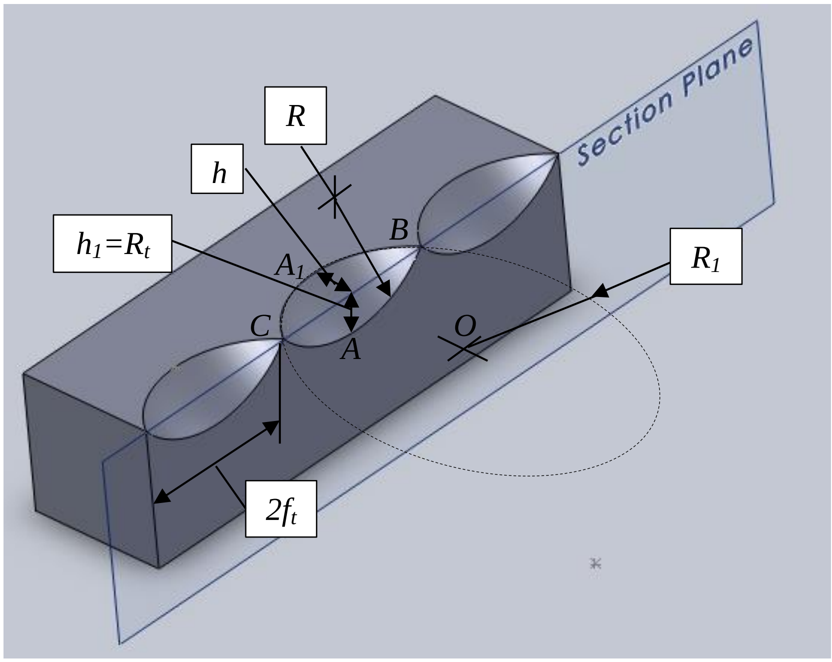

(b)

Figure 48. Surface Profile of the Channel Formed after Ball End Milling at Particular Depth OB_1: (a) 3D View; (b) Section View.

Define variables used in the derivation of the theoretical model:

h : height of the peak in radial direction (mm)

f_t : chip load (mm/tooth)

R_1 : radius of the radial section of the tool at the particular depth OB_1 (mm)

h_1 : height of the peak in axial direction (mm)

x,y : coordinates of the circle of radius R_0 (mm)

R_0 : tool radius (mm)

R : radius of the circular segment *CAB* (mm)

x_G, y_G : coordinates of center of gravity of the area *ABD* (mm)

R_a : arithmetic average surface roughness (mm)

The radius R can be calculated using other parameters shown in the Figure 48 according to the following steps:

a) The height of the peak in radial direction h is calculated as following:

$$h = R_1 - \sqrt{R_1^2 - f_t^2} \tag{4.3}$$

b) Figure 49 shows perpendicular section of the channel $(A_1B_1C_1)$ with respect to Cartesian coordinate system. The height of the peak in axial direction h_1 is calculated using equation of the circle:

$$x^2 + y^2 = R_0^2 \tag{4.4}$$

c) According to the coordinate system shown in the Figure 49, the coordinates of the point $A(x,y)$ are:

$$x = R_1 - h \tag{4.5}$$

$$y = \sqrt{R_0^2 - R_1^2} + h_1 \tag{4.6}$$

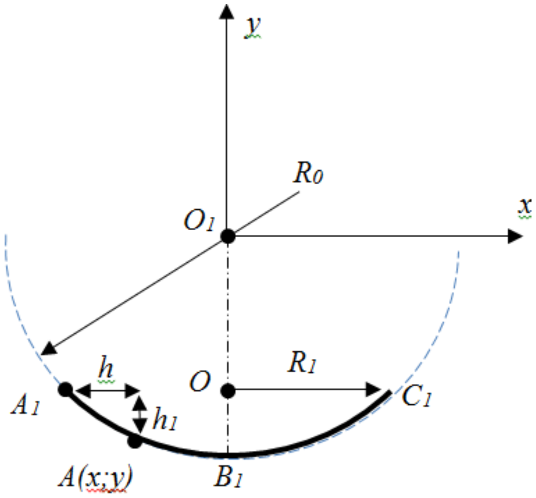

Figure 49. Perpendicular Section of the Channel *($A_1B_1C_1$)*.

d) When equations (4.5) and (4.6) are substituted into equation (4.4), the height of the peak in axial direction h_1 (or peak-to-valley surface roughness R_t) is calculated as following:

$$h_1 = R_t = \sqrt{R_0^2 - (R_1 - h)^2} - \sqrt{R_0^2 - R_1^2} \tag{4.7}$$

e) The radius R of the circular segment *CAB* (Figure 48 (b)), that describes surface profile at channel bottom, is calculated using properties of the chord and the sagitta of the circle as following:

$$R = \frac{(2f_t)^2}{8h_1} + \frac{h_1}{2} \tag{4.8}$$

$$R = \frac{f_t^2}{2h_1} + \frac{h_1}{2} \tag{4.9}$$

Figure 50 shows surface profile formed by ball end mill at the channel bottom along the distance equal to six chip loads ($6f_t$). Contour *CAB* is a machined surface. The point G is a center of gravity of the area of machined surface *ABD*. The line L goes through center of gravity G and is a base line for R_a surface roughness calculation.

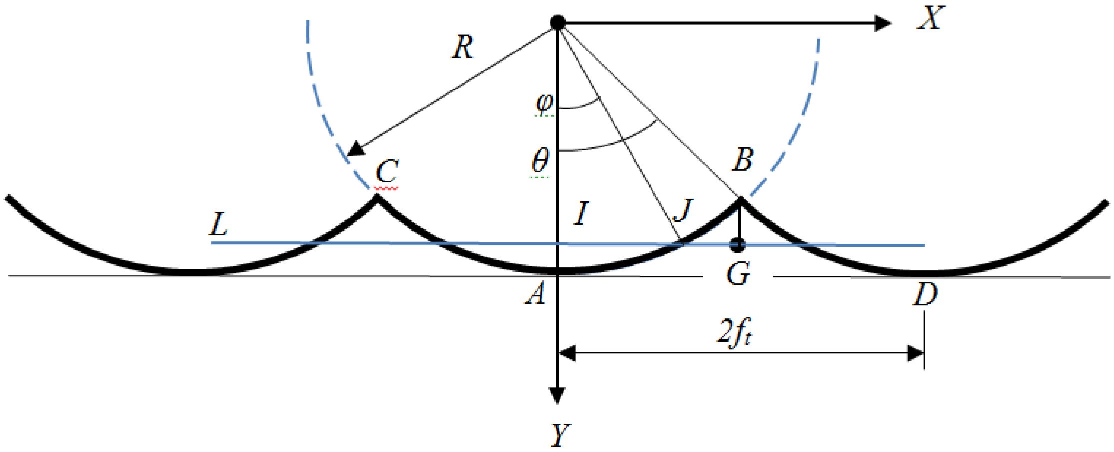

Figure 50. Surface Profile Formed by Ball End Mill at the Channel Bottom.

Theoretical R_a surface finish was derived according to the following steps:

1) Two additional variables θ and φ are defined in order to simplify derivation (Figure 50):

$$\theta = arcsin\left(\frac{f_t}{R}\right) \tag{4.10}$$

$$\varphi = arcsin\left(\frac{(R^2 - y_G^2)^{0.5}}{R}\right) \tag{4.11}$$

2) According to the coordinate system shown in the Figure 50, the coordinate of center of gravity x_G at point *G* is:

$$x_G = f_t \tag{4.12}$$

3) Area *ABD* can be divided into horizontal strips with extremely small width. The coordinate of center of gravity y_G at point *G* is estimated from equation:

$$Ay_G = \int y\,dA = \int_{y_B}^{y_A} y[2f_t - 2(R^2 - y^2)^{0.5}]dy = \frac{1}{3}f_t^3 \tag{4.13}$$

4) Area *ABD* can be calculate as following:

$$A = 2\int_0^{ft}[R - (R^2 - x^2)^{0.5}]dx = 2Rf_t - R^2\left(\theta + \frac{1}{2}\sin 2\theta\right) \tag{4.14}$$

5) When equations (4.14) is substituted into equation (4.13), the coordinate of center of gravity y_G is than calculated as following:

$$y_G = \frac{f_t^3}{3R}\frac{1}{2f_t - R\left(\theta + \frac{1}{2}\sin 2\theta\right)} \tag{4.15}$$

6) The absolute values of /y_i-y_G/ are used to calculate arithmetic average surface roughness as following:

$$R_a = \sum_i^n \frac{|y_i - y_G|}{n} = \sum_i^n \frac{|y_i - y_G|dx}{ndx} = \frac{2(area\ AIJ + area\ JGB)}{2f_t} \tag{4.16}$$

$$R_a = \frac{1}{f_t}\left\{\int_0^{x_j}[(R^2 - x^2)^{0.5} - y_G]dx + \int_{x_j}^{ft}[y_G - (R^2 - x^2)^{0.5}]dx\right\} \tag{4.17}$$

$$R_a = \frac{R^2}{f_t}\left(\varphi - \frac{1}{2}\theta + \frac{1}{2}\sin 2\varphi - \frac{1}{4}\sin 2\theta\right) + y_G - \frac{2y_G}{f_t}(R^2 - y_G^2)^{0.5} \qquad (4.18)$$

Figure 51 shows theoretical surface roughness prediction given by equation (4.18), theoretical model from the literature [37], and experimental surface roughness data obtained after milling of aluminum alloy 6061-T5 with WC-Co ball end mill with two flutes of diameter Ø9.525mm. The theoretical surface roughness model agrees with the model form the other study given by following equation [37]:

$$R_a = 0.2568\frac{{f_t}^2}{D} \qquad (4.19)$$

The theoretical model predicts surface finish quiet well when chip load is larger than 50µm. However, when chip load is lower than 50µm the experimental surface roughness values are much higher than predicted by theory and are similar (0.27-0.31µm R_a) for different chip loads (5µm/tooth-25µm/tooth). The contribution of the chip load is not truly reflected at low chip loads, because when the chip thickness becomes lower than tool edge radius, which was approximately 20-25 µm, more elastic deformations occur at machined surface and the surface finish worsens. This agrees with another study that found that when uncut chip thickness (chip load) is lower than cutting edge radius are used, the plowing of the cutting edge on the surface occurs and material is not removed by shearing mechanism and is deformed elastically, which leads to bad surface finish and faster tool wear [1].

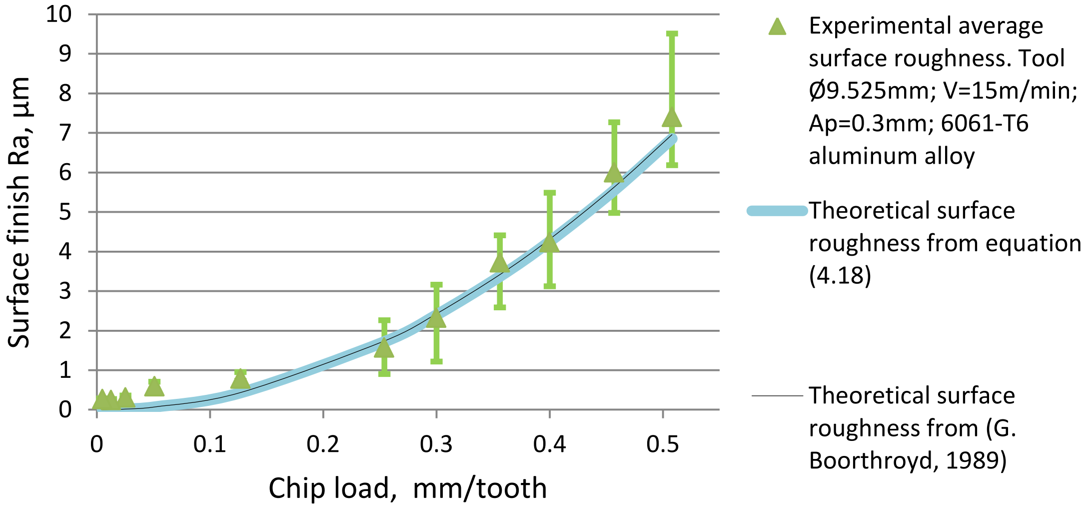

(a)

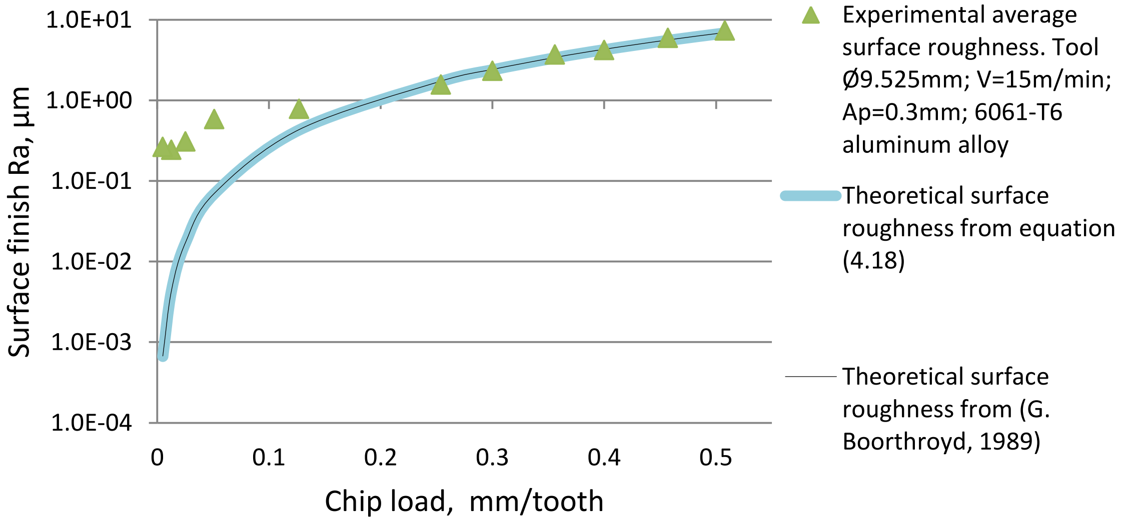

(b)

Figure 51. Validation and Comparison of Theoretical R_a Model with Experimental Data: (a) Plot with Standard Linear Scale; (b) Plot with log Scale.

As we can see from discussion above, the theoretical surface roughness after macro ball end milling can be predicted using geometrical approach. However, these mathematical models have not yet been validated for micro ball end milling, and it is not clear whether they are suitable for micromachining operations. Also, other studies need to be conducted in order to include other parameters that affect surface roughness, such as build up edge (BUE), utilization of coated tools, and utilization of rough and finishing passes.

4.3 Surface Roughness

Surface roughness was measured along the center line at the bottom of each machined microchannel. The average value of surface roughness R_a was calculated form 10 values measured at the center line of the same channel. The average surface finish was in range 0.1-1.5μm R_a for all machined materials (304 stainless steel, 316L stainless steel, and NiTi alloy) as expected for poly-grain cutting tools and polycrystalline materials. Surface roughness was increasing with chip load for all micromilling experiments (Figure 52-54) as it does during macromilling, but it contradicts with another study that found feedrate, and therefore chip load, does not affect surface finish [26]. It is postulated that a wrong combination of large tool edge radius and shallow depth of cut could smear the surface and does not truly reflect the contribution of chip load. Surface finish data along a channel axis is tabulated in the APPENDIX D.1.

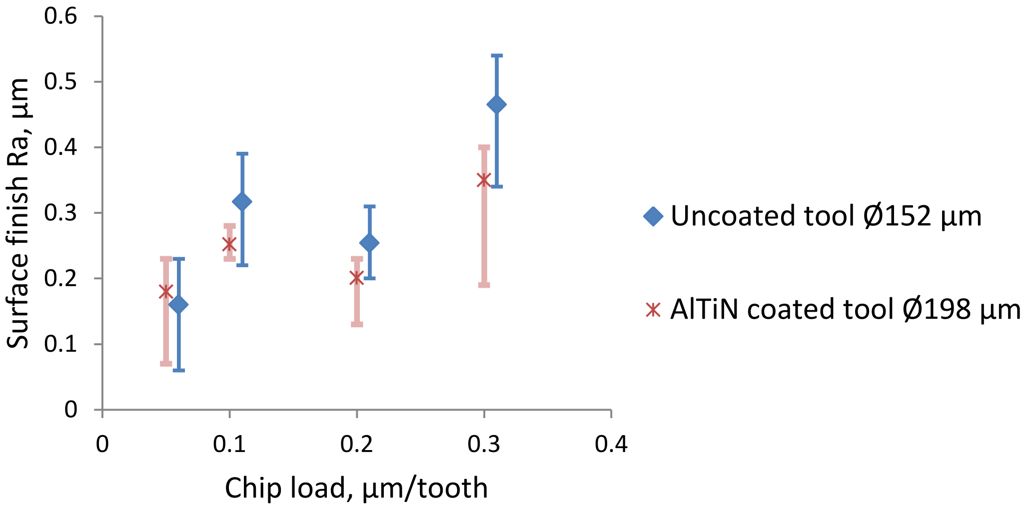

Figure 52. Average and Range of Surface Finish due to Chip Load Variation. V=24m/min, Ad=0.03mm, MQL, after Machining 12 mm on 304 Stainless Steel.

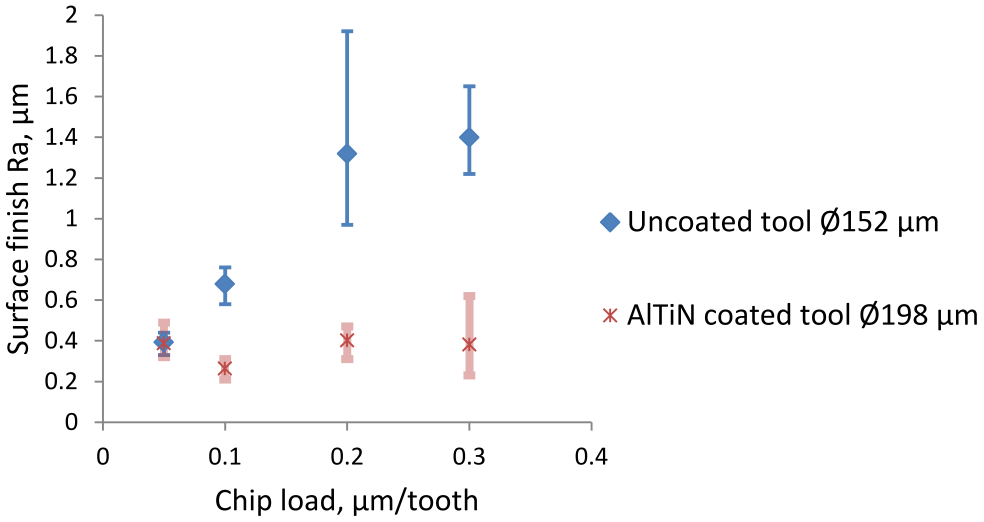

Figure 53. Average and Range of Surface Finish due to Chip Load Variation. V=24m/min, Ad=0.03mm, MQL, after Machining 12mm on 304 and 12mm on 316L Stainless Steels.

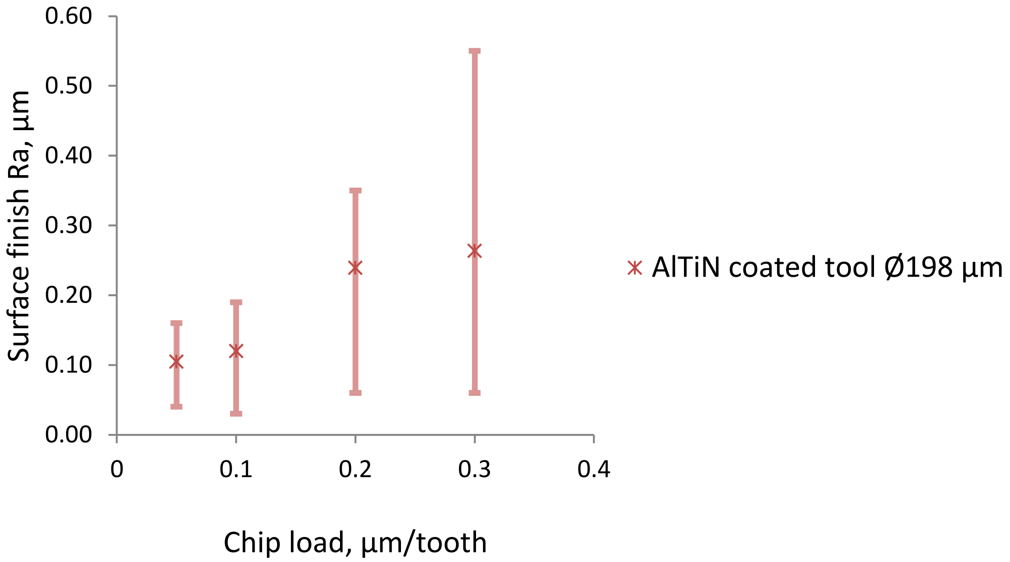

Figure 54. Average and Range of Surface Finish due to Chip Load Variation. V=24m/min, Ad=0.03mm, MQL, after Machining 12mm on 304, 12mm on 316L Stainless Steels, and 8 mm on NiTi Alloy.

It is depicted in Figures 52 and 53 that microchannels machined in stainless steel with coated tools had lower R_a values compared to those machined with uncoated tools for the same chip loads. Uncoated microtools performed like coated when new, but they were quickly deteriorated due to tool wear and the forming of the build-up edge (Figures 55 and 56). The maximum abrasive wear was observed on the cutting edges of the uncoated tools at the largest diameter (effective tool diameter), since the cutting speed was largest at that diameter. Figure 57 shows SEM images of coated ball end mill after machining of 24 mm of stainless steel and 8 mm of NiTi alloy. Although no abrasive tool wear and significant build-up edge are seen, its coating layer is chipped off along the cutting edges.

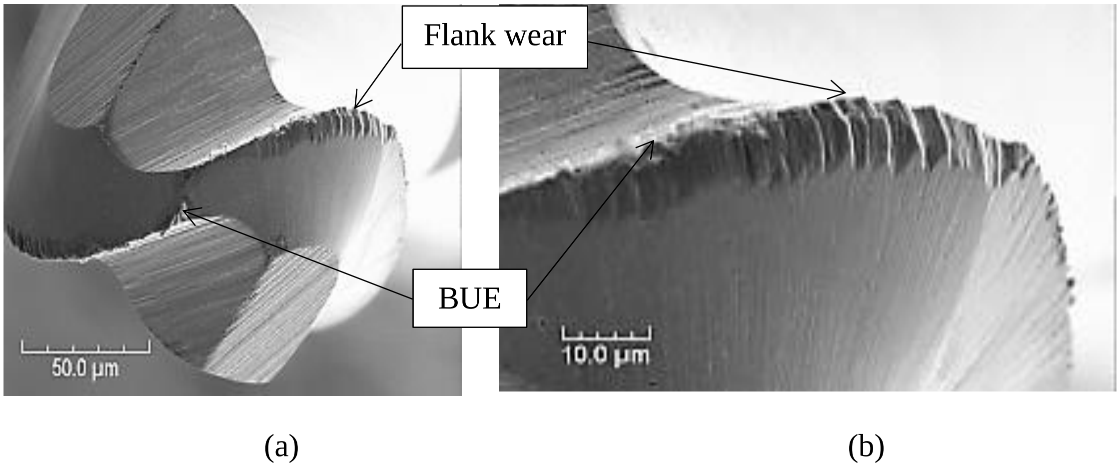

Figure 55. SEM Image of Uncoated Ø152µm Ball End Mill, V=24m/min, ft=0.1µm/tooth, MQL, after Machining 12 mm on 304 Stainless Steel and 12 mm on 316L Stainless Steel: (a) Cutting End of the Mill; (b) Cutting Edge.

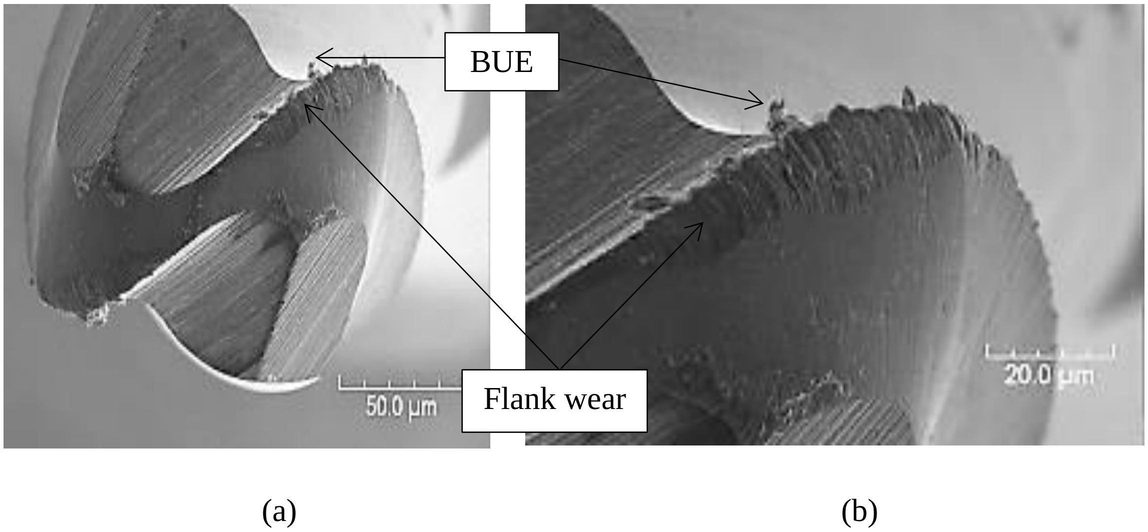

Figure 56. SEM Image of Uncoated Ø152µm Ball End Mill, V=24m/min, ft=0.2µm/tooth, MQL, after Machining 12 mm on 304 Stainless Steel and 12 mm on 316L Stainless Steel: (a) Cutting End of the Mill; (b) Cutting Edge.

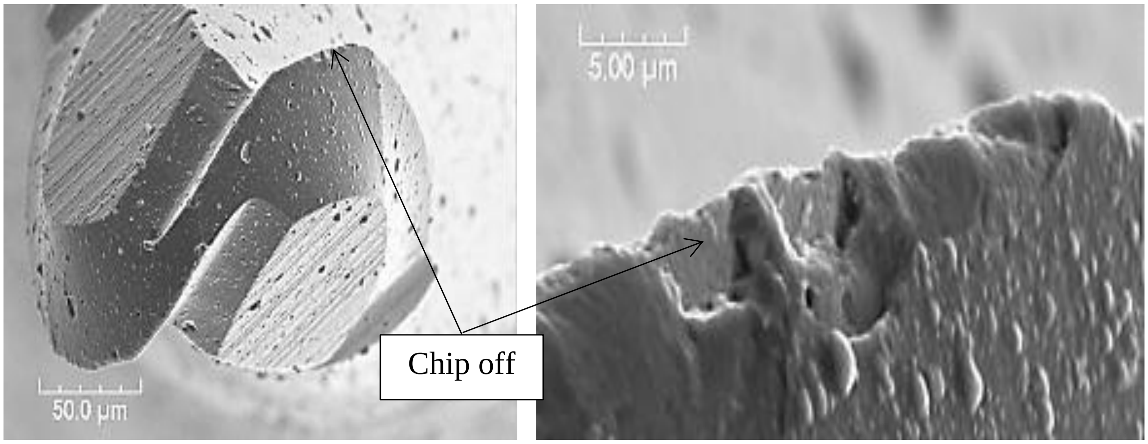

(a) (b)

Figure 57. SEM Image of Coated Ø198µm Ball End Mill, V=24m/min, ft=0.1µm/tooth, MQL, after Machining 12mm on 304 Stainless Steel, 12 mm on 316L Stainless Steel, and 8 mm on NiTi Alloy: (a) Cutting End of the Mill; (b) Cutting Edge.

The BUE on the uncoated tools increased effective cutting edge radius, generated more burrs, work-hardened the machined subsurface, and worsened the surface finish. On the contrary, a better surface finish resulted from machining with coated tool since BUE was absent when micromilling 304, 316L stainless steels, NiTi alloy (Figure 58). This is in agreement with another experimental study that found micromilling Ti6Al4V in dry condition promotes BUE and worsens surface finish [2].

The milling direction also affected the surface integrity of a microchannel. Referring to Figure 42, a cutter was programmed to mill a channel from points 1-2 then 3-4. The combination of tool rotation direction and tool feed direction provided down milling on the right side of the moving tool and up milling on its left side. Down milling generated fewer burrs and resulted in better surface finish as compared to up milling as seen in Figure 58, which is in agreement with another study that investigated that down milling is recommended when low surface roughness is desired [18]. The excessive and non-uniform burrs pose a challenging task to remove them after micromilling.

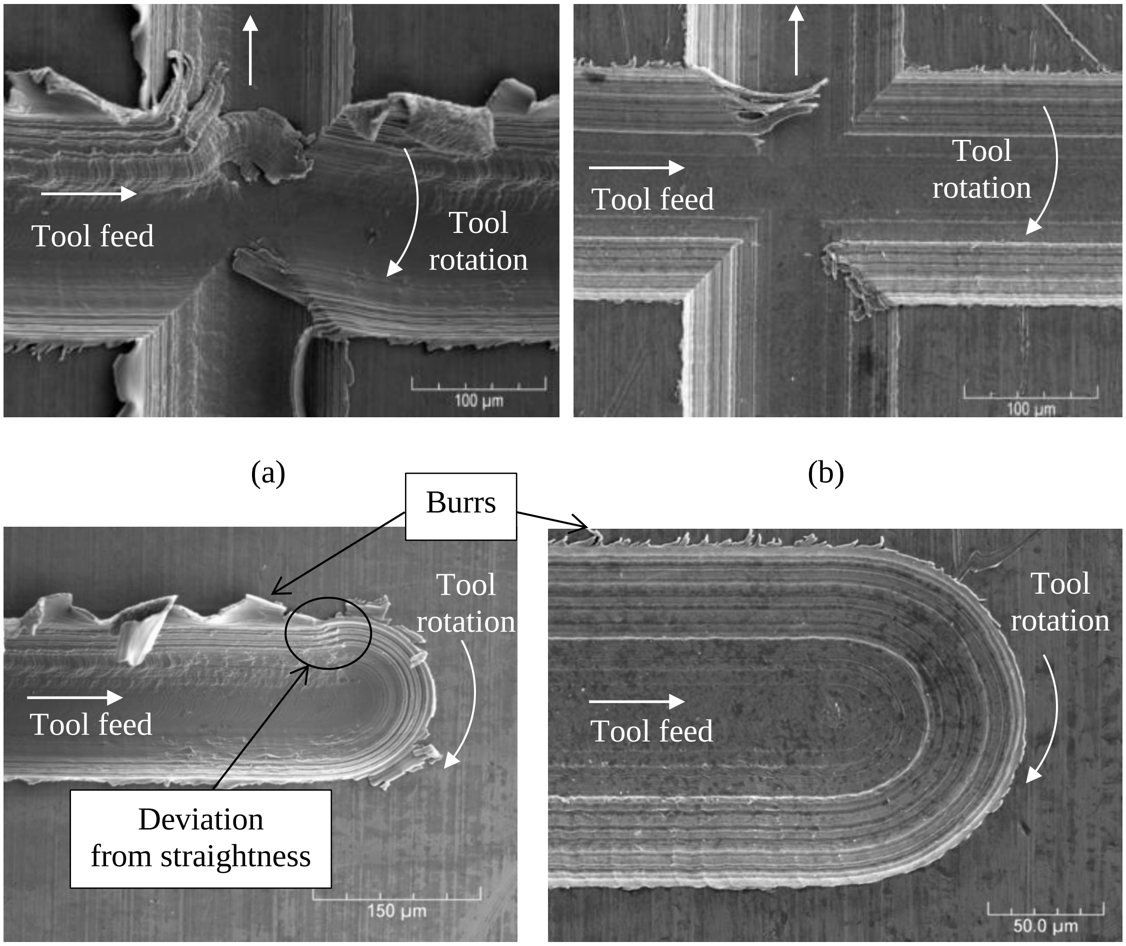

(a) (b)

(c) (d)

Figure 58. SEM Images of Milled Microchannels in 304 Stainless Steel, V=24m/min, ft=0.1µm/tooth, MQL: (a) Center of Channels, Uncoated Tool Ø152µm; (b) End of Channel, Uncoated tool Ø152µm; (c) Center of Channels, Coated Tool Ø198µm; (d) End of Channels, Coated Tool Ø198µm.

After milling with both coated and uncoated tools, the scratching parallel lines formed away from the center of the channel on the side walls (Figure 58) due to missing WC grains on the tool cutting edges. These defects, found on the cutting edges of the new coated and uncoated microtools, are shown in the Figure 59.

The geometric accuracy of the microchannels machined with uncoated tools was lower than for those machined with coated tools. Figure 58 (c) shows that the microchannel milled with uncoated tool was not straight at its end. However, the channel machined with coated tool was straight along its full length (Figures 58 (b) and (d)). The progressive wear and the formation of the build-up edge on the uncoated tool resulted in the more excessive cutting force at the one cutting edge than at another, which led to the bending and deflection of the tool during machining. When the tool was moving up in Z direction at the end of the slot, the magnitude of the cutting force decreased and elastic deformation of the tool was recovered, which led to the deviation from straightness of the slot at its end.

Figure 60 shows that surface finish also depended on the machined length. Because tool wear progressed and BUE formed on the tools, the surface roughness was increasing with machined length while micromilling 304 stainless steel with uncoated tools with the same chip load (0.3μm/tooth). On the other hand, surface finish did not change significantly with machined distance while micromilling with coated tools, since tools had no BUE and wear that could worsen the surface finish.

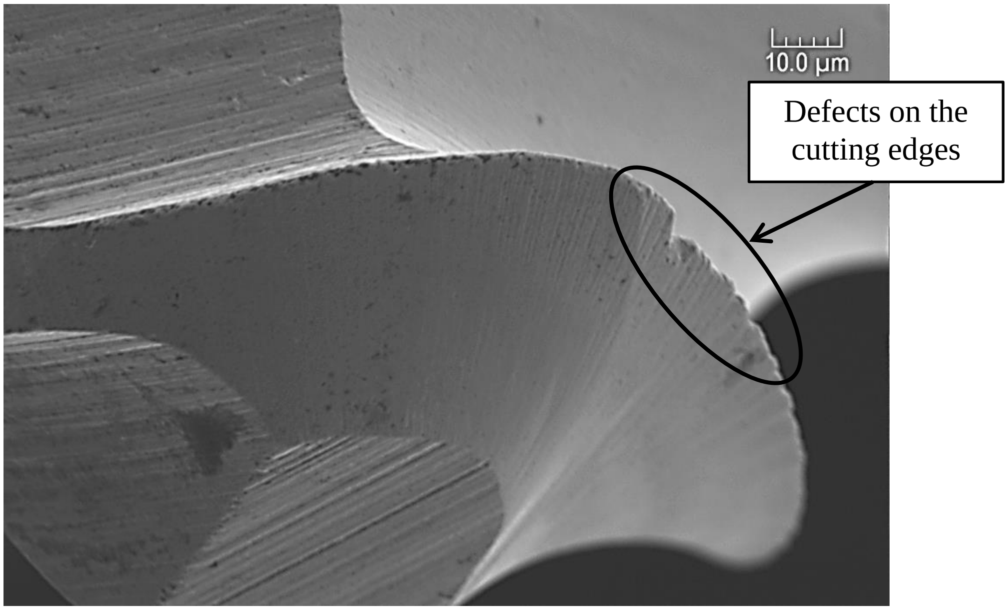

Figure 59. Defects on the Cutting Edges of Uncoated Tool Ø152µm.

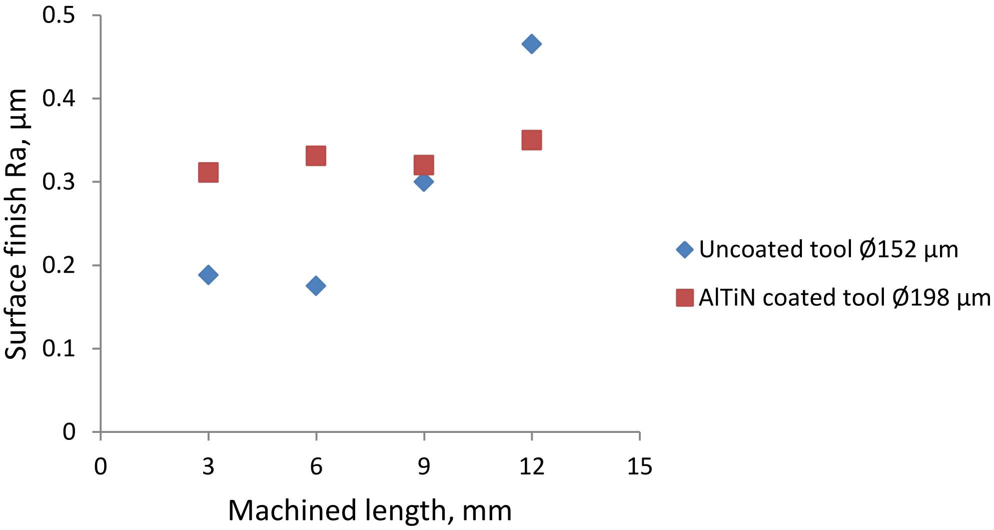

Figure 60. Effect of Machined Length on Surface Finish of Milled Microchannels, f_t=0.3µm/tooth, V=24m/min, Ad=0.03mm, 304 Stainless Steel, MQL.

Surface finish values measured along the center line of milled mesochannels were higher than those measuring 60-70µm away from it for both machined materials 6061-T6 aluminum alloy and A36 low carbon steel (Figure 61 and 62). The cutting speed at the tip of the ball end mill was zero, which could lead to the faster center wear of the tool tip. When center wear progressed, the new flat cutting edges were created in the tool geometry, which resulted in the generation of the rougher surface finish at the center of the channel.

The surface roughness was increasing with chip load as it did for micromilling experiments. Its average values were similar in the channels machined with both coated and uncoated tools, since there were no effects of tool wear and BUE on the surface formation. Both coated and uncoated tools had no wear and BUE after machining 10mm of 6061-T6 aluminum alloy and 20mm of 36A low carbon steel (Figure 63). Figure 64 shows how the surface finish at the channel center was worsening with increase of chip load while mesomilling of 6061-T6 aluminum alloy. The distance between marks at the channel center was equal to two chip load distances. Milling direction also affected the surface finish on the side walls of the channel. Referring to Figure 64, the combination of tool rotation direction and tool feed direction provided down milling on the right of moving tool and up milling on its left. Down milling resulted in better surface finish on the right side wall as compared to up milling on the left. Surface finish data along a channel axis and at the side wall is tabulated in the APPENDIX D.2.

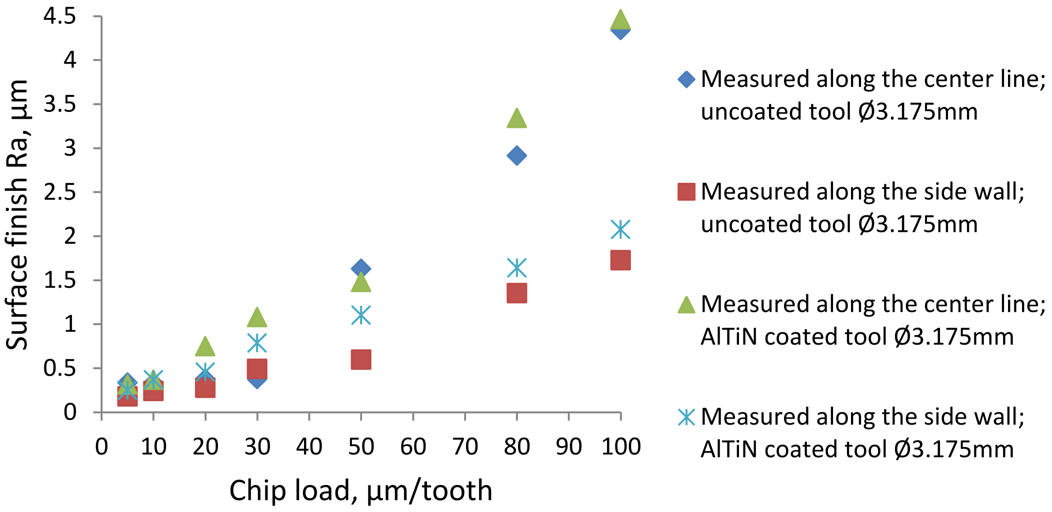

Figure 61. Effect of Chip Load and Measuring Location on Surface Finish of Milled Mesochannels. V=60m/min, Ad=0.1mm, MQL, after Machining 10mm on 6061-T6 Aluminum Alloy.

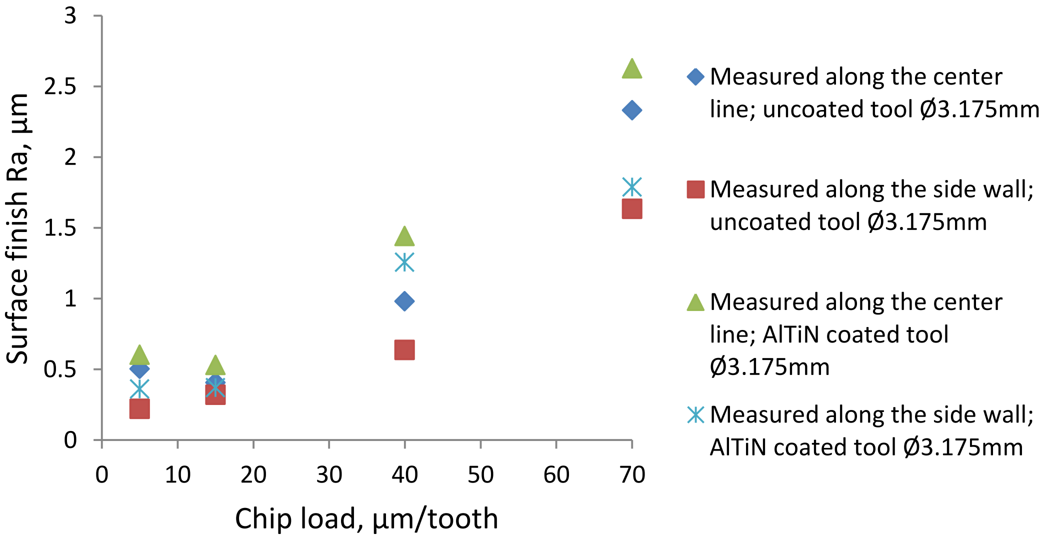

Figure 62. Effect of Chip Load and Measuring Location on Surface Finish of Milled Mesochannels. V=30m/min, Ad=0.05mm, MQL, after Machining 10mm on A36 Low Carbon Steel.

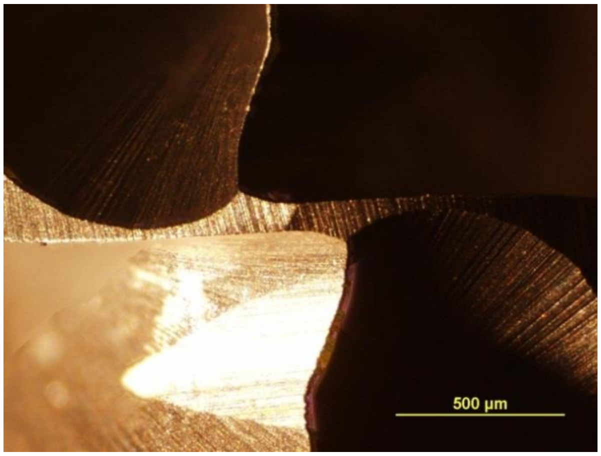

Figure 63. Absence of BUE and Tool Wear on the Cutting Edges of the Uncoated Ball End Mill Ø3.175mm, MQL, after Machining 10mm on 6061-T6 Aluminum Alloy and 20mm on 36A Low Carbon Steel.

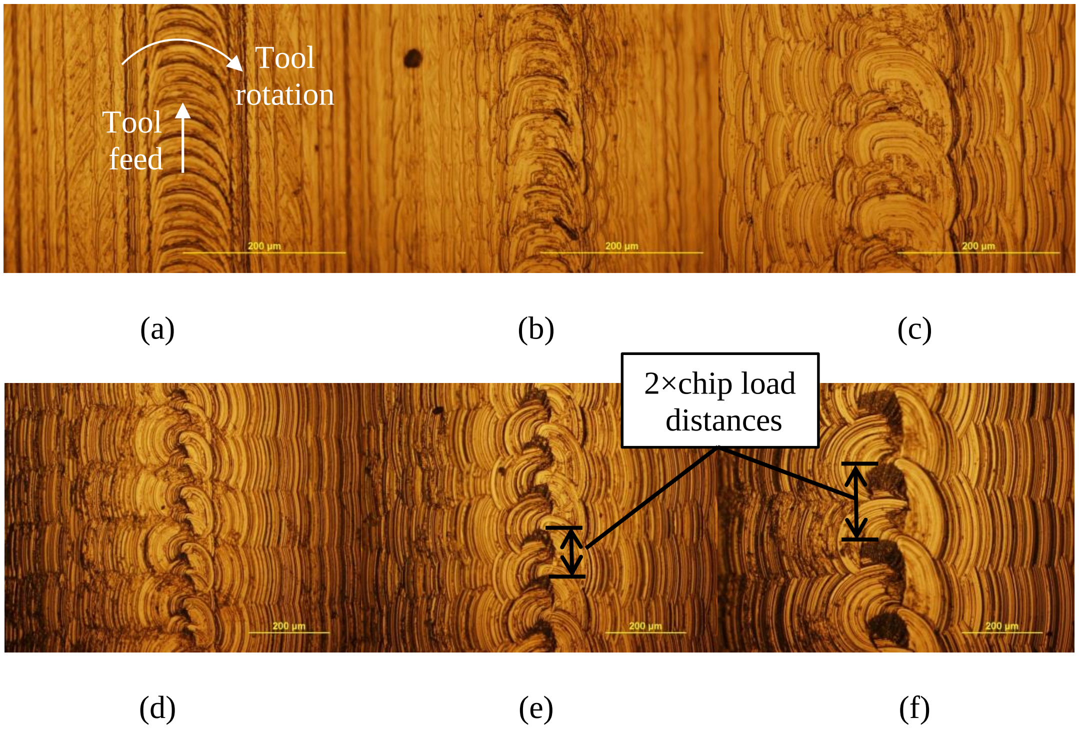

Figure 64. Optical Microscope Images of the Channel Center Milled in 6061-T6 Aluminum Alloy with Uncoated Tool Ø3.175mm, V=60m/min, Ad=0.1mm, MQL: (a) ft=0.005mm/tooth; (b) ft=0.01mm/tooth; (c) ft=0.02mm/tooth; (d) ft=0.03mm/tooth; (e) ft=0.05mm/tooth; (f) ft=0.08mm/tooth.

4.4 Empirical Surface Roughness Modeling

As we can see from discussion above, varying feed rate (or chip load) significantly changes the surface finish in ball end milling. The theoretical surface finish in conventional macro ball end milling was given by [37]:

$$R_a = 0.2568 \frac{{f_t}^2}{D} \tag{4.20}$$

where

R_a : average surface finish (mm)

f_t : chip load (mm/tooth)

D : diameter of ball end milling tool (mm)

In order to normalize the effect of tool diameter and investigate only a chip load effect on surface finish with different tool sizes, equation (4.20) can be modified by multiply the tool diameter on both sides to obtain:

$$D \cdot R_a = 0.2568 f_t^2 \tag{4.21}$$

Plotting the produce of $D \cdot R_a$ against f_t should be a straight line on log-log scale. Experimental surface finish data in micro ball milling, however, fitted to the following empirical equation:

$$D \cdot R_a = 245.3 f_t^{0.7} \tag{4.22}$$

The Figure 66 shows comparison between theoretical surface finish models and experimental surface finish data obtained in macro, meso, and micro milling. The theoretical model derived in the section 4.2 (equation (4.18)) agrees with theoretical model obtained in the previous study (equation (4.21)). Both theoretical models predict surface roughness in macro and meso-scale milling, when chip load is above 100µm. However, the experimental surface roughness in micromilling is much higher than predicted by theory due to size effect, tool edge sharpness effect, smearing of the chips, tool wear, and formation of build-up edge.

In order to further enhance surface finish of milled microchannels additional finishing technique can be used. A separate study developed an effective electrochemical polishing technique that can be used to remove burrs, work hardened layer, and enhance surface finish. Hybrid micromilling and polishing processes allow fabrication of microchannels on polycrystalline Nitinol, 304, and 316L stainless steels with surface finish consistently less than 100 nm R_a (Figure 65).

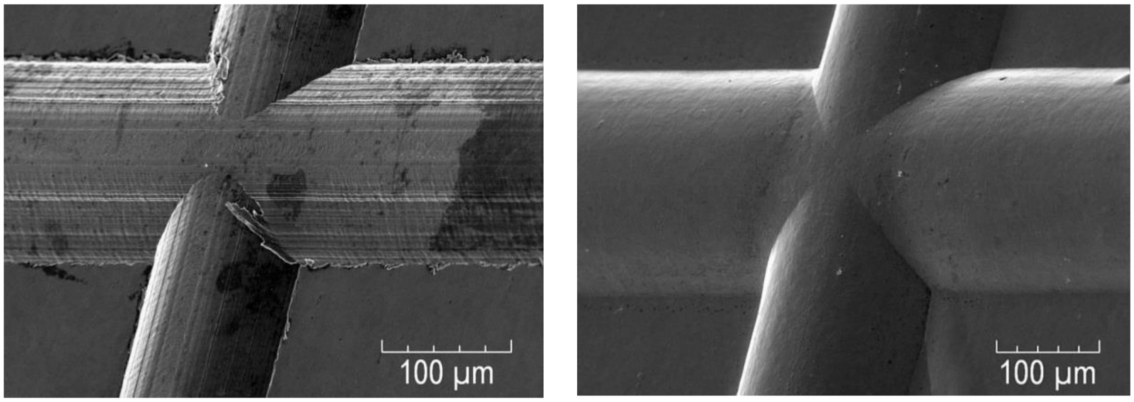

(a) (b)

Figure 65. Micromilling Following by Electrochemical Polishing of 316L Stainless Steel: (a) Micromilled Channel with AlTiN Coated Ø0.198mm Tool, 24 m/min, 0.1 µm/tooth, MQL; (b) Polished Microchannel, 1.25A, 400s.

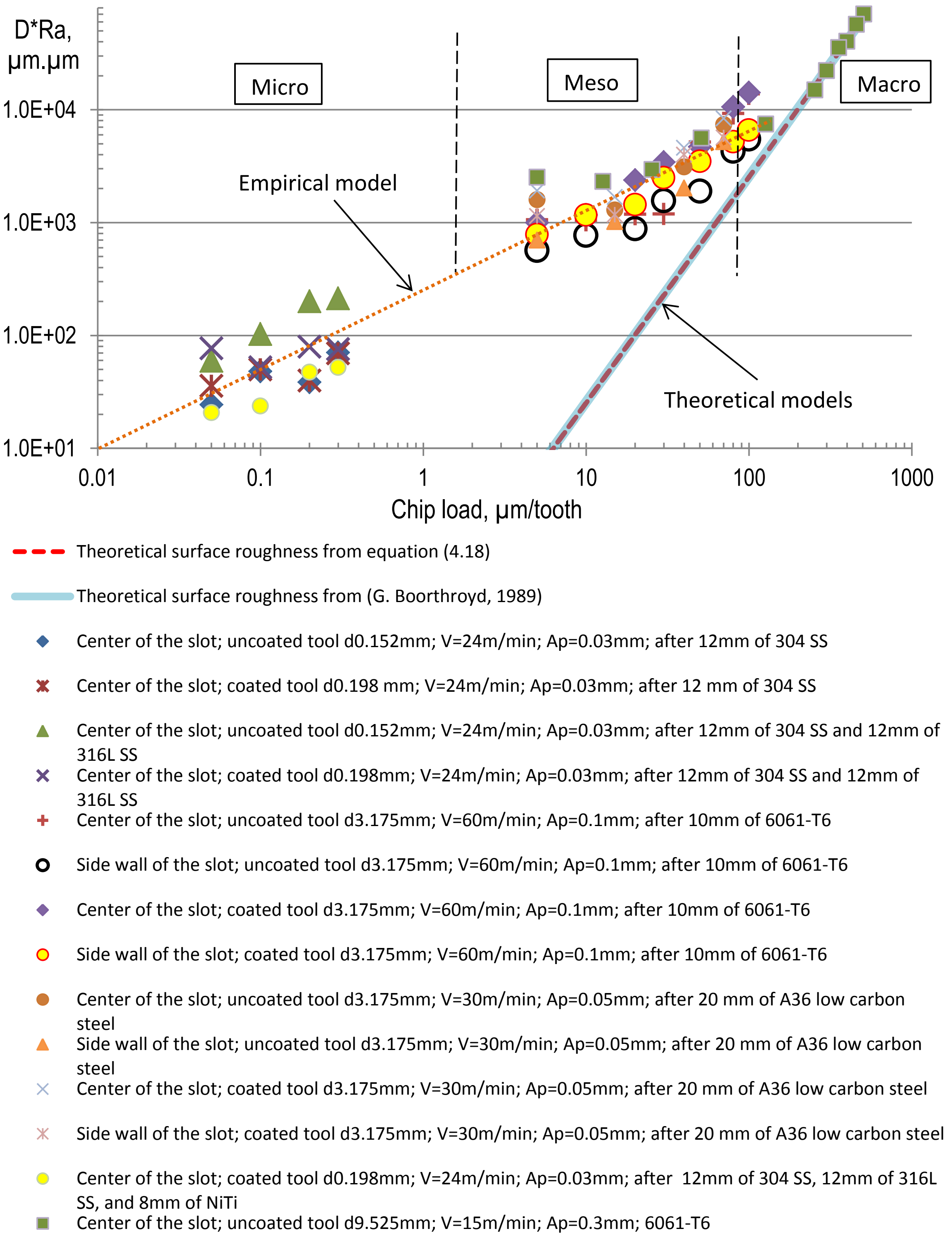

Figure 66. Theoretical Model Verification and Comparison with Experimental R_a Data in Micro, Meso, and Macro Ball End Milling.

4.5 High Aspect Ratio Channels

The depths and the aspect ratios of the microchannels milled on NiTi alloy, 304 and 316L stainless steel are provided in the Table 12. Figure 67 (a-d) shows the surface profiles of milled microchannels on 304 stainless steels with aspect ratios 0.5:1, 0.8:1, 1.1:1, and 1.2:1. The profiles of all machined channels are very similar to the profiles of the tool cutting edges and have a consistent geometry. Figure 68 (a-b) shows the surface profiles of milled microchannels on NiTi alloy with aspect ratios 1.6:1 and 2.2:1. Although, these channels have a consistent geometrical profile at the bottom, the width of the channel is not constant along the axial depth of the channel. The width is larger at the upper part of the channels than it is at the bottom. This could be explained by the geometry and dimensions of the microtool used to machine the channels, which is shown in the Figure 69. When the tool was engaged in the material deeper than 300µm, the conical part of the microtool started participating in the cutting process and resulted in the deviation from the constant width of the channel along its depth. However, this experiment showed that the channels with even higher aspect ratio can be machined providing accurate and consistent geometric profile, if microtools with longer flute length are used. The additional optical microscope images of the high aspect ratio channels milled in 316L stainless steel and NiTi alloy are provided in APPENDIX H.

Table 12. Aspect Ratios of the Microchannels.

Channel #	Workpiece material	Tool diameter, µm	Channel depth, µm	Aspect ratio
1	304 SS 316L SS NiTi	198	95	0.5:1
2			155	0.8:1
3			215	1.1:1
4			245	1.2:1
5	NiTi	198	315	1.6:1
6			435	2.2:1

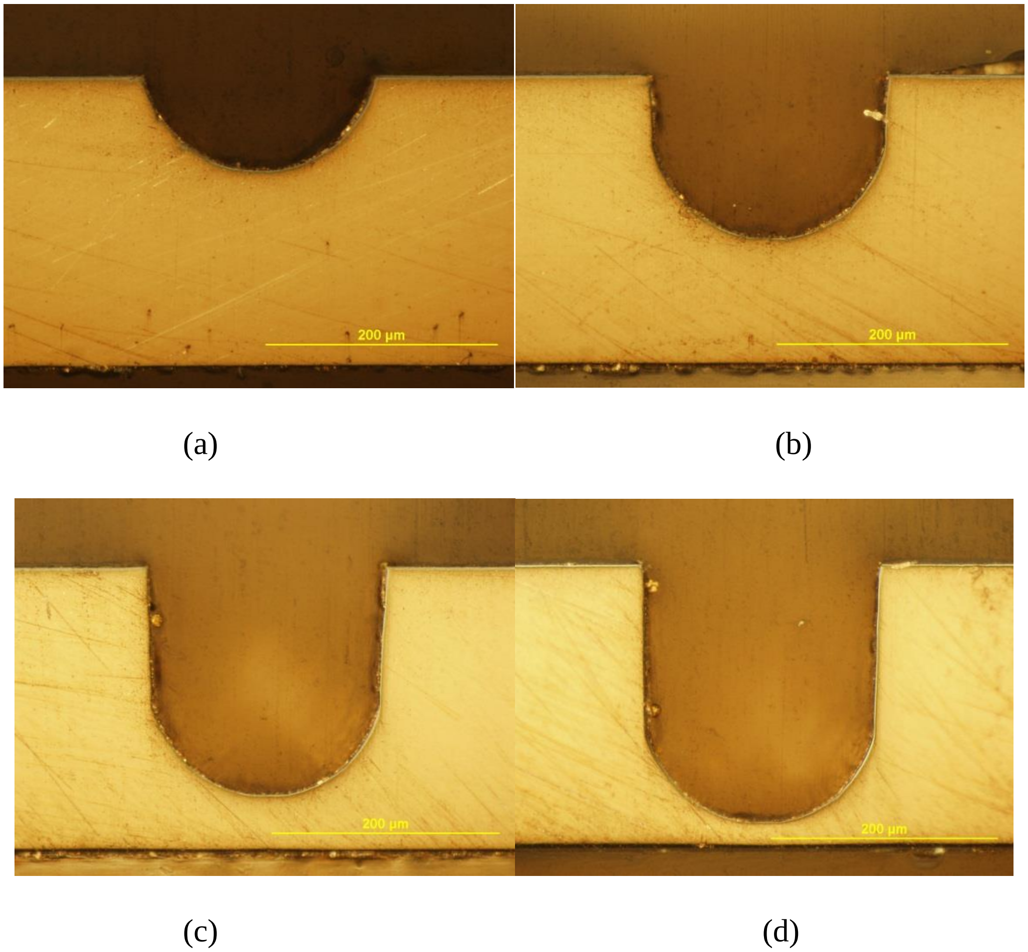

(a) (b)

(c) (d)

Figure 67. Profile of the Microchannels with Aspect Ratios: (a) 0.5:1; (b) 0.8:1; (c) 1.1:1; (d) 1.2:1. AlTiN Coated Tool Ø198µm, f_t=0.1µm/flute, V=24m/min, Ad=0.03mm, 304 Stainless Steel, MQL.

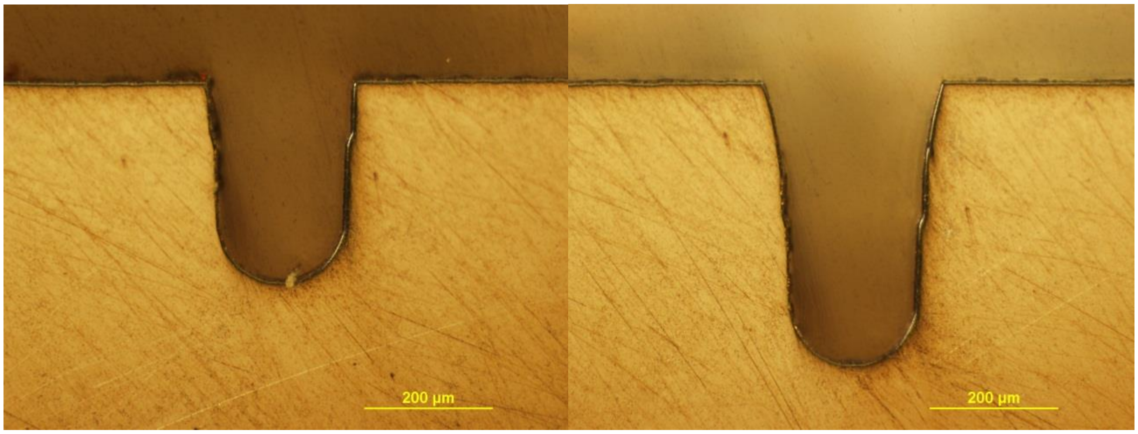

(a) (b)

Figure 68. Profile of the Microchannels with Aspect Ratios: (a) 1.6:1; (b) 2.2:1. AlTiN Coated Tool Ø198µm, f_t=0.1µm/flute, V=24m/min, Ad=0.03mm, NiTi Alloy, MQL.

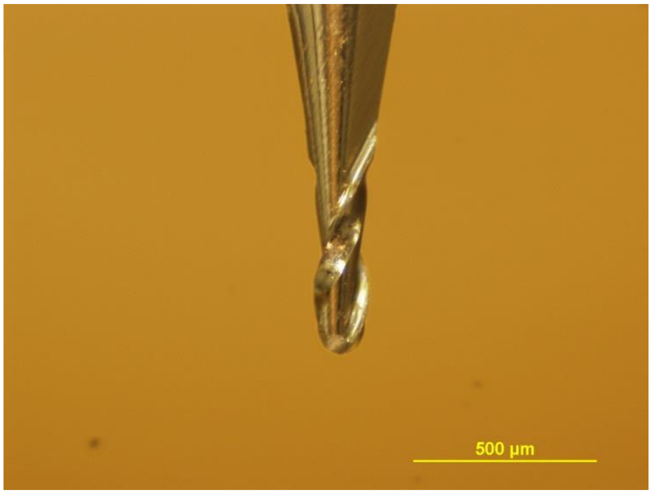

Figure 69. Side View of the AlTiN Coated Ø198µm Ball End Mill.

Figure 70 shows microchannel profile that was machined with excimer laser on nickel super alloy (Figure 70 (b)) and microchannel profile that was machined with ball end mill on NiTi alloy (Figure 70 (a)). The microchannel machined with ball end mill has a more accurate and well defined profile compared to the laser machined microchannel. Also the surface finish of the micromilled channel is much smoother.

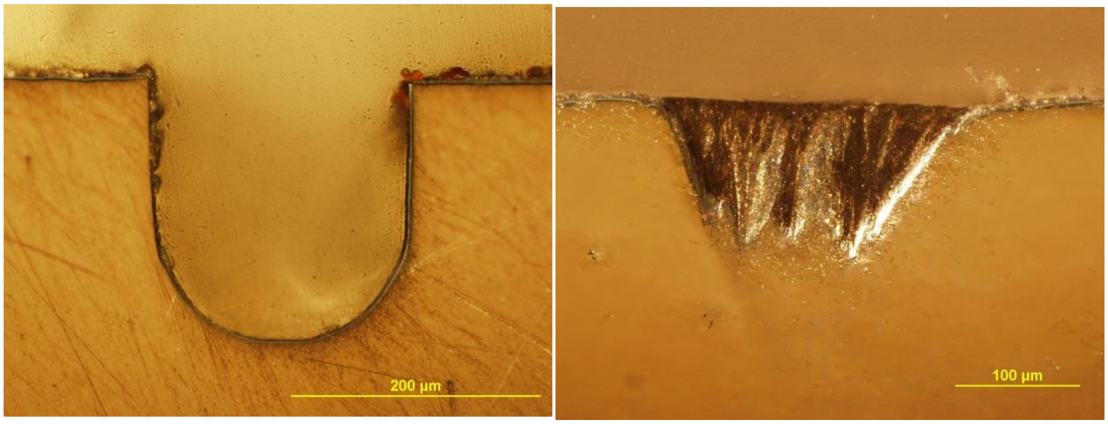

(a) (b)

Figure 70. Profiles of the Microchannels Machined with: (a) AlTiN Ball End Mill Ø198µm, f_t=0.1µm/flute, V=24m/min, Ad=0.03mm, NiTi Alloy, MQL; (b) Ultrashort Excimer Laser, Nickel Super Alloy.

5. CONCLUSIONS

The fabrication of microchannels on biocompatible alloys such as 304, 316L stainless steels, and NiTi alloy using micro ball end milling and electrochemical polishing are presented.

This study shows:

1. Build-up-edges (BUE) and tool wear worsen surface finish and increases burr formation on the milled microchannels.
2. Formation of BUEs and wear of the tool are minimized with AlTiN coated tool and micromilling in minimum quantity lubrication.
3. Down milling produces fewer burrs and results in better surface finish than up milling. Therefore, more burrs and rougher surface finish are generated on one side of the channel than on another.
4. The theoretical surface finish model to predict surface finish in ball end milling is derived, validated with experimental data, and compared to other model from literature. Derived theoretical surface roughness model agrees with theoretical model obtained in the published literature and is applicable for macro/meso scale milling when chip load is lower than 100μm. However, the experimental surface roughness in micromilling is much higher than predicted by theory due to size effect, tool edge sharpness effect, smearing of the chips, tool wear, and formation of build-up edge.

5. Empirical surface roughness model derived in this study shows the dependence of surface finish on chip load in micromilling.
6. Ball-end milled microchannels can be effectively polished by electrochemical polishing technique. Hybrid micromilling and polishing developed in this study allow fabrication of microchannels on polycrystalline 304, 316L stainless steels, and nitinol with surface finish consistently < 100nm R_a.
7. The microchannels with high aspect ratios, and accurate and consistent geometric profile can be effectively machined with micro ball end mills using multiple tool passes. In this study the channels with aspect ratio up to 2.2:1 were successfully machined. The higher aspect ratio can be achieved when using ball end mills with longer flute length.

6. RECOMMENDATIONS

1. Theoretical model to predict surface finish in ball end milling should be extended to flat end milling.
2. Although, this research showed that utilization of AlTiN coated tools resulted in better surface finish and generation of a fewer burrs, the coating layer on the tools was chipped off along the cutting edges after machining relatively short distance (32 mm). Therefore, the adhesion of the coating on the tool should be investigated and the means to improvement the quality of the adhesion should be recommended.
3. The effect of the anisotropy of grain's mechanical properties and grain's crystallographic orientation on surface roughness in micromilling should be investigated.
4. The effect of the dynamics and vibrations of the microtool on surface finish should be investigated

REFERENCES

[1] J. Chae, S. Park and T. Freiheit, "Investigation of micro-cutting operations," *International Journal of Machine Tools & Manufacture,* vol. 46, pp. 313–332 , 2006.

[2] K. Tsuda, K. Okuda, H. Shizuka and M. Nunobiki, "A Study of the Micro-end Milling of Titanium Alloy," *Advanced Materials Research,* vol. 325, pp. 588-593, 2011.

[3] "Micro and Nano manufacturing laboratory," [Online]. Available: http://www.min.uc.edu. [Accessed 02 Sep 2012].

[4] A. Dhanorker and T. Ozel, "An experimental and modeling study on meso/micro end milling process," *ASME 2006 International Manufacturing Science and Engineering Conference,* pp. MSEC2006-21127, 2006.

[5] L. Alting, F. Kimura, N. Hansen and G. Bissacco, "Micro engineering," *Annals of CIRP Keynote STC-O,* vol. 52/2, pp. 635-658, 2003.

[6] S. Mohanty, "Micro drilling of biocompatible materials," *Master of Science. Thesis, Texas A&M University, College Station, TX.* , 2011.

[7] X. Liu, R. Devor, S. Kapoor and K. Ehman, "The mechanics of machining at the micro scale," *Journal of Manufacturing Science and Engineering,* vol. 126, pp. 666–678, 2004.

[8] X. Liu, M. Jun, R. Devor and S. Kappor, "Cutting mechanisms and their influence on dynamic forces, vibrations and stability in micro-end milling," *Proceedings ASME International Mechanical Engineering Congress and Exposition,* pp. 13–20, 2004.

[9] M. Madou, Surface micromachining, chapter fundamentals of microfabrication, Boca Raton, Florida: CRC Press, 1997.

[10] D. Dornfeld, S. Min and Y. Takeuchi, "Recent advances in mechanical micromachining," *CIRP Annals – Manufacturing Technology,* vol. 55, pp. 745-768, 2006.

[11] G. Byrne and D. Dornfeld, "Advancing cutting technology," *CIRP Annals,* vol. 52/2, pp. 483-507, 2003.

[12] T. Hwang, J. Kim, D. Yang, Y. Park and W. Ryu, "Targeted electrohydrodynamic printing for micro-reservoir drug delivery systems," *Journal of Micromechanics and Microengineering,* pp. 23/035012 , 2012.

[13] H. Jha, T. Kikuchi, M. Sakairi and H. Takahash, "Micro-patterning in anodic oxide film on aluminium by laser irradiation," *Electrochimica Acta,* vol. 52, pp. 4724-4733, 2007.

[14] A. Aramcharoen, P. Mativenga, S. Yang, K. Cook and D. Teer, "Evaluation and selection of hard coatings for micro milling of hardened tool steel," *International Journal of Machine Tools & Manufacture,* vol. 48, pp. 1578– 1584, 2008.

[15] J. Kim and D. Kim, "Theoretical analysis of micro-cutting characteristics in ultra-precision machining," *Journal of Materials Processing Technology,* vol. 49, pp. 387–398, 1995.

[16] B. Kim, M. Schmittdiel, F. Degertekin and T. Kurfess, "Scanning grating micro interferometer for MEMS metrology," *Journal of Manufacturing Science and Engineering,* vol. 126, pp. 807–812, 2004.

[17] T. Dow, E. Miller and K. Garrard, "Tool force and deflection compensation for small milling tools," *Precision Engineering,* vol. 28, pp. 31-45, 2004.

[18] G. Schueler, J. Engmann, T. Marx and R. Haberland, "Burr formation and surface characteristics in micro-end milling of titanium alloys," *Proceedings of the CIRP International Conference on Burrs,* pp. 129-138, 2010.

[19] M. Vogler, R. Devor and S. Kapoor, "On the modeling and analysis of machining performance in micro end milling. Part II: Cutting force prediction," *Journal of Manufacturing Science and Engineering,* vol. 126/4, pp. 685–705, 2004.

[20] S. Shimada, N. Ikawa, H. Tanaka, G. Ohmori, J. Uchikoshi and H. Yoshinaga, "Feasibility study on ultimate accuracy in micro cutting using molecular dynamics simulation," *CIRP Annals,* vol. 42/1, pp. 91-94, 1993.

[21] X. Liu and M. Rahman, "Characteristics of high speed micro cutting of tungsten carbide," *Journal of Materials Processing Technology,* vol. 140, pp. 352–357, 2003.

[22] K. Iwata, T. Moriwaka and K. Okuda, "Ultra-high precision diamond cutting of

copper," *Memoirs of Faculty of Engineering, Kobe University,* vol. 31, pp. 93-102, 1984.

[23] M. Vogler, R. Devor and S. Kapoor, "On the modeling and analysis of machining performance in micro end milling. Part I: Surface generation," *Journal of Manufacturing Science and Engineering,* vol. 126/4 , pp. 685–694, 2004.

[24] Y. Furukawa and N. Moronuki, "Effect of material properties on ultra-precise cutting processes," *CIRP Annals,* vol. 37/1, pp. 113-116, 1988.

[25] W. Grzesik, Advanced machining processes of metallic materials: theory, modeling and applications, Amsterdam: Elsevier, 2008.

[26] H. Shizuka, K. Okuda, M. Nunobiki and Y. Inada, "Study on surface roughness in micro end milling of mold material," *Advanced Materials Research,* vol. 325, pp. 594-599, 2011.

[27] T. Ozel, T. Thepsonthi, D. Ulutan and B. Kaftanoglu, "Experiments and finite element simulations on micro-milling of Ti–6Al–4V alloy with uncoated and cBN coated micro-tools," *CIRP Annals - Manufacturing Technology,* vol. 60, pp. 85-88, 2011.

[28] M. Groover, Fundamentals of modern manufacturing: materials, processes and systems, 4th ed, Danver: John Wiley & Sons Inc, 2010.

[29] L. Uriarte, S. Azcarate, A. Herrero, L. Lopez de Lacalle and A. Lamikiz, "Mechanistic modeling of the micro end milling operation," *Journal of Engineering Manufacture,* vol. 222, pp. 23-33, 2007.

[30] P. Davim, Machining of complex sculptured surfaces, London: Springer London Ltd, 2012.

[31] "Knucklebuster. Milling. Ball nose end mills.," [Online]. Available: http://www.knucklebusterinc.com. [Accessed 6 Feb 2012].

[32] H. Li, X. Lai, C. Li, J. Feng and J. Ni, "Modeling and experimental analysis of the effects of tool wear, minimum chip thickness and micro tool geometry on the surface roughness in micro-end-milling," *Journal of Micromechanics and Microengineering,* vol. 18/2, pp. 025006 (12pp), 2008.

[33] K. Hamaguchi , Y. Kagata, H. Shizuka and K. Okuda, "Effect of tool tilting angle on tool wear and surface roughness in micro ball end milling," *Advanced Materials*

Research, vol. 325, pp. 606-611, 2011.

[34] G. Quintana, J. De Ciurana and J. Ribatallada, "Surface roughness generation and material removal rate in ball end milling operations," *Materials and Manufacturing Processes,* vol. 25/6, pp. 386-398, 2010.

[35] T. Jung, M. Yang and K. Lee, "A new approach to analyzing machined surfaces by ball-end milling, part I: Formulation of characteristic lines of cut remainder," *The International Journal of Advanced Manufacturing Technology,* vol. 25, pp. 833–840, 2005.

[36] J. Chen, Y. Huang and M. Chen, "A study of the surface scallop generating mechanism in the ball-end milling process," *International Journal of Machine Tools & Manufacture,* vol. 45, pp. 1077–1084, 2005.

[37] G. Boothroyd and W. Knight, Fundamentals of Machining and Machine Tools, New York: Marcel Dekker Inc, 1989.

[38] M. Hashimura, L. Hassamamontr and D. Dornfeld , "Effect of in-plane exit angle and rake angles on burr height and thickness in face milling operation," *Journal of Manufacturing Science and Engineering,* vol. 121/1, pp. 13-19, 1999.

[39] D. Shiosaki, "Modeling of tool wear and tool fracture in micro milling," *Master of Science. Thesis, Texas A&M University, College Station, TX.,* 2011.

[40] M. Rahman, A. Kumar, A. Senthil and M. Salam, "Experimental evaluation on the effect of minimal quantities of lubricant in milling," *International Journal of Machine Tools and Manufacturing,* vol. 42, pp. 539-547, 2002.

[41] S. Kajaria, S. Chittipolu, S. Adera and W. Hung, "Micromilling in minimum quantity lubrication," *Machining Science and Technology: An International Journal,* vol. 16/4, pp. 524-546, 2012.

[42] "AZoM™, Pty.Ltd., Grade 316L – properties, fabrication and applications," [Online]. Available: http://www.azom.com/. [Accessed 28 Nov 2012].

[43] "Performance Micro Tool," [Online]. Available: http://www.pmtnow.com/end_mills/tools/TR-2BN.asp. [Accessed 23 Nov 2012].

[44] "Mitsubishi Materials. Carbide and Tools Division. Solid Carbide Blanks," [Online]. Available: http://blank.mitsubishicarbide.com. [Accessed 24 Nov 2012].

[45] "MSC Industrial Supply Co. Accupro High Performance Milling," [Online].

Available: http://www1.mscdirect.com. [Accessed 13 Dec 2012].

[46] E. Oberg, F. Jones, H. Horton and H. Ryfeel, Machinery's hand book 28th edition, New York: Industrial Press Inc, 2009.

[47] "HAAZ Automation. Haas Automation Ltd," [Online]. Available: http://www.haas.co.uk. [Accessed 29 Nov 2012].

[48] "UNIST Environmentally Friendly Lubrication," [Online]. Available: http://unist.com. [Accessed 13 Dec 2012].

[49] "Raynger ST. Raytec," [Online]. Available: http://www.instrumart.com. [Accessed 21 Jan 2013].

[50] "Struers. Marking, Cleaning, Drying, and Storing.," [Online]. Available: http://www.struers.com. [Accessed 21 Jan 2013].

[51] "GF AgieCharmilles Management Ltd," [Online]. Available: http://www.gfac.com. [Accessed 13 Dec 2012].

APPENDIX A

EQUIPMENT

A.1 HAAS OM2 specifications.

Table A. 1 HAAS OM2 Milling Machine Specification [47].

Travels	**S.A.E.**	**Metric**
X axis	12’’	305 mm
Y axis	10’’	254 mm
Z axis	12’’	305 mm
Table	**S.A.E.**	**Metric**
Length	20”	508 mm
Width	10’’	254 mm
Max weight on table	150 lb	68 kg
Spindle	**S.A.E.**	**Metric**
Taper	ISO/20	ISO/20
MAX speed	50000 rpm	50000 rpm
MIN speed	1000 rpm	1000 rpm
Feed rates	**S.A.E.**	**Metric**
Rapids on X, Y, and Z	757 in/min	19.2 m/min
MAX cutting	500 in/min	12.7 m/min
Accuracy	**S.A.E.**	**Metric**
Positioning	-	±0.005 mm
Repeatability	-	±0.003 mm
General	**S.A.E.**	**Metric**
Air required	1 scfm, 40-70 psi	28 L/min, 2.8-4.8 bar
Machine weight	1500 lb	680 kg

Figure A. 1 HAAS OM2 CNC Milling Maching [47].

A.2 UNIST Cool Lubricator System

The Cool Lubricator System is used to provide micro mist during cutting process. The micro mist flow can be adjusted using an air metering screw, a pulse generator and a 0.2-1.0 cc stroke liquid metering pump. The amount of droplets of the coolant per cycle can be set in the range from 0.1 to 3.0 droplets per cycle. The number of cycles can be adjusted in the range from 5 to 200 cycles per minute. The capacity of the coolant reservoir of the Cool Lubricant System is 10 ounces, which is about 9000 drops of coolant. The amount of coolant in the micro mist can be adjusted using a knob on the metering pump. The flexible plastic nozzle with magnetic base is attached to the spindle of the milling machine and can be adjusted to control the direction of the micro mist flow [48].

Cooluble 2210 was used as a lubricant for the experiments. This lubricant has great cooling and lubricating properties. The polar properties of the Cooluble provide formation of the uniform lubricating layer with strong bonds at the metal surface. It reduces friction in the cutting zone by 50 % compared to regular mineral oils, which leads to better surface finish and longer tool life. Cooluble 2210 is natural and non-toxic coolant without petroleum products. Thus, it has no hazards for the people who work in the machine shop and results in a very low environmental pollution [48].

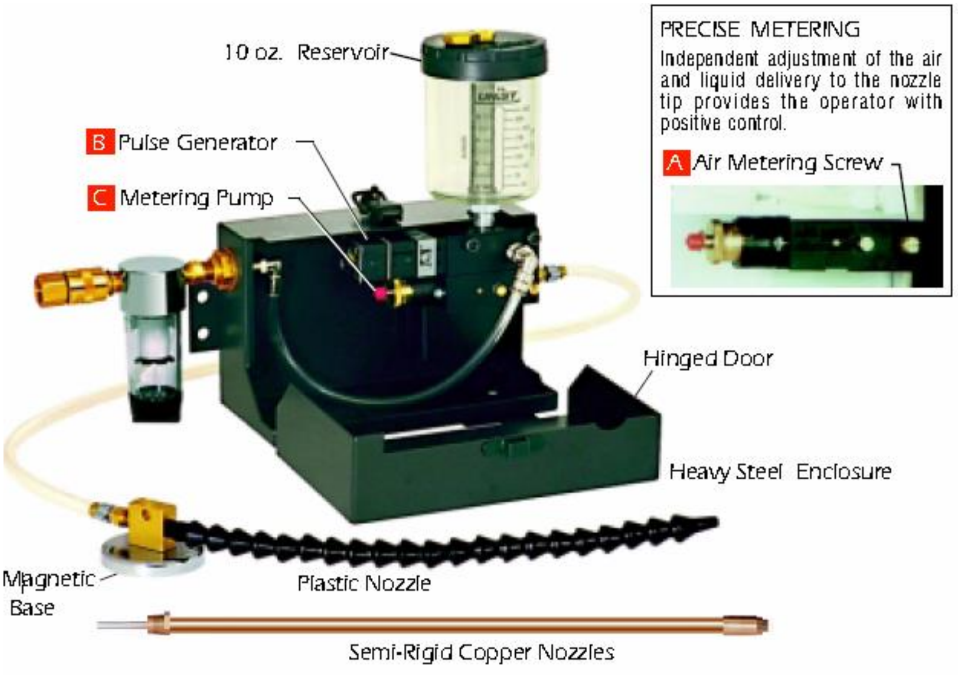

Independent adjustment of the air and liquid delivery to the nozzle tip provides the operator with positive control.

Figure A. 2 UNIST Cool Lubricator System [6].

A.3 Keyence CCD Laser Displacement Sensor LK-G Series

Keyence laser can be used for high accuracy measurements of 2D dimensions or displacements of the spinning or vibrating objects with high frequency. The surface of the measured object can vary from highly reflective to completely dull. LK navigator software is used with the laser in order to set laser intensity depending on the surface reflectivity of the measured component [6].

Table A. 2 Keyence CCD Laser Specification [39].

Sampling speed, KHz	50
Measuring range, mm	150±40
Working distance (between laser and object), mm	152
Resolution, µm	0.1

A.4 Zygo NewView 100 Interferometer

Zygo interferometer is utilized to analyze three dimensional surface topography and measure surface roughness. It is used to measure diverse types of surfaces such as polished surfaces, macro and micro machined surfaces, and more. Also, measurements can be conducted for different materials such as metals, ceramics, polymers, and composites. However, in order to provide accurate measurements it should be used only for highly reflective surfaces and materials.

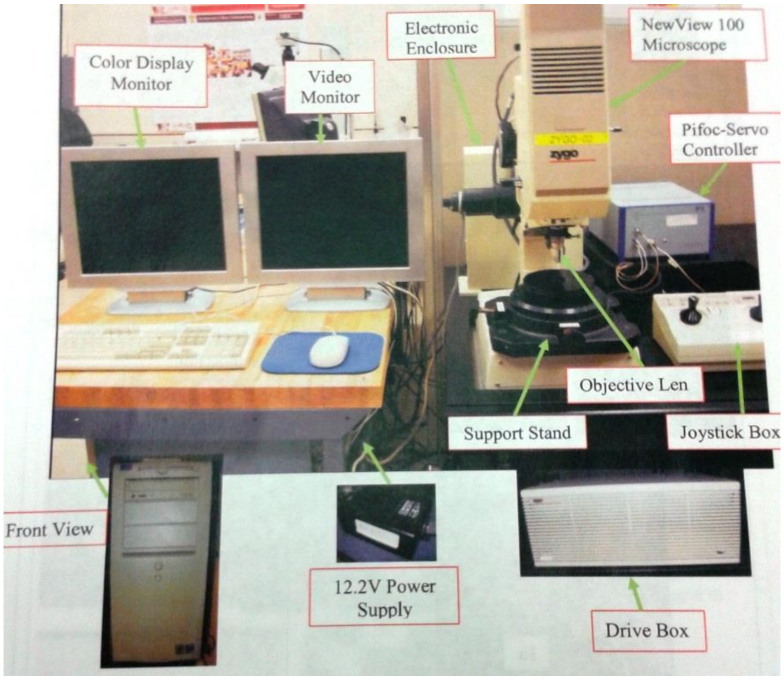

Figure A. 3 Zygo NewView 100 System.

Table A. 3 Zygo NewView 100 System Specification.

Vertical travel	130 mm
Camera size	640 x 480 pixels
Vertical resolution	0.1 nm
Scanning depth (height)	10 µm – 100 µm
Working distance	11.1 mm
Objective Lens	2.5x, 5x, 10x

A.5 Raytec Rangers ST Pyrometer

The pyrometer is noncontact infrared thermometer that is used to accurately measure the temperature of the surface form a distance in dangerous or difficult to reach places, or in cases when no-contact temperature measurements are required.

Table A. 4 Raytec Rangers ST Pyrometer Specification [49].

Accuracy (at ambient temperature)	±1°C
Repeatability	±1°C
Response time	500 mSec
Ambient operating range	0 to 50°C
Measured temperature range	-32 to 600°C
Display resolution	0.1°C

A.6 Ultrasonic Cleaner Metason 200

Ultrasonic cleaner is used for effective cleaning of pores and cavities, removing debris and chips after grinding, polishing or machining.

Table A. 5 Ultrasonic Cleaner Metason 200 Specification [50].

Output power	140 W
Tank dimensions (W x D x H)	290 x 240 x 150 mm
Tank capacity	9.5 l
Overall dimensions (W x D x H)	400 x 395 x 370 mm
Weight	9.6 kg

A.7 CUT 20P AgieCharmilles Wire EDM

The electrical discharging machine is used to cut through pieces from metal sheets with brass wire (electrode). Wire with diameter from 0.15 mm to 0.30 mm can be utilized on this machine. During cutting new wire is continuously feeding through the work piece which prevents wear of the wire to affect the precision of the machining and provides constant size of cut. The dimension of the table of the wire EDM is 350x250x250 mm [51]. EDM provides low surface roughness and prevents from bending of the workpiece during machining, which is important for preliminarily machining of the work pieces for further micromachining.

Figure A. 4 AgieCharmilles Wire EDM **[51]**.

Table A. 6 AgieCharmilles Wire EDM Specification [51].

Machine dimensions, mm	2500 x 2500 x 2200
Total weight, kg	3000
X, Y, Z travel, mm	350 x 250 x 250
U, V travel, mm	90 x 90
MAX workpiece dimensions, mm	900 x 680 x 250
MAX workpiece weight, kg	400
Wire diameters, mm	0.15-0.3
Best surface finish Ra, µm	<0.25

APPENDIX B

TECHNICAL DRAWINGS

B.1 Technical Drawing of Aluminum Block for Securing of Small Samples during Micromilling.

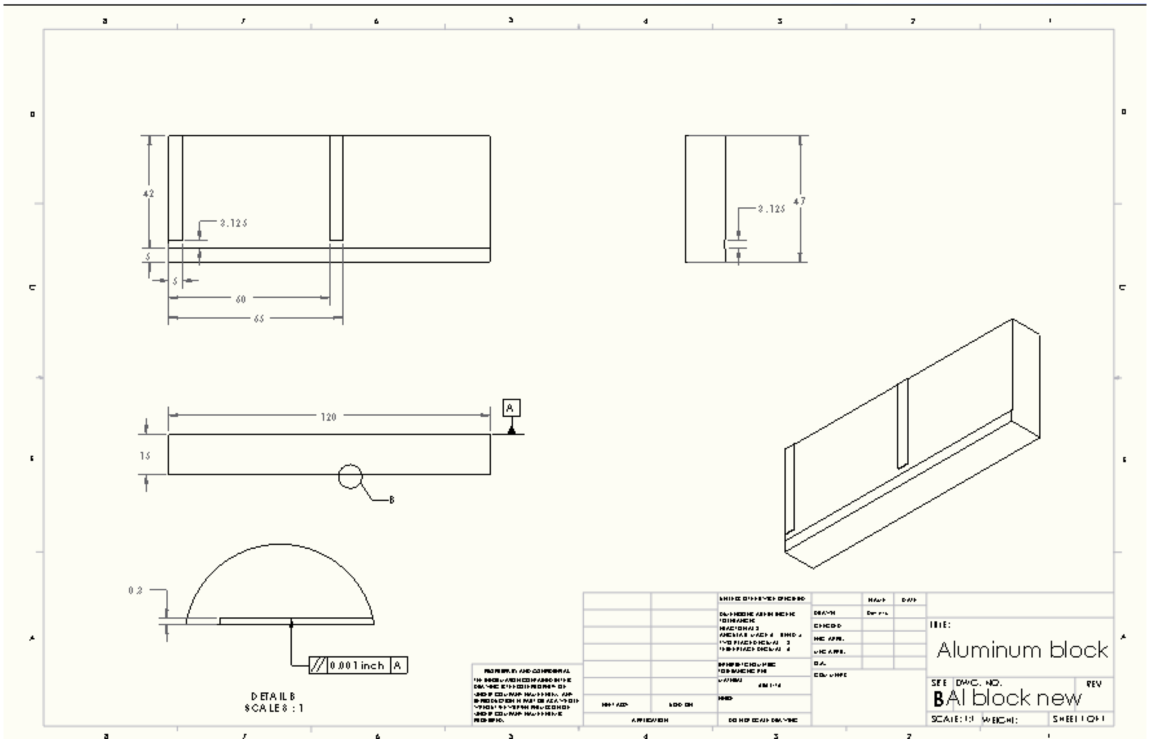

Figure B. 1 Technical Drawing of Aluminum Block.

APPENDIX C

CNC G-CODES

C.1 Spindle warm-up program:

```
O02026 (NSK 20 MIN SPINDLE WARM-UP)
M03 S10000
G04 P120.
M03 S20000
G04 P180.
M03 S25000
G04 P180.
M03 S30000
G04 P180.
M03 S35000
G04 P180.
M03 S40000
G04 P180.
M03 S50000
G04 P180.
M05
M30
```

C.2 Program for micromilling of 304 and 316L stainless steels:

```
O10003
(Ra Milling Dimitry)
(Milling with ball end mill of the cross 9/19/2012)
N40 G00 G17 G40 G90 G21
(STANDARD START-UP SETTINGS)
N45 T1
(IDENTIFIES TOOLING)
N50 G54 G01 Z25. F100.
N55 X0. Y0.
(COORDINATES SET IN LINE G54 IN OFFSETS)
(MUST SET ZEROES)
N60 S38377 M03
(SETS SPINDLE SPEED AND TURNS ON CLOCK-WISE)
N65 G01 Y2.
N70 Z2.
N75 Z-0.03 F1.3
(LOWERS TOOL TO Z AT 1.3 MM/MINUTE)
N80 G91 G01 Y3. F23.
```

```
(MOVES INCREMENTAL DISTANCE IN +Y DIRECTION with 2.7 MM/MINUTE)
N85 G90 Z2.
(TOOL MOVES IN +Z DIRECTION)
N90 G91 X-1.5 Y-1.5
(MOVES INCREMENTAL DISTANCE IN -X and -Y DIRECTION with 2.7
MM/MINUTE)
N95 G90 Z-0.03 F1.3
N100 G91 X3. F23.
N105 G90 Z2.
N110 G90 X0. Y25. F100.
N115 Z-0.03 F1.3
(LOWERS TOOL TO Z AT 1.3 MM/MINUTE)
N120 G91 G01 Y3. F23.
(MOVES INCREMENTAL DISTANCE IN +Y DIRECTION with 2.7 MM/MINUTE)
N125 G90 Z2.
(TOOL MOVES IN +Z DIRECTION)
N130 G91 X-1.5 Y-1.5
(MOVES INCREMENTAL DISTANCE IN -X and -Y DIRECTION with 2.7
MM/MINUTE)
N135 G90 Z-0.03 F1.3
N140 G91 X3. F23.
(MOVES INCREMENTAL DISTANCE IN +X DIRECTION with 2.7 MM/MINUTE)
N145 G90 G01 Z25. F100.
(TOOL MOVES IN +Z DIRECTION)
N150 M30
```

C.3 Program for micromilling of NiTi alloy:

```
O10004
(Ra Milling Dimitry NiTi)
(Milling with ball end mill of the cross 2/04/2013)
N40 G00 G17 G40 G90 G21
(STANDARD START-UP SETTINGS)
N45 T1
(IDENTIFIES TOOLING)
N50 G54 G01 Z25. F100.
N55 X0. Y0.
(COORDINATES SET IN LINE G54 IN OFFSETS)
(MUST SET ZEROES)
N60 S38377 M03
(SETS SPINDLE SPEED AND TURNS ON CLOCK-WISE)
N65 Z2.
N70 Z-0.03 F1.3
(LOWERS TOOL TO Z AT 1.3 MM/MINUTE)
```

```
N75 G91 G01 Y4. F23.
(MOVES INCREMENTAL DISTANCE IN +Y DIRECTION with 2.7 MM/MINUTE)
N80 G90 Z2.
(TOOL MOVES IN +Z DIRECTION)
N85 G91 X+2. Y+4.
(MOVES INCREMENTAL DISTANCE IN +X and +Y DIRECTION with 2.7
MM/MINUTE)
N90 G90 Z-0.03 F1.3
N95 G91 y+4. F23.
N100 G90 G01 Z25. F100.
(TOOL MOVES IN +Z DIRECTION)
N105 M30
```

C.4 Program for runout measurements while micromilling of CP titanium:

```
O10002
(Milling Dimitry for vibration)
(Milling with ball end mill 1 row 4/27/2012)
N40 G00 G17 G40 G90 G21
(STANDARD START-UP SETTINGS)
N45 T1
(IDENTIFIES TOOLING)
N50 G54 G01 Z25. F100.
N55 X0. Y0.
(COORDINATES SET IN LINE G54 IN OFFSETS)
(MUST SET ZEROES)
N60 G01 X3. Y-3.
N65 Z-0.038 F100.
N70 G04 P30. (Pauses tool 20s and I take measurments1)
N75 G01 Z-0.076 F100.
(LOWERS TOOL TO Z AT 100 MM/MINUTE)
N80 G04 P30. (Pauses tool 20s and I take measurments2)
N85 S27238 M03
(SETS SPINDLE SPEED AND TURNS ON CLOCK-WISE)
N90 G04 P30. (Pauses tool 20s and I take measurments3)
N95 Z-0.038 F100.
N100 G04 P30. (Pauses tool 20s and I take measurments4)
N105 G91 G01 Y11. F2.7
(MEAUSURMENTS5)
N110 G04 P1.5
N115 G90 G01 Z-0.076 F1.3
N120 G04 P1.5
N125 G91 G01 Y3. F2.7 (MEASURMENTS6)
N130 G90 G01 Z25. F100.
```

```
(TOOL MOVES IN +Z DIRECTION)
N135 M30
```

C.5 Program for mesomilling of 6061-T6 aluminum alloy:

```
O10004
(Ra validation Milling Dimitry)
(Meso Milling with ball end mills of aluminum 10/29/2012)
N40 G00 G17 G40 G90 G21
(STANDARD START-UP SETTINGS)
N45 T1
(IDENTIFIES TOOLING)
N50 G54 G01 Z25. F200.
N55 X0 Y-3.5
(COORDINATES SET IN LINE G54 IN OFFSETS)
(MUST SET ZEROES)
N60 S6020 M03
(SETS SPINDLE SPEED AND TURNS ON CLOCK-WISE)
N65 Z-0.1
(LOWERS TOOL TO Z)
N70 G90 Y10. F120.4
(MOVES INCREMENTAL DISTANCE IN +Y DIRECTION with 120.4 MM/MINUTE)
N75 G90 Z25. F200.
(TOOL MOVES IN +Z DIRECTION)
N180 M30
```

C.6 Program for mesomilling of A36 low carbon steel:

```
O10004
(Ra validation Milling Dimitry)
(Meso Milling with ball end mills of aluminum 10/29/2012)
N40 G00 G17 G40 G90 G21
(STANDARD START-UP SETTINGS)
N45 T1
(IDENTIFIES TOOLING)
N50 G54 G01 Z25. F200.
N55 X0 Y-3.5
(COORDINATES SET IN LINE G54 IN OFFSETS)
(MUST SET ZEROES)
N60 S3009 M03
(SETS SPINDLE SPEED AND TURNS ON CLOCK-WISE)
N65 Z-0.05
(LOWERS TOOL TO Z)
```

```
N70 G90 Y20. F120.4
(MOVES INCREMENTAL DISTANCE IN +Y DIRECTION with 120.4
MM/MINUTE)
N75 G90 Z25. F200.
(TOOL MOVES IN +Z DIRECTION)
N180 M30
```

C.7 Program for micromilling of high aspect ratio channels:

```
O10006
(Milling High aspect ratio Dimitry)
(Milling with ball end mill 4/06/2013)
N40 G00 G17 G40 G90 G21
(STANDARD START-UP SETTINGS)
N45 T1
(IDENTIFIES TOOLING)
N50 G54 G01 Z20. F100.
N55 X0. Y0.
(COORDINATES SET IN LINE G54 IN OFFSETS)
(MUST SET ZEROES)
N60 S38377 M03
(SETS SPINDLE SPEED AND TURNS ON CLOCK-WISE)
N65 G01 Y2.
N70 Z2.
N75 G90 Z-0.03 F1.3
(LOWERS TOOL TO Z AT 1.3 MM/MINUTE)
N80 G91 G01 Y3.5 F7.7
(MOVES INCREMENTAL DISTANCE IN +Y DIRECTION with 7.7 MM/MINUTE)
N85 G90 Z-0.06 F1.3
(LOWERS TOOL TO Z AT 1.3 MM/MINUTE)
N90 G91 G01 Y-3.5 F7.7
(MOVES INCREMENTAL DISTANCE IN +Y DIRECTION with 7.7 MM/MINUTE)
N95 G90 Z-0.09 F1.3
(LOWERS TOOL TO Z AT 1.3 MM/MINUTE)
N100 G91 G01 Y3.5 F7.7
(MOVES INCREMENTAL DISTANCE IN +Y DIRECTION with 7.7 MM/MINUTE)
N105 G90 Z-0.12 F1.3
(LOWERS TOOL TO Z AT 1.3 MM/MINUTE)
N110 G91 G01 Y-3.5 F7.7
(MOVES INCREMENTAL DISTANCE IN +Y DIRECTION with 7.7 MM/MINUTE)
N115 G90 Z-0.15 F1.3
(LOWERS TOOL TO Z AT 1.3 MM/MINUTE)
N80 G91 G01 Y3.5 F7.7
(MOVES INCREMENTAL DISTANCE IN +Y DIRECTION with 7.7 MM/MINUTE)
```

```
N120 G90 Z-0.18 F1.3
(LOWERS TOOL TO Z AT 1.3 MM/MINUTE)
N125 G91 G01 Y-3.5 F7.7
(MOVES INCREMENTAL DISTANCE IN +Y DIRECTION with 7.7 MM/MINUTE)
N130 G90 Z-0.21 F1.3
(LOWERS TOOL TO Z AT 1.3 MM/MINUTE)
N135 G91 G01 Y3.5 F7.7
(MOVES INCREMENTAL DISTANCE IN +Y DIRECTION with 7.7 MM/MINUTE)
N140 G90 Z2.
(TOOL MOVES IN +Z DIRECTION)
N145 G90 G01 X0. Y0. Z20. F100.
(TOOL MOVES IN +Z DIRECTION)
N150 M30
```

APPENDIX D

RAW SURFACE FINISH DATA

D.1 Measured surface finish after micromilling

Table D. 1 Measured Surface Finish after Micromilling

Material	Tool	V [m/min]	f_t [μm/tooth]	R_a Center [μm]
304	Uncoated Ø0.152 mm	24	0.05	0.16
			0.1	0.32
			0.2	0.25
			0.3	0.47
	AlTiN Coating Ø0.198 mm	24	0.05	0.18
			0.1	0.25
			0.2	0.20
			0.3	0.35
316L	Uncoated Ø0.152 mm	24	0.05	0.39
			0.1	0.68
			0.2	1.32
			0.3	1.40
	AlTiN Coating Ø0.198 mm	24	0.05	0.39
			0.1	0.26
			0.2	0.40
			0.3	0.38
NiTi	AlTiN Coating Ø0.198 mm	24	0.05	0.10
			0.1	0.12
			0.2	0.24
			0.3	0.26

D.2 Measured surface finish after mesomilling

Table D. 2 Measured Surface Finish after Mesomilling.

Material	Tool	V [m/min]	f_t [µm/tooth]	R_a Center [µm]	R_a Side wall [µm]
6061-T6	Uncoated Ø3.175 mm	60	5	0.33	0.18
			10	0.33	0.24
			20	0.37	0.28
			30	0.38	0.49
			50	1.63	0.60
			80	2.91	1.35
			100	4.34	1.73
	AlTiN Coating Ø3.175 mm	60	5	0.31	0.25
			10	0.37	0.37
			20	0.75	0.45
			30	1.08	0.79
			50	1.48	1.10
			80	3.34	1.64
			100	4.46	2.07
A36	Uncoated Ø3.175 mm	30	5	0.50	0.22
			15	0.41	0.32
			40	0.98	0.64
			70	2.33	1.63
	AlTiN Coating Ø3.175 mm	30	5	0.60	0.36
			15	0.53	0.37
			40	1.44	1.26
			70	2.63	1.79

APPENDIX E

FFT PLOTS FOR TOOL RUNOUT ANALYSIS

E.1 FFT for feed rate 2.7mm/min and spindle speed 27238rpm.

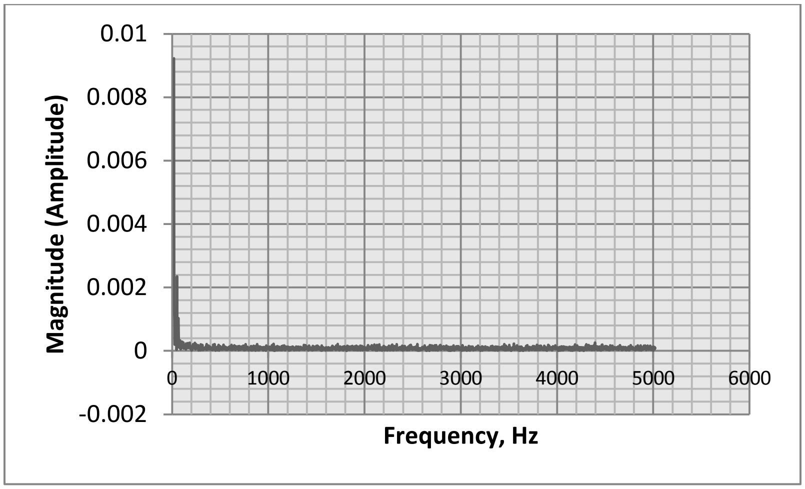

Figure E. 1 FFT, Stationary Spindle.

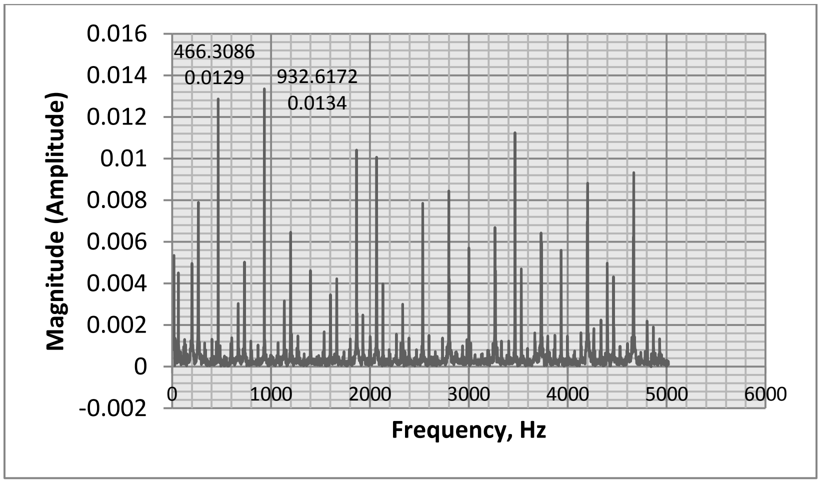

Figure E. 2 FFT, Rotating Spindle without Machining, Ball End Mill ϕ0.152 mm, Spindle Speed 27238 rpm.

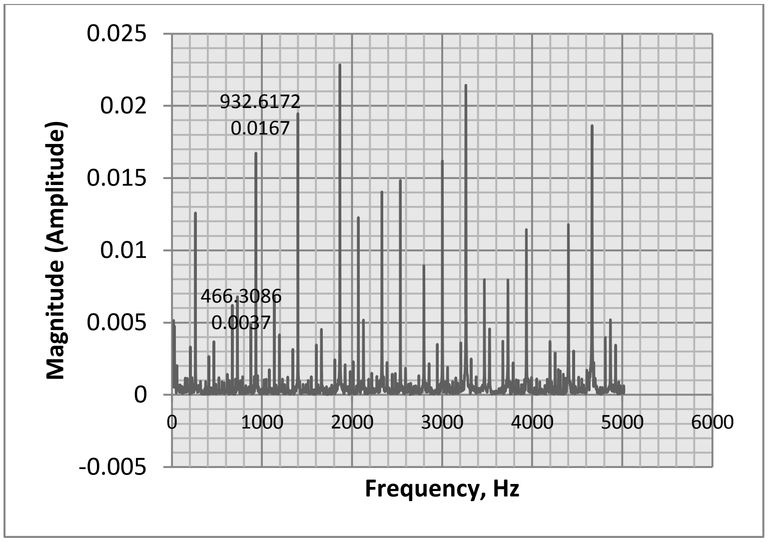

Figure E. 3 FFT, Milling CP Titanium, Ball End Mill ϕ0.152 mm, Spindle Speed 27238 rpm, Feed Rate 2.7 mm/min, Depth of Cut 38 µm, MQL.

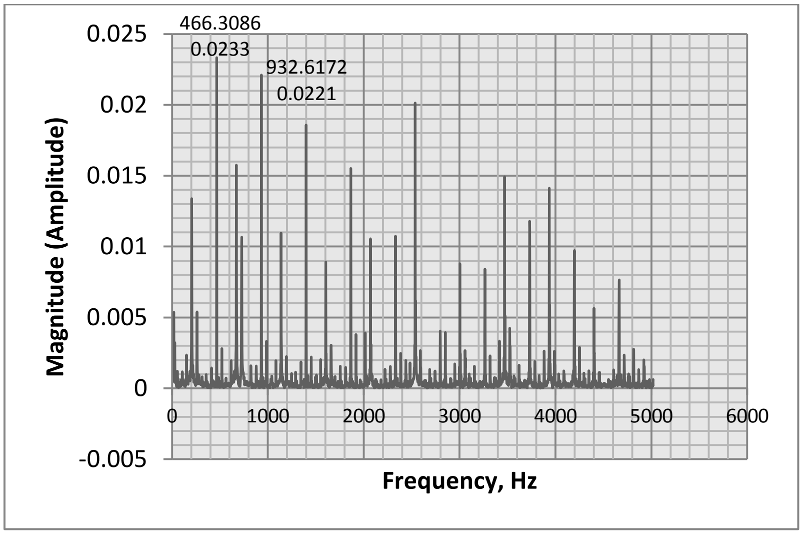

Figure E. 4. FFT, Milling CP Titanium, Ball End Mill ϕ0.152 mm, Spindle Speed 27238 rpm, Feed Rate 2.7 mm/min, Depth of Cut 76 µm, MQL.

E.2 FFT for feed rate 5.4mm/min and spindle speed 27238rpm.

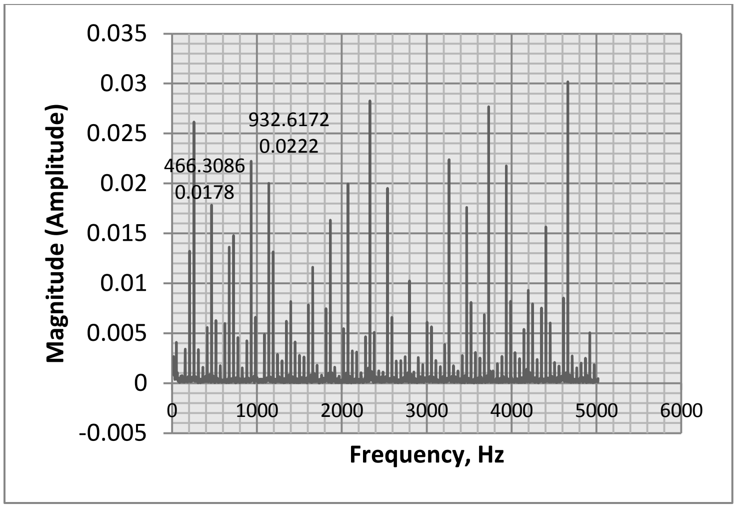

Figure E. 5 FFT, Milling CP Titanium, Ball End Mill ϕ0.152 mm, Spindle Speed 27238 rpm, Feed Rate 5.4 mm/min, Depth of Cut 38 µm, MQL.

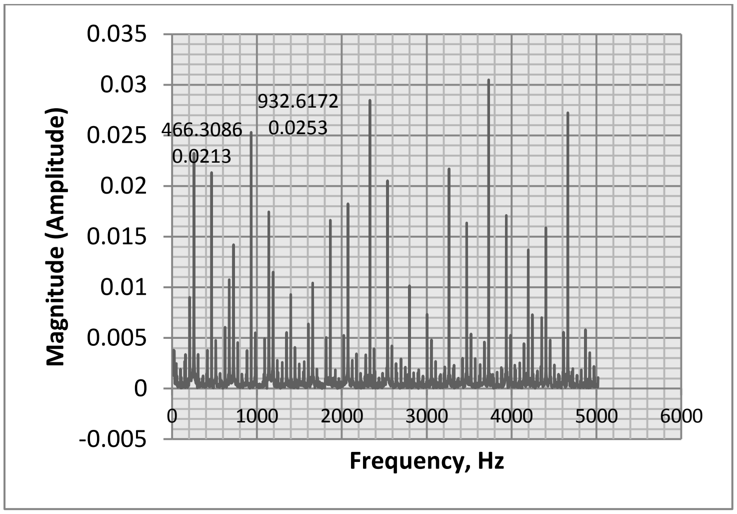

Figure E. 6 FFT, Milling CP Titanium, Ball End Mill ϕ0.152 mm, Spindle Speed 27238 rpm, Feed Rate 5.4 mm/min, Depth of Cut 76 µm, MQL.

E.3 FFT for feed rate 4.2mm/min and spindle speed 41904rpm.

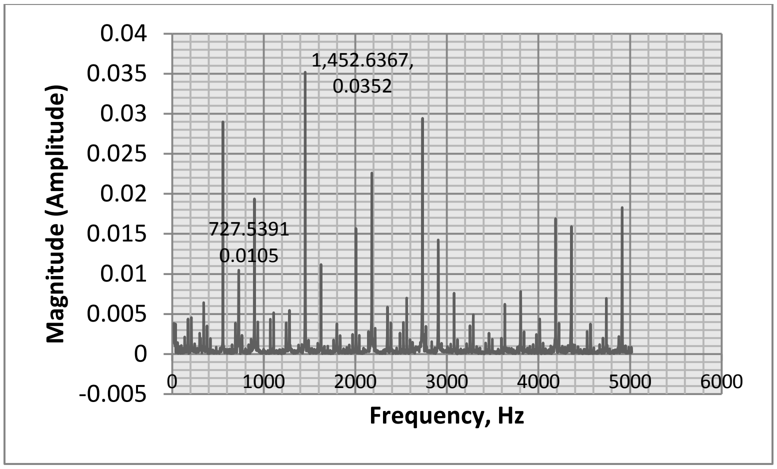

Figure E. 7 FFT, Milling CP Titanium, Ball End Mill ϕ0.152 mm, Spindle Speed 41904 rpm, Feed Rate 4.2 mm/min, Depth of Cut 38 µm, MQL.

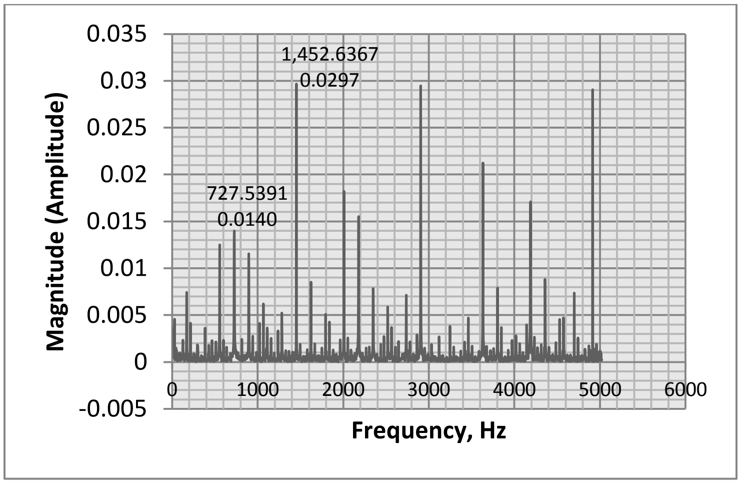

Figure E. 8 FFT, Milling CP Titanium, Ball End Mill ϕ0.152 mm, Spindle Speed 41904 rpm, Feed Rate 4.2 mm/min, Depth of Cut 76 µm, MQL.

E.4 FFT for feed rate 8.4mm/min and spindle speed 41904rpm.

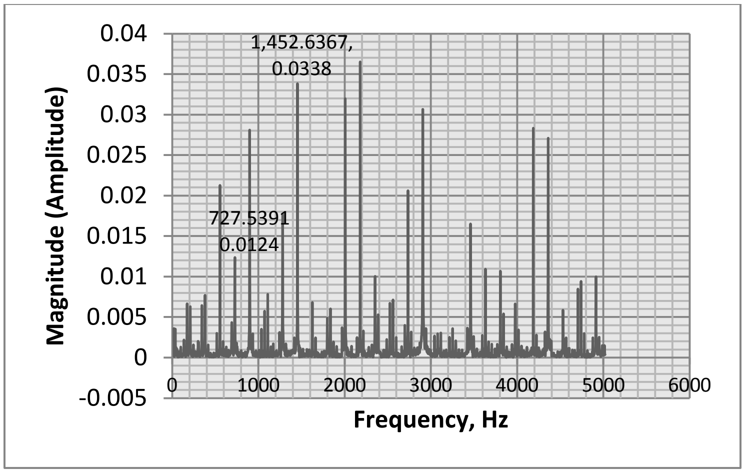

Figure E. 9 FFT, Milling CP Titanium, Ball End Mill ϕ0.152 mm, Spindle Speed 41904 rpm, Feed Rate 8.4 mm/min, Depth of Cut 38 µm, MQL.

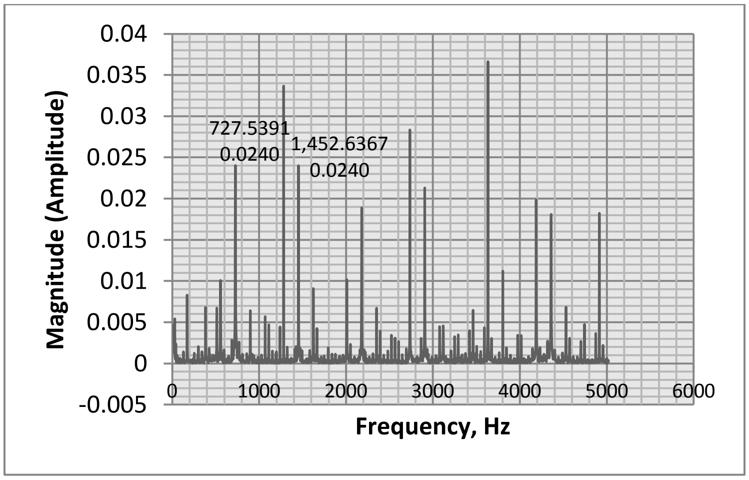

Figure E. 10 FFT, Milling CP Titanium, Ball End Mill ϕ0.152 mm, Spindle Speed 41904 rpm, Feed Rate 8.4 mm/min, Depth of Cut 76 µm, MQL.

APPENDIX F

SOLIDWORKS SIMULATIONS FOR SURFACE ROUGHNESS ANALYSIS

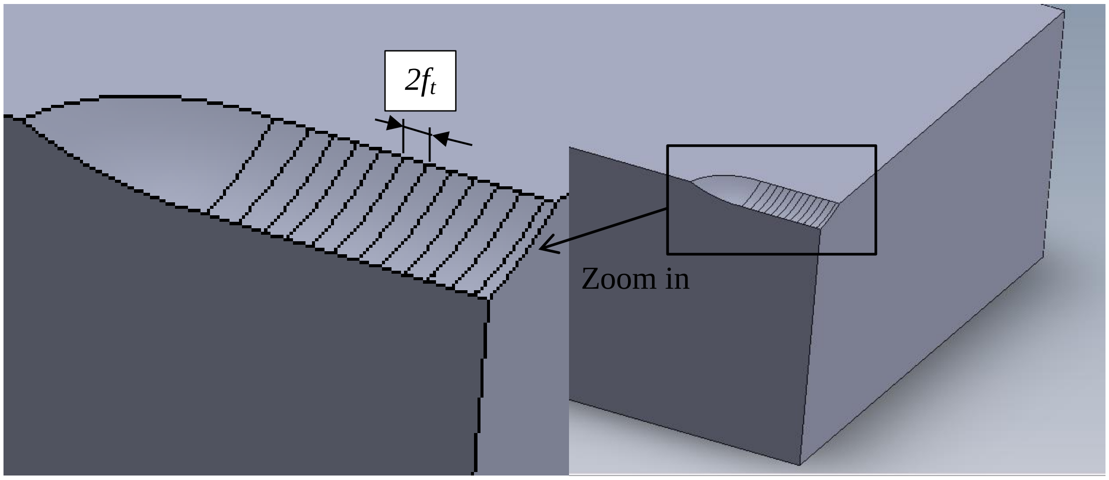

Figure F. 1 SolidWork Simulation of Surface Formation in Ball End Milling with Tool Ø9.525, Depth of Cut 1mm , Chip Load 0.254mm/tooth.

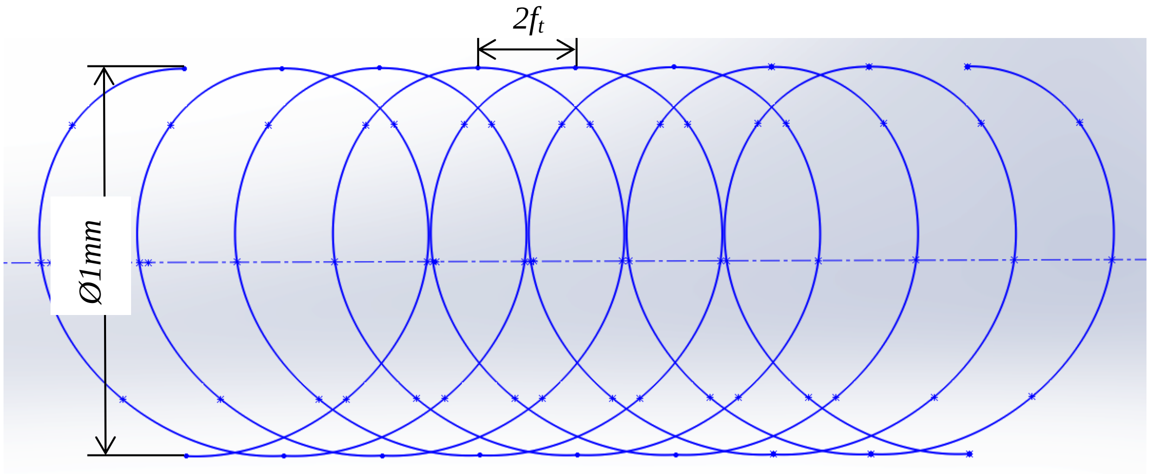

Figure F. 2. SolidWorks Simulation of the Tool Cutting Edges Motion (Top View). Chip load 0.254mm/tooth, Diameter of Tool Section 1mm.

APPENDIX G

SURFACE PROFILE RAW DATA OBTAINED WITH ZYGO INTERFEROMETER

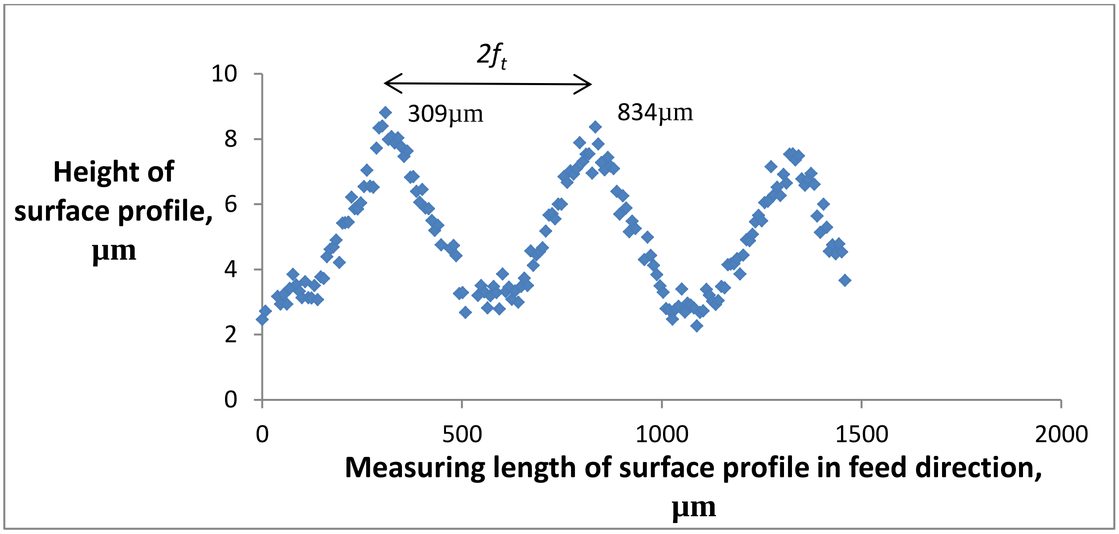

Figure G. 1 Raw Surface Profile Data at Channel Bottom. Chip Load 254µm/tooth, Cutting Speed 15m/min, 6061-T6.

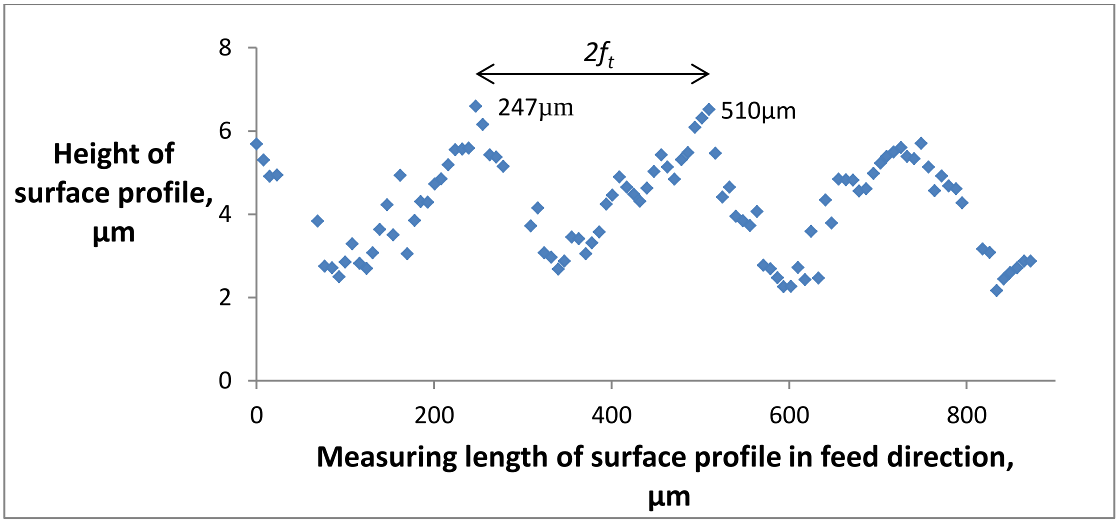

Figure G. 2 Raw Surface Profile Data at Channel Bottom. Chip Load 127µm/tooth, Cutting Speed 15m/min, 6061-T6.

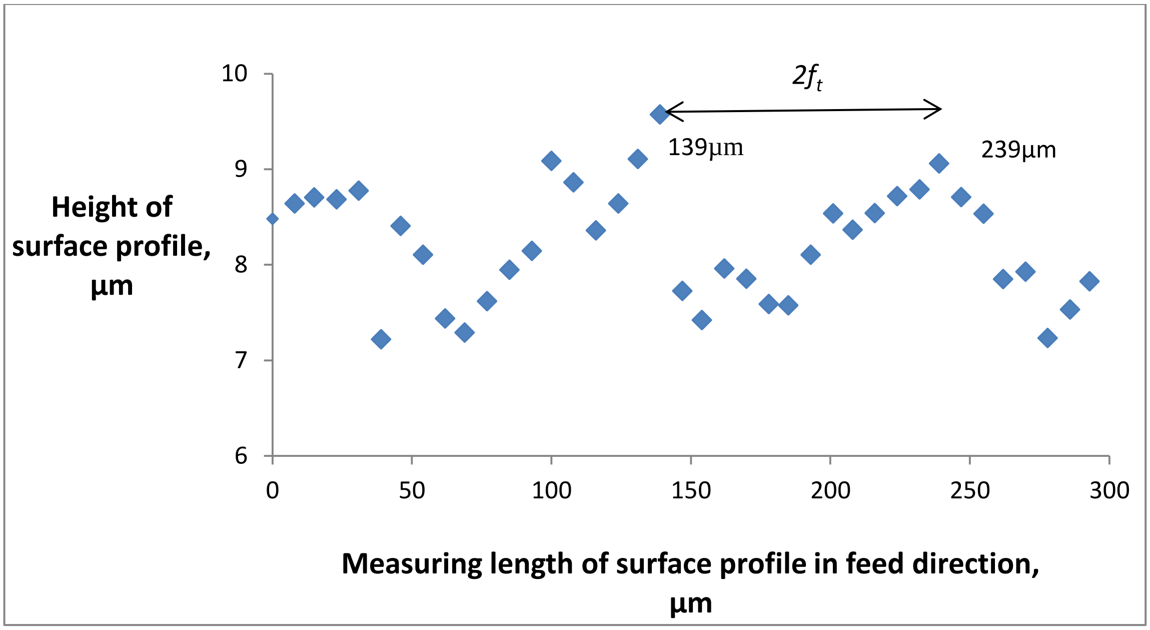

Figure G. 3 Raw Surface Profile Data at Channel Bottom. Chip Load 51µm/tooth, Cutting Speed 15m/min, 6061-T6.

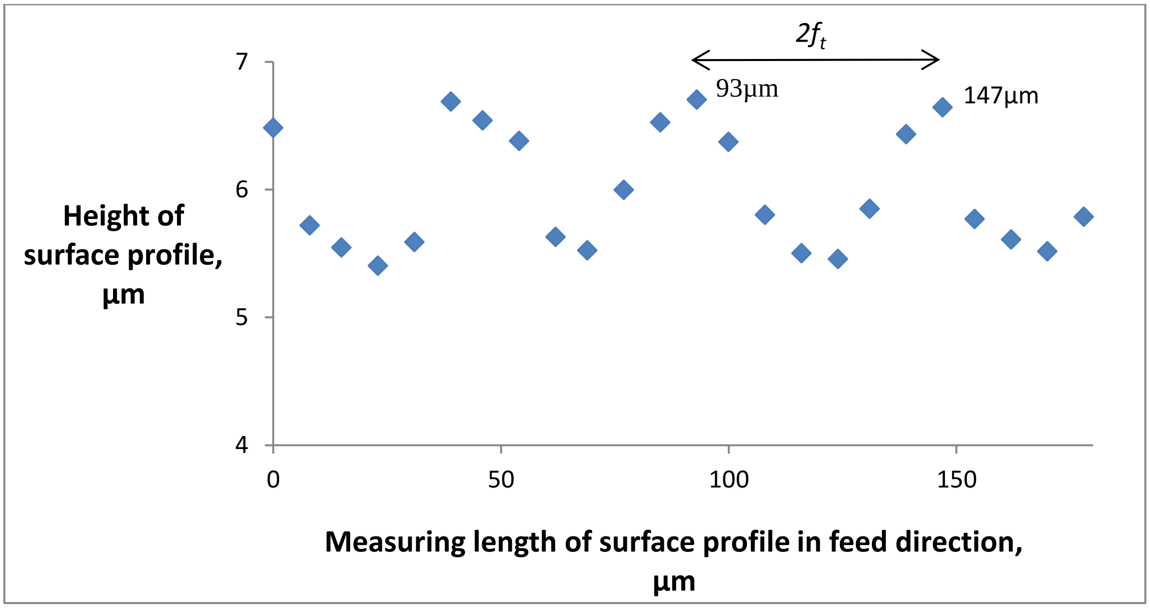

Figure G. 4 Raw Surface Profile Data at Channel Bottom. Chip Load 25.4µm/tooth, Cutting Speed 15m/min, 6061-T6.

APPENDIX H

HIGH ASPECT RATIO CHANNELS

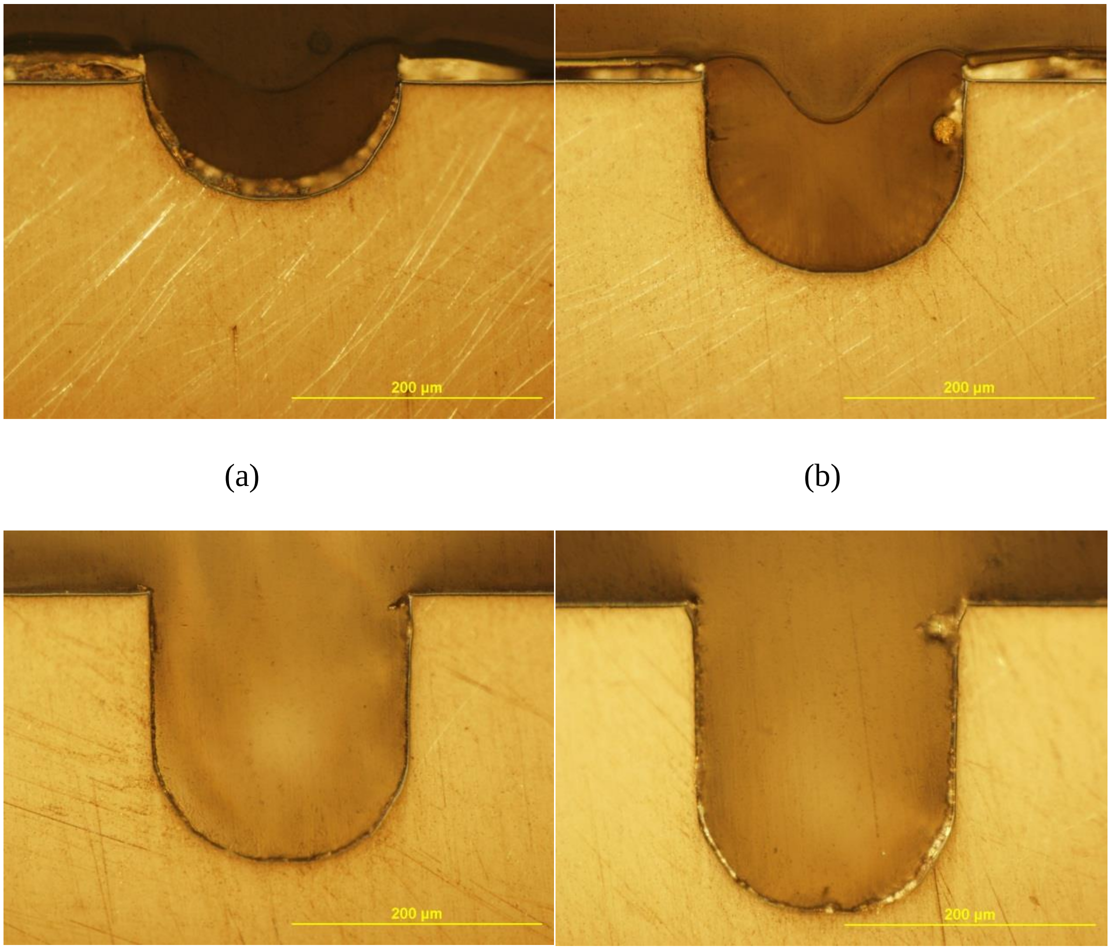

(a) (b)

(c) (d)

Figure H. 1 Profile of the Microchannels with Aspect Ratios: (a) 0.5:1; (b) 0.8:1; (c) 1.1:1; (d) 1.2:1. AlTiN Coated Tool Ø198µm, f_t=0.1µm/flute, V=24m/min, Ap=0.03mm, 316L Stainless Steel, MQL.

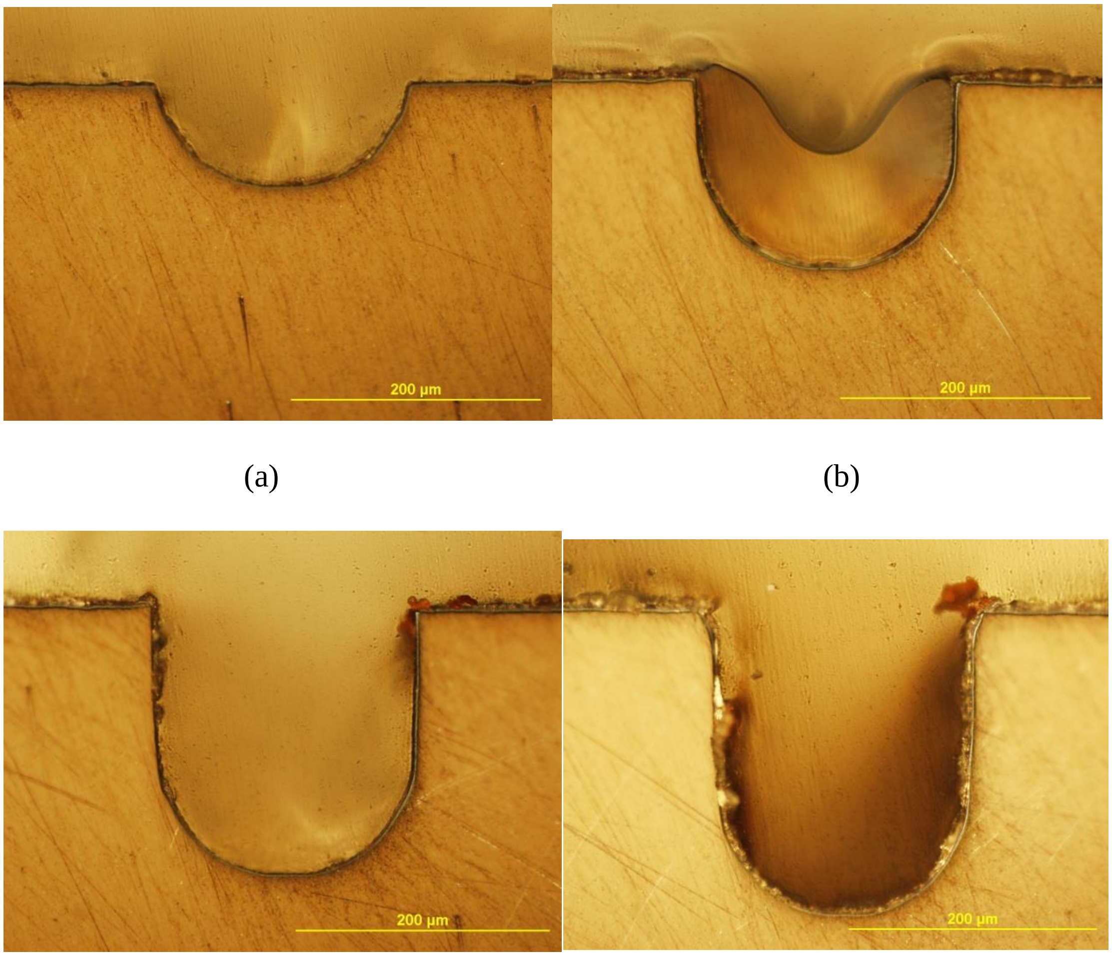

(a) (b)

(c) (d)

Figure H. 2 Profile of the Microchannels with Aspect Ratios: (a) 0.5:1; (b) 0.8:1; (c) 1.1:1; (d) 1.2:1. AlTiN Coated Tool Ø198µm, f_t=0.1µm/flute, V=24m/min, Ap=0.03mm, NiTi Alloy, MQL.